Universität Stuttgart

Institut für Wasser- und Umweltsystemmodellierung

Mitteilungen

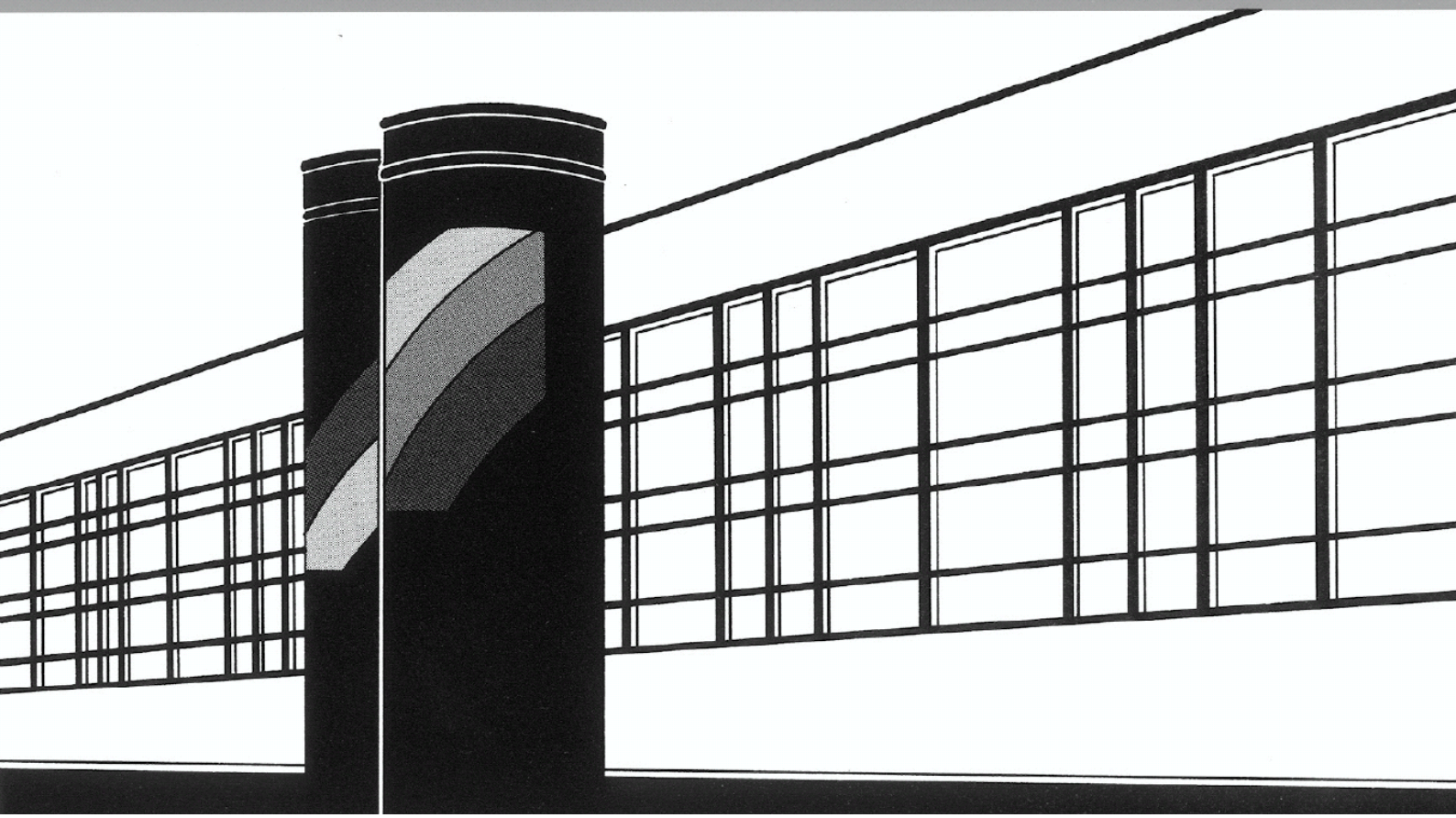

Heft 230 Benjamin Faigle

Adaptive Modelling of Compositional Multi-Phase Flow with Capillary Pressure

Adaptive Modelling of Compositional Multi-Phase Flow with Capillary Pressure

von der Fakultät Bau- und Umweltingenieurwissenschaften der Universität Stuttgart zur Erlangung der Würde eines Doktor-Ingenieurs (Dr.-Ing.) genehmigte Abhandlung

vorgelegt von

Benjamin Faigle
aus Mühlacker

Hauptberichter:	Prof. Dr.-Ing. Rainer Helmig
Mitberichter:	Prof. Ivar Aavatsmark
Mitberichter:	Dr. habil Bernd Flemisch.

Tag der mündlichen Prüfung: 2.12.2013

Institut für Wasser- und Umweltsystemmodellierung
der Universität Stuttgart
2014

Heft 230

Adaptive Modelling of Compositional Multi-Phase Flow with Capillary Pressure

von
Dr.-Ing. Benjamin Faigle

Eigenverlag des Instituts für Wasser- und Umweltsystemmodellierung
der Universität Stuttgart

D93 **Adaptive Modelling of Compositional Multi-Phase Flow with Capillary Pressure**

Bibliografische Information der Deutschen Nationalbibliothek
Die Deutsche Nationalbibliothek verzeichnet diese Publikation in der Deutschen Nationalbibliografie; detaillierte bibliografische Daten sind im Internet über http://www.d-nb.de abrufbar

Faigle, Benjamin:
Adaptive Modelling of Compositional Multi-Phase Flow with Capillary Pressure, Universität Stuttgart. - Stuttgart: Institut für Wasser- und Umweltsystem-modellierung, 2014

(Mitteilungen Institut für Wasser- und Umweltsystemmodellierung, Universität Stuttgart: H. 230)
Zugl.: Stuttgart, Univ., Diss., 2014
ISBN 978-3-942036-34-4

NE: Institut für Wasser- und Umweltsystemmodellierung <Stuttgart>: Mitteilungen

Herausgegeben 2014 vom Eigenverlag des Instituts für Wasser- und Umweltsystem-modellierung

Druck: Document Center S. Kästl, Ostfildern

Danksagung

Diese Arbeit entstand während meiner Zeit am Lehrstuhl für Hydromechanik und Hydrosystemmodellierung der Universität Stuttgart, und ich danke der Deutschen Forschungsgemeinschaft (DFG) für die Förderung dieses Projekts.

Mein besonderer Dank gilt Rainer Helmig für sein Zutrauen, seine Motivation und Unterstützung. Seine schlaue, offene Art hat mir einen einzigartigen Einblick in die Welt der Wissenschaft ermöglicht, mir viele Türen geöffnet und tolle Erlebnisse beschert. Ich möchte Ivar Aavatsmark für den Mitbericht, seine detaillierte und unkomplizierte Hilfe und für eine wunderschöne Zeit in Norwegen danken. Bernd Flemisch danke ich für seine unentbehrliche Unterstützung, wenn ich ins Stocken geraten bin, für viele Ratschläge und lehrreiche Gespräche, aber auch für seinen feinen Humor.

Nicht zuletzt habe ich es Rainer Helmig zu verdanken, dass ich mit solch tollen Kolleginnen und Kollegen zusammenarbeiten durfte, sowohl am Lehrstuhl als auch im Graduiertenkolleg. Im besonderen danke ich Philipp Nuske für die wichtigen Kicks zurück in die Spur, und Markus Wolff für die enge Zusammenarbeit als "Entkoppelte". Ich danke Prudence Lawday für ihre Hilfe und Ratschläge, und Sebastian Geiger für reichlich wertvollen Input. Von Annozie Ebigbo und Holger Class durfte ich sehr viel lernen, und vielen Dank an Jochen Fritz, der mir thematisch den Weg geebnet hat. Ich möchte allen Kollegen für die freundliche Atmosphäre und die gegenseitige Unterstützung danken, unter anderem bei der gemeinsamen Entwicklung des Softwareprojekts DuMu^{x} bzw. DUNE, aber auch für die tolle Zeit neben der Arbeit.

Abschließend möchte ich meiner Familie und insbesondere Karin Werle danken, die beim zermürbenden Debuggen einiges an Frust zu ertragen hatten, und mich immer wieder aufgebaut haben.

Contents

List of Figures

List of Tables

Notation

Symbol	Definition	Dimension
Scalars:		
ε	Error term (3.38)	[1/s]
ϕ	Porosity	[−]
Φ_α	Phase potential; Equation (3.42)	[Pa]
φ^κ	Fugacity coefficient of component κx	[−]
ϱ_α	Density of phase α	$\left[\mathrm{kg/m^3}\right]$
λ_α	Mobility of phase α	$[1/(\mathrm{Pa}\cdot\mathrm{s})]$
$\lambda_{E,\alpha}$	Heat conductivity of phase α	$[\mathrm{W}/(\mathrm{m}\cdot\mathrm{K})]$
$\bar{\lambda}_E$	Combined heat conductivity of the porous medium	$[\mathrm{W}/(\mathrm{m}\cdot\mathrm{K})]$
μ, μ_α	Dynamic viscosity	$[\mathrm{Pa}\cdot\mathrm{s}]$
μ^κ	Chemical potential of component κ	[J/mol]
ν_α	Phase mass fraction of phase α	[−]
A	Area, typically related to a face γ between two cells	$[\mathrm{m^2}]$
a	Coefficient for time-step control, Equation (3.53)	[−]
C^κ	Total concentration of component κ	$\left[\mathrm{kg/m^3}\right]$
c_p, c_v	Isobaric and isochoric specific heat capacity, respectively	$[\mathrm{J}/(\mathrm{kg}\cdot\mathrm{K})]$
c_s	Specific heat capacity of solid phase	$[\mathrm{J}/(\mathrm{kg}\cdot\mathrm{K})]$
$\hat{c}$	Total compressibility of the fluid mixture	[1/Pa]
$\bar{d}$	Mean particle size of the porous medium	$[mm]$
n_{dim}	The number of dimensions of the system	[−]
f(...)	An unspecified function of ...	
f_α	Fractional flow factor of phase α	[−]
f^κ	Fugacity of component κ	[Pa]
F_i	Representative magnitude of a flux associated with cell i	$\left[\mathrm{kg/sm^3}\right]$
g	Gravity as a scalar quantity, $g = \mathbf{g} * \lvert\mathbf{z}\rvert$	$\left[\mathrm{m/s^2}\right]$
H, h	Enthalpy and specific enthalpy, respectively	[J], [J/kg]
h_{vap}	Specific enthalpy of vaporisation	[J/kg]
$H_\alpha^{\infty\kappa}$	Henry coefficient of component κ in phase αx	$[Pa]$
K	Scalar permeability, possibly representing individual diagonal entries of a tensorial $\boldsymbol{K}$ if explicitly stated	$[\mathrm{m^2}]$

K_α^κ	(Mass) equilibrium ratio for component κ in phase α	$[-]$
$k_{r,\alpha}$	Relative permeability of phase α	$[-]$
M^κ	Molar mass of component κ	[kg/mole]
m^κ	Mass of substance κ	[kg]
n	An amount of a specific quantity	$[-]$
p_α	Pressure in phase α	$[Pa]$
p_c	Capillary pressure	$[Pa]$
p_{vap}	Vapour pressure	$[Pa]$
Q	Volumetric flux	$[\mathrm{m}^3/\mathrm{s}]$
q^κ	Mass source of component κ	$[kg/\left(\mathrm{s}\cdot\mathrm{m}^3\right)]$
q^E	Heat source	$\left[\mathrm{W}/\mathrm{m}^3\right]$
R	Universal gas constant	$[\mathrm{J}/\left(\mathrm{mole}\cdot\mathrm{K}\right)]$
S	Salinity, the salt content of the brine	$[kg/kg]$
S_α	Saturation of phase α	$[-]$
S_e	Effective saturation	$[-]$
$S_{r,\alpha}$	Residual saturation of phase α	$[-]$
T	Temperature	[K]
t	Time	[s]
Δt	Time-step	[s]
U, u	Internal Energy and specific internal energy, respectively	[J], [J/kg]
V	Volume	$[\mathrm{m}^3]$
v	Specific fluid volume	$[\mathrm{m}^3/\mathrm{m}^3]$
X_α^κ	Mass fraction of component κ in phase α	$[-]$
x	Coordinate in first (horizontal) direction	[m]
Δx	Discretisation length in x-direction	[m]
x_α^κ	Mole fraction of component κ in phase αx	$[-]$
y	Coordinate in second (horizontal) direction	[m]
Z^κ, z^κ	Feed mass and feed mole fraction of component κ	$[-]$
z	Coordinate in third (vertical) direction	[m]

Vectors/Matrices

$\boldsymbol{A}, \boldsymbol{B}, \boldsymbol{C}, \boldsymbol{D}$	Flux-related matrices of the MPFA-method	
$\nabla\Phi$	Potential gradient	[Pa/m]
$\boldsymbol{F}$	Stiffness or coefficient matrix	
$\mathbf{g}$	Vector of gravity	$\left[\mathrm{m/s^2}\right]$
$\mathbf{J_E}$	Conductive heat flux	$[\mathrm{W/m^2}]$
$\boldsymbol{T}$	Transmissibility matrix of the MPFA-method	
$\mathbf{n}_\gamma$	Unit normal vector on control volume surface γ	[m]
$\mathbf{n}_{\gamma_{ij}}$	Unit normal vector on surface γ pointing from cell i to j	[m]
$\boldsymbol{\chi}$	Vector of unknowns	
$\mathbf{d}, \mathbf{d}_{ij}$	Normalized vector connecting the cell center of i with its neighbour's center j.	[m]
$\mathbf{v}_\alpha$	Velocity of phase α	[m/s]
$\mathbf{x}$	Position vector with entries $\mathbf{x} = (x, y, z)^T$	[m]

subscripts

α	Phase
β	Subset of phases α without a certain phase
w, n, g, s	Wetting, non-wetting, gas and solid phase
m	Index of iteration
r	Reference phase (for equilibrium calculations)
i	Specific cell of the grid. Also used for the cell's properties.
j, j'	Neighbouring cell to cell i
k	The cells contained in all interaction regions related to the interface
l	Son cells after the refinement of a father cell
liq	A liquid phase with undefined wetting capabilities

superscripts

κ, ι	Component, $\iota \in \kappa$ resembles a specific component
T	Transposed vector
$*$	Reference state (for equilibrium calculations)
$\breve{}$	Quantities attributed to one interaction region

symbols

$\hat{}$	Combined property, obtained by summation over all elements of a set.
$\bar{}$	Averaged property.

Abstract

Many technical as well as environmental applications in the field of multi-phase flow in porous media, such as CO_2 storage in the subsurface, remediation of hazardous spills in the groundwater or gaseous infiltration from nuclear storage sites into the surrounding rock, take place on a huge spatial domain and occur over large time-scales. In most cases, however, complex flow regimes occur only in small regions of the whole domain of interest. Inside these regions, the quality of simulations benefits from highly resolved grids and from an in-depth description of the physics involved. Outside, in contrast, the grid can remain coarse and the relevant processes are already captured by a simpler model abstraction.

To simulate such processes, numerical models have to be developed that mimic the relevant system properties and characteristics of flow. In this work, the sequential solution scheme is shown to be an efficient alternative to fully implicit formulations for compressible, compositional multi-phase systems; it even considers the often neglected gravitational effects and capillary pressure. An extension for non-isothermal flow is presented as well. Some numerical obstacles have to be mastered to model these numerically challenging systems in an efficient manner, avoiding costly iteration of the global solution.

Two adaptive strategies are discussed: the multi-physics concept adapts the model complexity locally according to the underlying physical processes. Complicated physics are approached by complex models that differ from those applied in flow regimes that are simpler. The efficiency gain is flanked by the qualitative improvement to model each process not only with the fastest, but also with the most appropriate numerical model. As an example of such an adaptive modelling strategy, a large-scale CO_2 injection scenario is presented. This example provides insights into the increased efficiency, as well as the decrease in modelling bias because the constraint on one numerical model per simulation is relaxed and the most appropriate available model is applied locally.

In the quest for a good global solution, the physical and thermodynamic detail employed in complicated areas should be supported by a detailed resolution of the grid. Uniform

refinement a priori is again avoided in favour of dynamic adaptation, resembling the second branch of adaptivity in this work. Detail and accuracy are gained in the region of interest while the global system remains coarse enough to be solved efficiently. The modification of the simulation grid should not be an additional source of error: for the complex systems considered, this requires careful transformation of the data while modifying the grid. Indicators have to be developed that steer the dynamic adaptation of the grid. These should be tailored to the specific problem at hand. Nevertheless, the stability of the numerical formulation applied is jeopardized by the types of indicators that would cause a back-coupling of modelling errors into the refinement process. On such adaptive grids, the standard approach to computing fluxes is known to fail. An alternative method, a multi-point flux approximation, is successfully applied and the improvements investigated. The combination with the standard flux expression yields a very efficient and potent solution to modelling compositional flow on adaptive grids.

The proposed conceptual methods can only be successfully adapted if they are applicable to real problems. The large-scale simulations presented in this work are not intended to answer specific problem-related questions but to show the general applicability of the modelling concepts even for such complicated natural systems. At the same time, such large-scale real systems provide a good environment for balancing the efficiency potentials and possible weaknesses of the approaches discussed. The last example features four levels of complexity bonded together in the multi-physics setting: compositional single-phase flow with a simplified thermal approximation and under full non-isothermal consideration as well as compositional two-phase flow with and without full non-isothermal effects. Simulations are performed on an adaptively refined simulation grid.

Zusammenfassung

Simulationen sind ein wertvolles Werkzeug, um komplexe Strömungsvorgänge im Untergrund zu analysieren, Entwicklungen in der Zukunft abschätzen beziehungsweise das Risiko menschlicher Eingriffe abwägen zu können. Eine beispielhafte Anwendung ist die unterirdische Speicherung von CO_2, wo riesige Mengen des überkritischen Gases in den Untergrund verpresst werden, um durch eine dauerhafte Speicherung den Ausstoß des klimaschädlichen Gases in die Atmosphäre zu vermindern. Bevor im großen Maßstab mit einer Injektion begonnen wird, sind großskalige Rechnungen nötig, die nicht nur den direkten Injektionsbereich umfassen, sondern auch weiträumige Effekte abdecken können. Der weitreichende Druckanstieg, zum Beispiel, könnte das Deckgestein gefährden oder mit anderen Nutzungen des Untergrunds interferieren, oder aber durch Verdrängung des potentiell salzhaltigen oder anderweitig belasteten Wassers vorher unbelastete wasserführende Schichten gefährden. Da eine dauerhafte Speicherung anvisiert wird, muss das riesige Untersuchungsgebiet zudem über lange Zeitabschnitte hin simuliert werden. Die großen Zeit- und Längenskalen in Verbindung mit den komplizierten Vorgängen während der Injektion (Löslichkeitseffekten, zeitliche Änderung vieler Fluideigenschaften, auch hinsichtlich Temperaturschwankungen, bis zum komplizierten Zusammenspiel zwischen den Fluiden und dem Korngerüst des Gesteins) stellt die Simulation solcher Szenarien höchste Anforderungen an die Numerik. Eine Risikobewertung könnte sogar eine Vielzahl an aufwändigen Simulationen mit unterschiedlichen Eingangsdaten erfordern.

Komplizierte Modelle wurden entwickelt, die immer mehr Prozesse auflösen können, deren Umfang zur Beschreibung einfacherer Systeme aber überdimensioniert erscheinen. Denn oftmals variieren die Prozesse und damit auch der erforderliche Rechenumfang räumlich: Im erwähnten Beispiel der CO_2-Speicherung sind die kompliziertesten Vorgänge dort zu beobachten, wo das CO_2 mit dem Wasser in Kontakt ist, und dort baut sich auch der treibende Druckgradient auf. Eine Migration von Salzwasser ins Frischwasser ist durch den großflächigen Verdrängungsprozess aber auch in weit entlegenen Bereichen möglich, wohin kein CO_2 gelangen wird und demnach damit assoziierte Prozesse irrelevant sind. Dennoch ist deren isolierte Betrachtung unmöglich, sodass beide Teilprozesse in die Berechnung einbezogen werden müssen, bestenfalls mit dem dazu passenden Modell. Ein

solch flexibler Modellansatz verspricht nicht nur qualitative Vorteile durch den Einsatz eines lokal geeigneten Modells, sondern vemeidet überflüssig verschwendete Rechenzeit, indem einfache Systeme nicht mit zu komplizierten Modellen gelöst werden.

Vor einer Kombination von Modellen müssen jene zuerst einzeln entwickelt werden. In dieser Arbeit liegt der Fokus auf einer sequentiellen Lösungsstrategie, die gegenüber einem gekoppelt voll-impliziten Ansatz bei advektionsdominierter Strömung effizienter und unter Umständen sogar stabiler sein kann. Um die nichtlinearen Abhängigkeiten komplexer Strömung im Untergrund dennoch abbilden zu können, und nicht wie einige vergleichbare sequentielle Ansätze auf das Vernachlässigen von dichte-getriebener Strömung und Kapillarkräften angewiesen zu sein, sind diverse numerische Hürden zu nehmen. Ähnliches gilt für die Erweiterung auf nicht-isotherme Systeme, da hier zusätzlich die Energiebilanz beachtet werden muss. Bei der Anwendung der Modelle werden auch die Grenzen des Lösungsverfahrens sichtbar, sobald diffusive Kräfte die Überhand gewinnen - hier besteht Raum für weitere Modellverbesserung, zum Beispiel bezüglich einer stabilen zeitlichen Auflösung, des Zeitschrittmanagements.

Insgesamt werden in der Arbeit zwei adaptive Strategien verfolgt: Ein Mehr-Physik–Ansatz passt die numerische Abstraktion an die lokal auftretenden physikalischen Prozesse an. Obwohl das gesamte Modellgebiet gelöst wird, wird örtlich selektiv das am besten passende Modell gewählt und zum Gesamtsystem verknüpft. Dadurch wird verhindert, dass modellbedingte Unsicherheiten auch in Gebiete durchschlagen, die durch einfachere Modelle besser gelöst werden könnten. Zudem wird überflüssiger Rechenaufwand vermieden, da die aufwändigen Teilgebiete nicht das Niveau des Gesamtsystems vorgeben. Am Beispiel eines synthetischen Szenarios zur CO_2 Speicherung wird der Effizienzgewinn sichtbar. Allerdings offenbart es auch die Schwächen des entkoppelten Lösungsschemas, die ungenaue Näherung der nichtlinearen Beziehungen.

Diese Fehler könnten durch eine feinere Gitterauflösung reduziert werden, während auf eine Verfeinerung in weniger relevanten Teilgebieten aus Effizienzgründen verzichtet werden sollte. Die dynamische Gitterverfeinerung stellt damit die zweite adaptive Strategie dar. Damit können einzelne Bereiche feiner aufgelöst werden, ohne die generelle Lösbarkeit des Gesamtsystems dadurch zu gefährden, dass sich die Gleichungssysteme durch globale Gitterverfeinerung aufblähen. Um das Gitter an die Strömung anpassen zu können, muss ein geeigneter Indikatorensatz entwickelt werden. Obwohl dieser prinzipiell problemspezifisch definiert werden muss, schließt das gewählte Lösungsverfahren

einige bereits im Vorfeld aus - schließlich soll die Gitterverfeinerung keinen negativen Einfluss auf die Stabilität des Verfahrens haben. Ein adaptiv verfeinertes reguläres Gitter stellt ein Beispiel dar, bei dem die Standardmethode fehlerhafte Flüsse zwischen Zellen produziert. Diese Schwächen vermeiden mehrere Alternativansätze, darunter die Mehrpunktflussverfahren, deren sogenannte "L-Methode" wie gemacht für die Simulation auf adaptiven Gittern ist. Hier wird der Einflussbereich der Flussberechnung vergrößert und dadurch Fehler reduziert, was natürlich mit einem größeren Rechenaufwand einhergeht. Die Kombination beider Methoden allerdings stellt einen sehr effizienten und leistungsfähigen Ansatz dar, der auch große und physikalisch komplexe Systeme bewältigen kann.

Die beiden beispielhaften großskaligen Simulationen in dieser Arbeit sind als Machbarkeitsstudien der Methodik zu verstehen, sodass deren Ergebnisse keine expliziten Fragen beantworten sollen. Sie zeigen allerdings, dass die Ansätze erfolgreich auch für reale Problemstellungen Anwendung finden können. Zudem kann so der reale Effizienzgewinn abgeschätzt werden, und auf Stärken als auch Schwächen der Ansätze eingegangen werden.

1 Introduction

1.1 Motivation

Numerical modelling of subsurface flow often spans long periods of time and has to cover a considerably large spatial domain. For example, safety assessments of storage sites for nuclear waste have to investigate if hazardous substances can reach and contaminate groundwater aquifers within at least decades, and since storage caverns will not lie in the vicinity of these precious aquifers, the area of investigation is considerably large. Another example might be the injection of CO_2 into the subsurface to mitigate its effect as a greenhouse gas on the climate. The common theme here is the question whether the CO_2 could leak back into the atmosphere, and which kind of pathways allow for such rising from deep underground. In addition, simulations can assist in the screening of appropriate storage locations and the development of injection strategies to preserve the integrity of the formations and prevent the displaced formation fluid to cause harm, possibly far away from injection. Then again, both the time span of interest and the spatial domain, at least for injection volumes necessary to actually mitigate anthropogenic emissions, are large. So are the computational demands, which despite ever growing computational power still require the development of efficient modelling tools.

These simulations are based on a (mathematical) conceptual model that is an abstraction of the complex (natural) phenomena. It is therefore necessary to identify the important and relevant processes and translate them into mathematical formulas while still maintaining a level of complexity where their solution is still possible. As research improves the understanding of the underlying physical processes, more detail and complexity can be included in the model, which increases computational demands. This balancing act is an inter-disciplinary challenge, as improvements in the thermodynamic description, for

example, should not be eroded by inaccuracies of the discretisation method or problems with the implementation. It gets even more inter-disciplinary as soon as these simulation results need to be interpreted and get perceived by the stakeholders. To do so, multiple simulation runs might be necessary to analyse parameter sensitivities and uncertainty, or in order to discuss the influences of model assumptions. Then again, efficiency becomes an important factor.

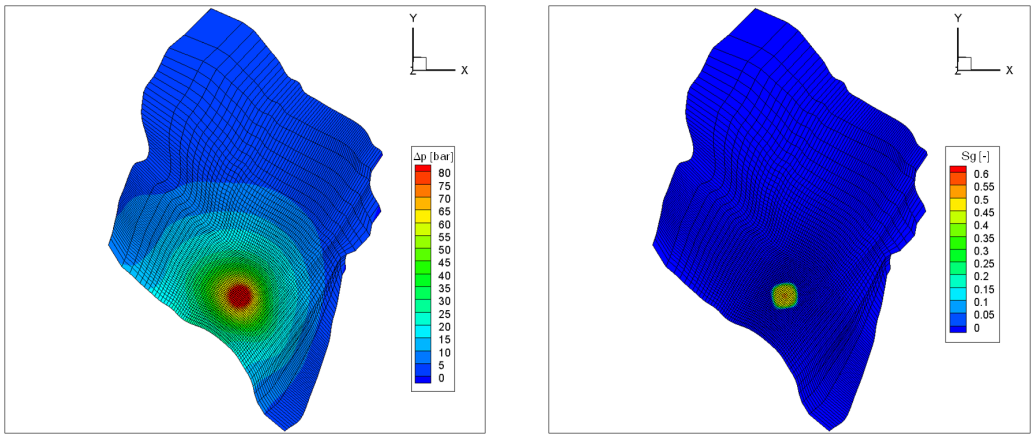

Figure 1.1: Change in reservoir pressure (left) and the plume shape of CO_2 (right) after 10 years of simulated injection (*Schäfer et al.*, 2012).

In most cases of multiphase flow in porous media, the level of complexity and their relevance for the simulation results differ significantly. Complex flow regimes that should be resolved in high detail might occur only in small regions of the whole modelling domain, which means a coarser description might be sufficient outside. Likewise, the physical processes might require a more detailed approximation locally while in other regions, the processes show better resemblance if simpler conceptual models are applied. Over the large periods of time, some driving forces might become more significant as others cede.

As an example, the propagation of brine along a pressure gradient induced by injected CO_2 can be modelled with relatively simple numerical models. Yet the original displacement that lead to the flow of brine requires the modelling of the complicated processes attributed to the injection (two-phase effects with mutual dissolution, thermal effects, or even mineralization around the injection well), that could even be superposed by background flow from an additional human intervention such as geothermal energy. While brine is also displaced in the far field, away from the injection area (Figure 1.1 left), the region of injection remains a local phenomenon (Figure 1.1 right). At best, the

level of detail should adapt to the underlying processes and should not be decided a priori by the modeller.

Naturally, this can never be fully accomplished, but I present two adaptive strategies that can be principally followed independently, and are also discussed separately: the multi-physics concept adapts the numerical model complexity locally according to the underlying physical processes. Complicated physics are approached by complex abstractions that differ from those applied in flow regimes that remain simple (Figure 1.2). Secondly, an adaptive refinement of the modelling grid gains detail and accuracy in regions of interest while the global system remains coarse enough to be efficiently solved. These dynamic or adaptive simulation frameworks attempt to balance between accuracy / detail and reason / efficiency. They allow us to use the appropriate and best available numerical model and grid resolution locally.

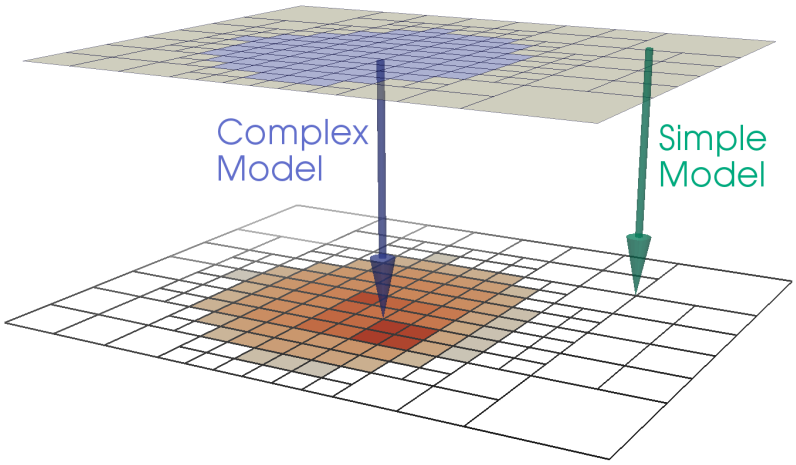

Figure 1.2: Schematic of the multi-physics framework: different models are applied locally to model the combined problem. The simulation grid is adaptively refined around the plume to complex physical processes occurring here.

1.2 Literature context

This work employs the numerical models for compositional multiphase flow and the multi-physics framework to combine the individual models of different complexity that where developed in *Fritz et al.* (2012); *Fritz* (2010). The bonding of the models is simplified by formulating them mathematically by means of one pressure equation based

on (*Ács et al.*, 1985) and sequentially solved transport equations, which circumvents the coupling by domain decomposition techniques (*Peszyńska et al.*, 2000; *Peszyńska*, 2003). The latter approach, however, would also allow to use different numerical solution schemes for the individual models (*Wheeler et al.*, 1999). A good overview of different coupling schemes and multi-physics models can be found in *Wheeler and Peszyńska* (2002). As an extension to previous work, capillary pressure is included in the two-phase models to increase the range of applicability (*Faigle et al.*, 2013).

The second branch of adaptivity considered here involves a dynamic adjustment of the simulation grid, whereas the focus lies exclusively on regular grids. Adaptive mesh refinement (AMR) increases the resolution of the simulation mesh in regions of high interest while maintaining a coarse grid everywhere else. The technique is widely used in porous media flow with ongoing development (*Heinemann et al.*, 1983; *Mehl and Hill*, 2004; *Pau et al.*, 2012); many authors nest the refined areas into the coarse grid in a multi-grid or domain decomposition framework (*Hornung and Trangenstein*, 1997; *Trangenstein*, 2002; *Nilsson et al.*, 2005; *Pau et al.*, 2010; *Thomas and Wheeler*, 2011), allowing for parallel computations and an individual temporal resolution of coarse and fine grid patches. In the former approach on an integrated adaptive grid, the flux stencil has to be increased locally to avoid erroneous fluxes over interfaces between fine to coarse cells. A class of methods capable of doing so was initiated by (*Aavatsmark et al.*, 1994; *Edwards and Rogers*, 1994), the so-called Multi-Point Flux Approximations (MPFA). One of these, the L-method (*Aavatsmark et al.*, 2008), is perfectly suited for irregular grids that develop if regular grids are refined or coarsened.

1.3 Simulation environment

Simulation of complex flow regimes in the subsurface is a challenging task where knowledge from different disciplines have to come together. The modelling software has to provide a combination of efficient and potent grid managers, solvers and data structures necessary for most fields of computational science as well as the physical and thermodynamic properties and discretisation schemes for flow through porous media. The former is provided by the modular toolbox DUNE (Distributed and Unified Numerics Environment, *Bastian et al.* (2005, 2008b,a)), and especially the grid manager ALU (Adaptive, Load-balanced, and Unstructured Grid Library *Burri et al.* (2006))

that allows for a dynamic adaptation of the simulation grid. Included as well are Solvers, pre-conditioners and general data structures and methods for input and output. These features are then accessed and used by the modelling framework DuMu^{x} (DUNE for Multi-{Phase, Component, Scale, Physics, ...} flow and transport in porous media, *Flemisch et al.* (2011)). A core design principle of both projects is a high flexibility achieved through common interfaces and a modular setup. This is an essential requirement for both types of adaptivity applied in this work: general grid adaptivity can be supplemented with the requirements to model compositional multi-phase flow in a very efficient manner; And the individual sequential models can be incorporated into the flexible multi-physics framework by employing the strength of object-oriented programming to reduce code duplication.

Another important feature of DUNE and DuMu^{x} software is the open source licence, guaranteeing that the research produced is accessible for the whole society. On one hand this should improve the reproducibility of the results presented (see also the information given in Section 7.3), and might on the other hand ease usage and re-implementation of the approaches and concepts presented in this work.

1.4 Strucuture of the thesis

This work follows two strategies for adaptivity: the first alters the numerical complexity locally according to the underlying physical processes, and the second adapts the simulation grid. The applications and simulation examples intend to show the applicability of the presented frameworks.

Following this introduction, Chapter 2 describes the fundamental properties and functions of a compositional multi-phase system in a porous medium. The basic concepts are introduced and conservation laws are formulated. These are discretised in Chapter 3, and the numerical realisation of the mathematical models is discussed. The individual models bond together in the multi-physics framework in Chapter 4, which also includes a large-scale example to show the applicability of the framework. Then, as a second strategy, the adaptive grid refinement is presented in Chapter 5 and the resulting obstacles to model compositional multiphase flow up to three dimensions are resolved. The combination of both strategies is showcased on the large-scale CO_2 injection scenario (from Chapter 4)

in Section 6.1. Finally, the general applicability of the models is visualised in Section 6.2, which is based on an existing reservoir with challenging properties. The work is summarized in Chapter 7, which also includes an outlook for further research.

2 Fundamentals

This chapter provides the fundamental definitions and principal concepts to study multi-phase flow in porous media. The properties of the fluids and the thermodynamic description of mixtures is discussed first, followed by their interaction with the porous media which demands for additional concepts, laws and functional relations.

2.1 Fluid properties and thermodynamic relations

This section introduces the relevant fluid properties and their functional resemblance that need to be accounted for in the context of this work.

2.1.1 Phase composition

Fluids with homogeneous physical properties and chemical composition separated by a sharp interface are called phases. Such phases are typically classified into solid, gaseous and possibly several coexisting liquid phases. Each phase α can consist of one pure chemical substance or a mixture of several substances whose compartments are called components. This term is also used for a combination of substances that form a logical group: the component "air" comprises all its compartments (mainly N_2 and O_2, plus smaller fractions (*Römpp et al.*, 1999)).

Despite being defined via an interface, phase changes can occur due to changes in temperature or pressure, which would then lead to a transfer of mass over that interface. If two components of different phases come into contact, they usually do not remain completely immiscible: a small portion of gaseous air in contact with water, for example, gets dissolved in the water phase and vice versa. Such compositional effects may change

the thermodynamic properties of all phases α, making it necessary to quantify the components κ. The following quantities are used as measures.

The mole fraction x_α^κ relates the number of molecules of a component n_α^κ to the total number n_α of all molecules in the phase,

$$x_\alpha^\kappa = \frac{n_\alpha^\kappa}{n_\alpha} \, . \tag{2.1}$$

This relation can also be expressed by relating the mass of the components m^κ, which yields the mass fraction X_α^κ

$$X_\alpha^\kappa = \frac{m_\alpha^\kappa}{m_\alpha} = \frac{M^\kappa x_\alpha^\kappa}{\sum\limits_\kappa M^\kappa x_\alpha^\kappa} \, . \tag{2.2}$$

It translates to the mole fraction by means of the molar mass M^κ. By definition, the aforementioned fractions, as well as all other quantities denoted as a “fraction”, sum up to unity

$$\sum_\kappa x_\alpha^\kappa = \sum_\kappa X_\alpha^\kappa = 1 \, . \tag{2.3}$$

The volumetric measure of the mass concentration relates the mass of a substance to the total volume $\hat{V}_\alpha$ that is occupied by the fluid,

$$C_\alpha^\kappa = \frac{m_\alpha^\kappa}{\hat{V}_\alpha} \, . \tag{2.4}$$

In multiphase systems, the total amount of a substance in all phases can be quantified by the total concentration,

$$C^\kappa = \frac{\sum_\alpha m_\alpha^\kappa}{\hat{V}} = \sum_\alpha C_\alpha^\kappa \, . \tag{2.5}$$

2.1.2 Thermodynamic states and state variables

An ensemble of physical or thermodynamic properties describe the state of the fluid or system of fluids. These states are fixed end-points where it is irrelevant exactly how the system has arrived at the state. This means, at any given point in space and time, the state of the system can be exactly and fully determined. The association of phase

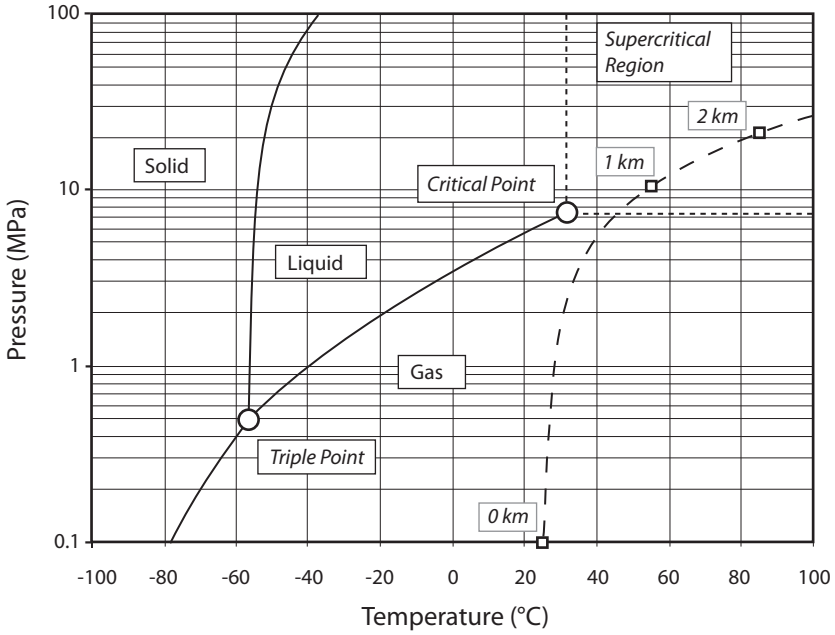

Figure 2.1: Phase diagram for pure CO_2 from *Nordbotten and Celia* (2012). Typical subsurface conditions are depicted by the dashed line.

state and system properties, such as temperature, pressure and composition, can be visualized in phase diagrams (Figure 2.1). The lines mark states where more than one phase coexist, a relevant information to determine the system state for a given set of system properties.

For applications considered in this work, the line for coexistent gas and liquid phases is of special importance. Expressed in functional form, its exploitation yields, for example, the vapour pressure p_{vap} of the liquid-gas mixture at any given temperature; or, inversely, the boiling temperature T_{boil}. In mathematical terms, the behaviour described above is accounted for with equations of state (EOS) that relate system properties, e.g. pressure and temperature, with properties of the fluids such as the density.

Denisty

The density of a fluid,

$$\varrho_\alpha = \frac{m_\alpha}{V_\alpha} \ , \tag{2.6}$$

Fluid	Property	Function	Literature
Water	Density	$\mathrm{f}(T, p_\alpha, X)$	*IAPWS* (1997); *Class et al.* (2002)
Brine	Density	$\mathrm{f}(T, p_\alpha, S, X)$	*IAPWS* (1997); *Bielinski* (2006)
Ideal Gas	Density	$\mathrm{f}(T, p_\alpha, X)$	
CO_2	Density	$\mathrm{f}(T, p_\alpha, X)$	*Darcis* (2012); *Span and Wagner* (1996)
TCE (NAPL)	Density	$\mathrm{f}(T, p_\alpha)$	*Reid et al.* (1987)

Table 2.1: Equations of state an their dependencies: temperature T, phase pressure p_α, salinity S, and phase composition indicated by the mass fraction X.

relates the mass of a phase with the volume it occupies. In general, there is a dependency on temperature, pressure and composition through the attractive or repulsive forces between the molecules. Typically, an increase in pressure or a lowering of temperature yields a higher density as mutual attraction is increased. For high pressure and temperature, the fluid enters the supercritical region (Figure 2.1), where the density approaches values of a liquid state while retaining the viscosity of a gas.

In functional form, one of the simplest equations of state is the ideal gas law,

$$\varrho = \frac{pM^\kappa}{RT} \ . \tag{2.7}$$

Here, R is the universial gas constant and T the fluid temperature. A large variety of equations of state can be found in textbooks such as *Poling et al.* (2001); *Atkins and De Paula* (2002); *Aavatsmark* (1995). Those applied in this work are summarized in table 2.1.

The inverse of the density function is the specific volume of a fluid, v_α, with the same functional dependencies. Its derivatives play a major role in the numerical scheme applied in this work. The derivative of the specific volume with respect to pressure is called compressibility,

$$\beta_\alpha = \frac{1}{\varrho_\alpha} \frac{\partial \varrho_\alpha}{\partial p_\alpha}\bigg|_{T, X_\alpha^\kappa} = -\frac{1}{v_\alpha} \frac{\partial v_\alpha}{\partial p_\alpha}\bigg|_{T, X_\alpha^\kappa} \tag{2.8}$$

The notation $|_{p_\alpha, X_\alpha^\kappa}$ implies that the partial derivative is to be formed by keeping the temperature and the composition of the phase constant. The compressibility of gases is much larger than that of liquids.

In a multiphase fluid system, the combined total compressibility describes the volumetric compaction of the fluid system for a given change in pressure,

$$\hat{c} = \left.\frac{\partial \hat{v}}{\partial p}\right|_{T,X^\kappa} . \tag{2.9}$$

If there is an EOS that describes the fluid system in all phase states, the total compressibility can be gained analytically. If this is not the case, it can be computed numerically investigating the change in combined fluid volume $\hat{v}$ for an infinitesimal change in all phase pressures (Section 3.3.5). Under boiling conditions, the total compressibility of the fluid system is orders of magnitudes lower than both β_α and $\hat{c}$ under non-boiling conditions, requiring a special treatment (Section 3.3.5).

Viscosity

In contrast to solids, fluids continue to deform when shear stress is applied: fluids can flow. The resistance to such a deformation is quantified by the viscosity *Bear* (1972). More specifically, the term in this work is used for the dynamic viscosity, μ_α. Viscosity is generally lower in gases than in liquids. Due to the strong temperature dependency, viscous fluids such as oil can be mobilized by an increase in temperature which decreases the viscosity.

Quantification of viscosity is only possible under transient, non-equilibrium conditions, so the discussion in this section might sound misguided. However, considering only Newtonian fluids, viscosity is independent of the magnitude of the velocity gradient but depends on the state of the system (*Poling et al.*, 2001). It can thus be discussed in the context of an equation of state (*Nordbotten and Celia*, 2012), which also justifies the application of similar mixing rules for example to consider gaseous mixtures, such as those mentioned in (*Class*, 2008).

Caloric quantities: internal energy and enthalpy

The state of fluids in a thermal system can be described by caloric state variables. These are the internal energy U, the energy that is stored inside the fluid; and the enthalpy H, that also includes the work necessary to provide enough space for it, and hence

displace the surrounding environment. Usually, both quantities are used as mass specific quantities u and h,

$$h = u + pv = u + \frac{p}{\varrho} \; . \tag{2.10}$$

As most quantities in Equation (2.10) are strongly dependent on temperature, the deviation of the caloric quantities with changes in temperature is captured by distinct quantities: the specific heat capacity at constant pressure,

$$c_p = \left.\frac{\partial h}{\partial T}\right|_p \; ; \tag{2.11}$$

and the partial derivative at constant volume,

$$c_v = \left.\frac{\partial u}{\partial T}\right|_v \; . \tag{2.12}$$

A system at boiling conditions remains at the boiling temperature even if it is further heated until the liquid phase has fully evaporated. The increase in energy is required for this vaporisation because the attractive forces in the liquid have to be overcome. The amount of energy required to change the phase state is called latent heat and can be quantified by the enthalpy of vaporisation,

$$h_{vap} = h_g - h_{liq} \; . \tag{2.13}$$

2.1.3 Phase equilibrium

The previous sections showed that fluid configuration, which stands for its composition and phase distribution in this work, is essential to describe the properties of the fluids. In equilibrium, the fluid system does not undergo further phase changes and flow of matter or energy has ceased. Then, the distribution of each component and the corresponding phase state can be calculated. Such an equilibrium is formulated locally, as are the fluid properties. Globally, in contrast, fluid properties may differ greatly and flow of matter may still be observable. The second law of thermodynamics demands that at equilibrium, intensive variables are the same in all phases, expressed by an equality of pressure p_α (mechanical equilibrium), temperature T_α (thermal equilibrium) and chemical potential μ_α^κ (material equilibrium)(*Aavatsmark*, 1995). The last two have to

be exploited to determine the phase state and phase composition of the material sample. In a gas-liquid system, we then have:

$$T_{liq} = T_g; \tag{2.14}$$

$$\mu_{liq} = \mu_g; \tag{2.15}$$

The range of values of the chemical potential is boundless, which makes it a very unfavourable quantity. This can be circumvented by the introduction of the fugacity f. For pure components, the fugacity describes the deviation from a hypothetical ideal gas, marked by an asterix, at a fixed reference pressure p_0.

$$\mu(T,p) - \mu^*(T,p_0) = RTln\frac{f}{p_0} \tag{2.16}$$

A gas is called ideal if the molecules do not interact with each other, and hence follows the ideal gas law, Equation (2.7). Using the thermal equilibrium (Equation (2.14)) and the fact that the chemical potential of perfect gases are equal, Equation (2.15) translates with Equation (2.16) to an equality of fugacity,

$$f_{liq} = f_g; \tag{2.17}$$

In a perfect gas, we can reach an arbitrary pressure by

$$\mu^*(T,p) - \mu^*(T,p_0) = RTln\frac{p}{p_0}\ . \tag{2.18}$$

A combination of Equation (2.16) and Equation (2.18) gives:

$$\mu(T,p) - \mu^*(T,p) = RTln\frac{f}{p}\ , \tag{2.19}$$

The fraction $\varphi = \frac{f}{p}$ is called the fugacity coefficient, which approaches unity in the case of an ideal gas. Accordingly, the fugacity can be seen as a kind of pressure correction that accounts for the non-ideal behaviour of real gases. For multicomponent systems, we follow the same methodology and introduce a fugacity $\check{f}$ that again describes the deviation from ideal behaviour, in this case from an ideal mixture. First, an ideal behaviour is regarded, where all substances in the mixture are subject to the same

interaction (such as attractive forces). It is described in analogy to Equation (2.18) by

$$\mu^*(T, p, x_\alpha^\kappa) - \mu^*(T, p_0, x_\alpha^\kappa) = RTln\frac{px_\alpha^\kappa}{p_0} \; . \tag{2.20}$$

As real mixtures deviate from an ideal mixture, we extend Equation (2.20) with a fugacity description for each component κ,

$$\mu(T, p, x_\alpha^\kappa) - \mu^*(T, p_0, x_\alpha^\kappa) = RTln\frac{\check{f}^\kappa}{p_0} \; , \tag{2.21}$$

which leans towards the step done for Equation (2.16). Combining Equation (2.21) and Equation (2.20) yields

$$\mu(T, p, x_\alpha^\kappa) - \mu^*(T, p, x_\alpha^\kappa) = RTln\frac{\check{f}^\kappa}{px_\alpha^\kappa} \; , \tag{2.22}$$

and provides analogous to Equation (2.19) a definition of the fugacity coefficient,

$$\varphi^\kappa = \frac{\check{f}^\kappa}{px_\alpha^\kappa} \tag{2.23}$$

for each component in the mixture. For an ideal mixture,

$$\varphi^\kappa = 1 \; . \tag{2.24}$$

The equality (2.17) in combination with Equation (2.23) and the assumption of mechanical equilibrium provides the equation

$$\varphi_g^\kappa x_g^\kappa = \varphi_{liq}^\kappa x_{liq}^\kappa \; , \tag{2.25}$$

which determines the composition of one phase given a known state of another phase, usually called reference phase. Conceptually, this can be done for all kinds of phases, as we calculate properties of real fluid behaviour by referencing with a hypothetical perfect gas state (*Michelsen and Mollerup*, 2007). If there is an appropriate equation of state, such as (2.7), that describes the behaviour in all phase states reasonably, the fugacity coefficients can be calculated and the composition of the fluid mixture at hand can be determined.

Instead of using the deviation from an ideal gas with a single EOS for both liquid and gas state, the liquid mixture can be described by comparing it to a pure liquid. If the fugacity of the pure liquid (Equation (2.18)) is subtracted from the fugacity of the liquid mixture (Equation (2.20)),

$$\mu(T,p,x_\alpha^\kappa) - \mu(T,p) = RTln\frac{\check{f}^\kappa}{f^\kappa} \,, \tag{2.26}$$

we get the definition of activity,

$$a^\kappa = \frac{\check{f}^\kappa}{f^\kappa} \,. \tag{2.27}$$

By definition (*Atkins and De Paula*, 2002; *Michelsen and Mollerup*, 2007), the activity equals the mole fraction in an ideal mixture, which also implies that the activity is a form of corrected mole fraction of an ideal mixture. Analogous to the fugacity coefficient, the deviation from ideal behaviour is expressed by the activity coefficient,

$$\gamma^\kappa = \frac{a^\kappa}{x^\kappa} = \frac{\check{\varphi}^\kappa}{\varphi^\kappa} \tag{2.28}$$

For a liquid consisting of one pure component, γ^κ equals unity.

An alternative to Equation (2.25) is gained by expressing the gaseous mixture in Equation (2.17) via the deviation from the ideal gas (Equation (2.23)) and the liquid mixture by the deviation from the pure liquid $f_{liq}^{\kappa,pure}$(Equation (2.28),

$$p\varphi_g^\kappa x_g^\kappa = f_{liq}^{\kappa,pure}\gamma^\kappa x_{liq}^\kappa \,, \tag{2.29}$$

Simplifications: Dalton**,** Raoult **and** Henry

For the applications considered in this work, fluid mixtures typically consist of a dominant species, allowing for a simplification of the thermodynamic system. As the dissolution behaviour in the water phase is of interest, the activity model (eqation 2.29) serves as the basis.

In ideal gases where the components of the mixture do not interact, Dalton found

that the sum of the partial pressures p_α^κ equals the total pressure,

$$p_\alpha = \sum_\kappa p_\alpha^\kappa \, . \tag{2.30}$$

In combination with Equation (2.1), this yields

$$p_\alpha^\kappa = x_\alpha^\kappa p_\alpha \, . \tag{2.31}$$

In the ideal case, the fugacity coefficient in the vapour is unity, and the fugacity of the pure component $f_{liq}^{\kappa,pure}$ at low pressure can be expressed by the vapour pressure $p_\alpha^{sat,pure}$. Then, Equations (2.29) and (2.31) yield

$$p_g^\kappa = p_{liq}^{sat,pure} x_{liq}^\kappa \tag{2.32}$$

This means that the partial pressure of the dissolved component is linearly dependent on its pure vapour pressure and the mole fraction, commonly known as Raoult's law. It can be a valid assumption if x_{liq}^κ approaches unity, so the dissolved component (solvent) has little influence on the fugacity of the dominant component in the liquid phase (solute), usually water. Under the assumption of an ideal gas at low pressures, however, it is typically a valid approximation to quantify traces of water that dissolve in the gas phase. As it was introduced in Equation (2.27), the activity acts as a corrected mass fraction to hold for non-ideal solutions, which means that a variation of Equation (2.32),

$$a^\kappa = \frac{p_g^\kappa}{p_{liq}^{sat,pure}} \tag{2.33}$$

would account for the non-ideal behaviour of the liquid mixture (*Atkins and De Paula*, 2002).

The solvent mole fraction, in contrast, approaches zero in the limit of a pure mixture, so its behaviour can hardly be described by a pure fluid. Henry nevertheless found a linear dependence of the partial vapour pressure with mole fraction (of the solute) and a component-specific Henry coefficient

$$p_\alpha^\kappa = H_\alpha^{\infty\kappa} x_{liq}^\kappa. \tag{2.34}$$

This coefficient is a measure of solute-solvent interaction at infinite dissolution (at

the limit $x^\kappa_{liq} \to 0$). In the context of Equation (2.29), we can quantify the dissolved component

$$p\varphi^\kappa_g x^\kappa_g = H^{\infty\kappa}_{liq}\gamma^\kappa x^\kappa_{liq} \tag{2.35}$$

Thus, the application of HENRY's law does not necessarily assume an ideal gas phase (*Poling et al.*, 2001). A variety of HENRY's coefficients for many substances, such as TCE used in Section 5.3, can be found in *Sander* (1999).

2.2 Fluid-matrix interaction in a porous medium

In a porous material, fluids not only interact with each other, but also with the solid skeleton. Such interactions include attractive or repulsive forces exerted by the solid surface, and exchange of heat. Mass exchange caused by reactions with the surface, or mere sorbtion or crystallization, which may occur if dissolved CO_2 forms solid carbonates, are explicitly disregarded in this work. On the one side, the rock matrix is assumed to be unaffected by the fluids, which, depending on the type of rock, might (*Lu et al.*, 2012) or might not (*Kharaka et al.*, 2006) be a reasonable assumption. The fluid properties, on the other side, are likewise considered to be unaffected by mass exchange with the solid, even though the solubility limit of CO_2 in brine, for example, can vary by up to 80% if salt concentration reaches 30% (*Nordbotten and Celia*, 2012).

The focus in this section lies on the contributions of micro-scale effects (Section 2.2.1) that propagate to the macro scale by changing the behaviour of the fluids and the mathematical formulations on the macro scale. For details, the reader is referred to general textbooks such as *Bear* (1972); *Helmig* (1997); *Pinder and Celia* (2006); *Nordbotten and Celia* (2012).

2.2.1 Scales and domains

In this work, three scales are explicitly defined. Firstly, on the micro scale, detailed knowledge of the spatial distribution of liquid and solid phases and their interfaces is available and mass exchange is observable. This scale is nevertheless large enough that the fluids can be described as a continuum with ensemble measures such as density, and not by individual molecules. Secondly, on the macro scale or REV scale, the actual

configuration of the grains can be neglected and its effects are up-scaled into averaged quantities that are valid throughout a "representative elementary volume" (REV). At this scale, the fluctuations of the properties (such as porosity, Figure 2.2) cedes with respect to an increase in scale size (*Hubbert*, 1956). Hence within each REV, it is assumed that there are only homogeneous effective parameters that capture all relevant processes. Finally, the field scale is the scale of the modelling domain that needs to be solved for and which is discretised by the simulation grid.

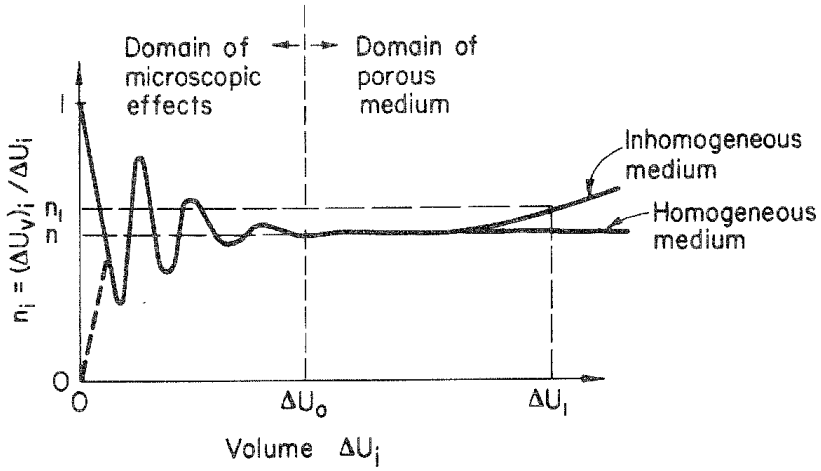

Figure 2.2: The fluctuations of porosity, denoted by n_i, over observation volume, here ΔU_i, cedes if the REV is reached (*Bear*, 1972).

Heterogeneities exist on the entire range of scales, so soil parameters vary as well: fractures, for example, are breaks in rocks that strongly influence subsurface flow and appear at every length scale (*Dietrich et al.*, 2005). The host rock is heterogeneous as well, through layering or inclusions of different material, which yields complex flow regimes that even lead to model inconsistencies on a variety of length scales (e.g. *Miller et al.* (1998); *Helmig et al.* (2006)).

Simulation on an adaptive grid introduces additional sub-scales on the field scale, as the discretisation length is modified: a fine scale representing the maximum resolution of the grid versus a coarse scale, including potential intermediate scales. Then again, the effective parameters have to be carefully determined for each of these sub-scales to allow for the fine-scale information to propagate to the coarser scale ("up-scaling") and vice versa ("down-scaling"). This is especially the case if the soil is heterogeneous on all levels, which leads to a broad field of research dedicated to up-scaling techniques to resolve

permeability (*Renard and De Marsily*, 1997; *Durlofsky*, 2005), relative permeability functions (*Barker and Thibeau*, 1997; *Darman et al.*, 2002) or flow functions *Stone* (1991) at different scales. These coarse-scale models can even include patterns of flow specific to the fine scale such as fingering (*Artus and Noetinger*, 2004) or compositional effects (*Binning and Celia*, 2008; *Salehi et al.*, 2013) by effective up-scaled quantities. The aforementioned methods are circumvented in this work by defining the soil properties and corresponding flow functions on the coarsest scale, thus no up-scaling of parameters is necessary.

The spatial domain can be divided into several units on the field scale. Possible criteria might be rock properties (for CO_2 storage, for example, the injection formation and a sealing cap-rock above), specifics of fluids (dependent on the amount of different phases present) or the applied numerical scheme. A combination of the latter two is undertaken in Chapter 4. The differently classified and non-overlapping subdivisions are denoted as "sub-domains".

2.2.2 Porosity and saturation

A porous medium is a solid material composed of grains and pores. The size and connectivity of the open void space is dependent on the variability in grain size and their geometric packing within the porous structure. The fraction of the void volume V_v that is accessible by fluids over the total volume defines the porosity

$$\phi = \frac{V_v}{\hat{V}} \, .$$

If several fluid phases are present in the rock, each fluid phase occupies a certain ratio of the available pore space

$$S_\alpha = \frac{V_\alpha}{V_v} \, . \tag{2.36}$$

On the REV scale, the exact spatial distribution of the fluid phases in the pore matrix is irrelevant. The saturation is thus an integral measure that is averaged over the REV (Figure 2.3).

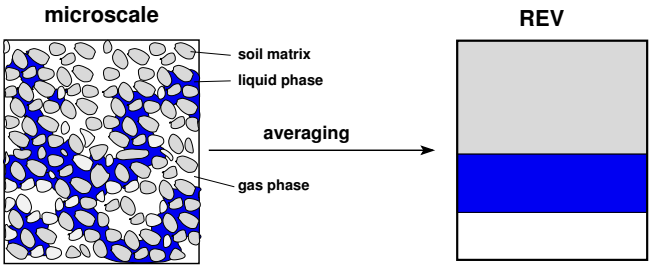

Figure 2.3: Averaging from micro-scale to macro-scale (*Class*, 2008).

2.2.3 Intrinsic permeability

The French engineer Henry Darcy investigated the seepage of water through a sand column already in the 19th century. He found that the total discharge, Q, is proportional to the cross-sectional area of the column, A and the gradient in hydraulic head, h, which can be expressed as

$$Q = -k_f A \frac{\Delta h}{l} \ . \tag{2.37}$$

The proportionality factor, k_f, was described by Darcy as "a coefficient dependent on the permeability of the [sand] layer" (*Hubbert*, 1956). The hydraulic head h is the sum of the geodetic height, z, and the pressure head, $\frac{p}{\varrho g}$. *Hubbert* (1956) accompanied Darcy's experimental analysis with a mathematical derivation, and concluded that k_f is indeed a lumped parameter of both soil and fluid properties

$$k_f = K \frac{\varrho g}{\mu} \ , \tag{2.38}$$

where K is now purely a soil property and thus denoted intrinisic permeability. A widely accepted relation of the intrinsic permeability and porosity is the Kozemy-Carman equation (*Bear*, 1972),

$$K = \frac{\bar{d}^2}{180} \frac{\phi^3}{(1-\phi^2)} \ , \tag{2.39}$$

where $\bar{d}$ is the mean particle size of the porous medium. The pores of a porous medium are, in general, neither well-sorted and homogeneously packed nor of uniform shape, so the resistance to fluid flow varies with the spatial direction. Hence, intrinsic permeability is a tensorial quantity $\mathbf{K}$. Whenever only one scalar value is given in this work, this implies equal diagonal entries and zero non-diagonal entries of the full permeability tensor.

2.2.4 Capillary Pressure

Molecules inside a fluid phase are subject to intermolecular forces, acting equally in all directions. At the phase interface, however, these forces are not balanced if the attractive force differs in each phase. This leads to a so-called surface tension that minimises the surface of a phase under multiphase conditions. In a porous medium, the fluids also interact with the solid matrix, so further adhesive and repulsive forces with the grain surface are present. The chemical composition of the solid and fluids determine which of the fluids wet the surface, which leads to the terms "wetting" ($\alpha = w$) and "non-wetting" ($\alpha = n$) phase. In real systems, however, even mixed-wet porous media exist (*Doerr et al.*, 2000) where such a distinction is non-trivial.

As the wetting phase spreads over the grain surface, the interface bends under stress. This leads to a pressure difference on either side of the interface (*Pinder and Celia*, 2006), which is called capillary pressure p_c. While originally a micro-scale phenomenon, the effect of capillarity propagates to the macro scale: as an example, let us consider a water-wet soil sample where the initial water is replaced by injecting a non-wetting gas with an overpressure. For each pore, this overpressure has to overcome the "entry pressure" p_d necessary to displace the wetting phase that is preferentially attracted by the solid. The higher the overpressure becomes, even smaller pores with increasingly high entry pressures get occupied. This difference in phase pressures on the macro scale,

$$p_c = p_n - p_w \ , \tag{2.40}$$

is again called capillary pressure, and represents a quantity that is averaged over the REV to mimic the macro-scale behaviour. Due to its correlation with the water content, the macro-scale capillary pressure is incorporated by its functional dependency on the saturation via a $p_c(S)$-relationship. In the example, the overpressure will rise until a limit is reached where no further water drains the sample. This limit is the residual saturation S_{wr}, that has its analogue (S_{nr}) for the inverse process, imbibition, when no more non-wetting fluid can be replaced by pressure gradients. The constitutive relation for the macro-scale capillary pressure with the saturation is thus typically formulated in terms of the effective saturation S_e,

$$S_e = \frac{S_w - S_{wr}}{1 - S_{wr}} \tag{2.41}$$

Widely used capillary-pressure–saturation relationships are formulated by Brooks-Corey and Van Genuchten.

$$\text{Brooks-Corey:} \quad p_c(S_w) = p_d S_e^{-\frac{1}{\lambda}} ; \qquad \text{for } p_c \geq p_d \tag{2.42}$$

$$\text{Van Genuchten:} \quad p_c(S_w) = \frac{1}{\alpha}\left(S_e^{-\frac{1}{m}} - 1\right)^{\frac{1}{n}} ; \quad \text{for } p_c \geq 0 \tag{2.43}$$

The parameters p_d and λ as well as n, m and α are determined by fitting curves to experimental data or numerical simulations performed on the micro or pore scale. It is noted here that there is a dependency of capillary pressure on temperature and even composition that is not considered in this work. Likewise neglected is the dependency on flow rate and relative direction of flow, and the history of the change in saturation (hysteresis).

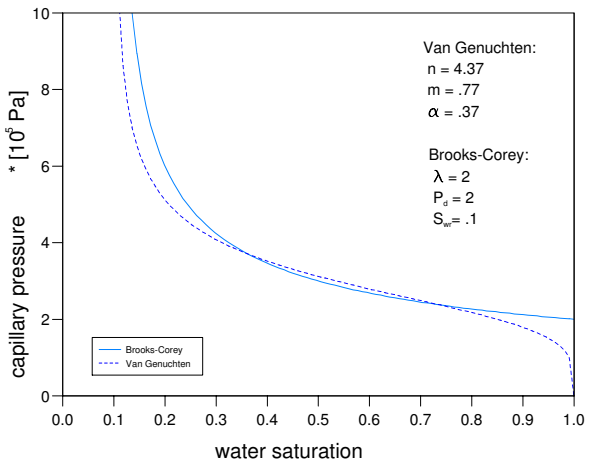

Figure 2.4: Capillary-pressure–saturation relationships (*Helmig*, 1997).

2.2.5 Multiphase Darcy's law and relative permeability

Under multiphase conditions, each phase occupies only a fraction of the available pore space, expressed by the saturation S_α. In motion, each fluid finds its own pathway through a set of channels that depends on the saturation (*Bear et al.*, 1968). The reduction of discharge caused by such a channelling is quantified by introducing a

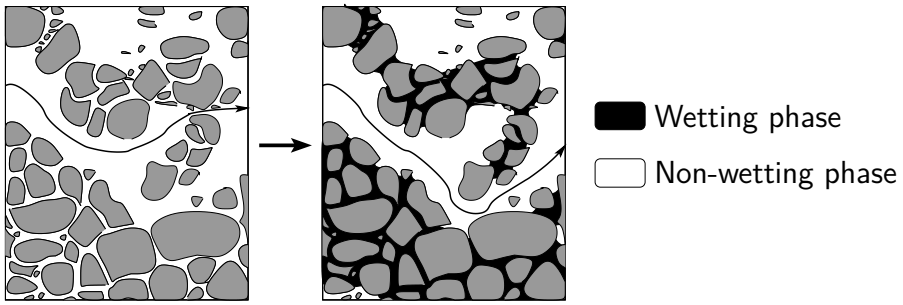

Figure 2.5: Fluid movement in porous matrix under singlephase (left) and under multiphase (right) condition.

relative permeability function that is dependent on saturation. This function equals the single-phase discharge in Equation (2.37) if the saturation approaches unity (Fig 2.5). The considerations in Section 2.2.4 allow for different pressures in each phase, which lead to the extended form of multiphase DARCY's law (*Pinder and Celia*, 2006; *Helmig*, 1997),

$$\mathbf{v}_\alpha = -\mathbf{K}\frac{k_{r\alpha}}{\mu_\alpha}(\nabla p - \varrho_\alpha \mathbf{g}) \;, \tag{2.44}$$

where the fraction of permeability and viscosity is usually abbreviated by the mobility $\lambda_\alpha = {}^{k_{r\alpha}}/_{\mu_\alpha}$. Although Equation (2.44) is written and widely applied as a phase velocity $\mathbf{v}_\alpha$, the quantity itself resembles more the volume-specific discharge $q_\alpha = \frac{Q_\alpha}{A} := \mathbf{v}_\alpha$. Functions of relative permeability can either be measured or derived from the applied capillary-pressure–saturation relationships (*Pinder and Celia*, 2006; *Helmig*, 1997). VAN-GENUCHTEN used the MUALEM model,

$$k_{rw} = \sqrt{S_e}\left[1 - \left(1 - S_e^{\frac{1}{m}}\right)^m\right]^2 \tag{2.45a}$$

$$k_{rn} = (1 - S_e)^{\frac{1}{3}}\left[1 - S_e^{\frac{1}{m}}\right]^{2m} \tag{2.45b}$$

and BROOKS-COREY the model of BURDINE,

$$k_{rw} = S_e^{\left(\frac{2+3\lambda}{\lambda}\right)} \tag{2.46a}$$

$$k_{rn} = (1 - S_e)^2\left[1 - S_e^{\left(\frac{2+\lambda}{\lambda}\right)}\right] \tag{2.46b}$$

2.2.6 Heat conductivity

Under non-isothermal conditions, temperature differences induce the conduction of heat, a diffusive flux of energy driven by temperature differences. FOURIER's law relates the heat flux $\mathbf{J}_{E,\alpha}$ to a material parameter $\lambda_{E,\alpha}$ and the gradient in temperature,

$$\mathbf{J}_{E,\alpha} = -\lambda_{E,\alpha} \nabla T_\alpha \tag{2.47}$$

The heat conductivity of the material, $\lambda_{E,\alpha}$, quantifies the ability to transport heat. As this transport happens between individual molecules, heat conductivity is larger in solids than in gases. In a multi-phase environment, heat transport is a rather complex process, thus integral measures of a combined multi-phasic conductivity $\bar{\lambda}_E$ are preferred (e.g. *Class* (2008)). The model of SOMERTON considers the contribution of the water by a root function,

$$\bar{\lambda}_E = \lambda_{E,s} + \sqrt{S_w}(\lambda_{E,w} - \lambda_{E,s}) \tag{2.48}$$

2.3 Balance equations

The previous sections describe the state of the fluids (Section 2.1) and their interplay with the porous media (Section 2.2). The governing equations on the REV scale are conservation laws that preserve mass, energy and momentum. The latter is usually omitted in the field of porous media, as the applied DARCY's law for flow in its range of applicability can substitute a general consideration of the momentum balance. The derivation of the following equations can be found in (*Helmig*, 1997; *Bielinski*, 2006; *Fritz*, 2010).

2.3.1 Mass balance

Considering compositional multiphase flow in porous media, the conservation of mass can be formulated for each component κ in the phases α

$$\sum_\alpha \frac{\partial(\phi S_\alpha \varrho_\alpha X_\alpha^\kappa)}{\partial t} + \nabla \cdot \left(\sum_\alpha X_\alpha^\kappa \varrho_\alpha \mathbf{v}_\alpha + \mathbf{J}_\alpha^\kappa \right) + q^\kappa = 0 \, . \tag{2.49}$$

The first term comprises the changes of mass per REV over time and is called a storage term. Fluxes to and out of the volume are considered next, expressed by a combination of advective fluxes in terms of a phase flux (Equation (2.44)) and diffusive fluxes $\mathbf{J}_\alpha^\kappa$. Sources or sinks are accounted for by the third term.

2.3.2 Energy balance

Under the assumption of local thermodynamic equilibrium, energy is conserved if

$$\frac{\partial \left(\phi \sum_\alpha S_\alpha \varrho_\alpha u_\alpha + (1-\phi)\varrho_s c_s T\right)}{\partial t} + \nabla \cdot \left(\sum_\alpha (h_\alpha \varrho_\alpha \mathbf{v}_\alpha + \sum_\kappa u_\alpha^\kappa \mathbf{J}_\alpha^\kappa - \bar{\lambda}_E \nabla T) \right) + q^E = 0 \; . \tag{2.50}$$

The storage term in the energy balance comprises both the energy stored in all fluids and in the solid phase. Thermal convection comprises the heat transport through advective and diffusive fluxes as they appeared in the mass balance equation, supplemented by the conductive heat flux (Section 2.2.6).

3 Numerical models

In the 1970s, the simplified RICHARDS equation commonly applied to describe multi-phase flow in hydrology was gradually replaced by solving the conservation equations (Section 2.3), where experience in their solution was gained in the field of petroleum engineering (*Morel-Seytoux*, 1973). The numerical solution in time of these coupled non-linear partial differential equations can be assorted into two groups: the sequential or decoupled solution strategies widely applied in petroleum engineering on one side and fully implicit or coupled solution strategies on the other side. The latter approach regards all dependencies in one large and coupled system of equations that is solved iteratively, until a converged solution is found. In the former method, in contrast, the system of equations is reformulated into subsequent computational steps, so the solution has not necessarily converged. The increase in efficiency therein comes with the price of severe constraints with regards to applicability of such a decoupled solution.

The basic assumptions made to develop the numerical models are summarized briefly:

- Molecular diffusion and hydrodynamic dispersion is neglected, i.e. $\mathbf{J}_\alpha^\kappa = 0$, because this works focus lies on advectively dominated processes where diffusion plays a minor role. Although being a diffusive effect, the heat conduction along a temperature gradient is regarded.

- Flow through the porous medium is assumed to be slow enough that the phase flux can be approximated with DARCY's law, (2.44).

- Mass and energy transfer is considered fast enough that the thermodynamic equilibrium is reached locally. The global system can nevertheless deviate from an equilibrium state.

- The porous medium is rigid, thus its properties remain constant in time.

3.1 Implicit versus explicit solution

For brevity, the balance equations (Section 2.3) can be reformulated formally as a system of equations with the form

$$\frac{\partial \boldsymbol{\chi}}{\partial t} = \boldsymbol{F}(\boldsymbol{\chi}) \tag{3.1}$$

where the vector $\boldsymbol{\chi}$ holds all primary variables. The time derivative in Equation (3.1) requires a discretisation in time by means of a finite number of time-steps. The last known state is denoted by the superscript $t - \Delta t$, and a solution of the next time level t is seeked. Unfortunately, both primary variables $\boldsymbol{\chi}$ and the coefficient functions in $\boldsymbol{F}(\boldsymbol{\chi})$ change with time. An implicit scheme (Figure 3.1(a)) examines the coefficients on the new time level,

$$\frac{\boldsymbol{\chi}^t - \boldsymbol{\chi}^{t-\Delta t}}{\Delta t} = \boldsymbol{F}^{t-\Delta t,t}(\boldsymbol{\chi}^t) \tag{3.2}$$

An iterative scheme is necessary because the right hand side also depends on the solution of $\boldsymbol{\chi}^t$ itself.

In contrast, explicit schemes use the coefficients of the known last time level $t - \Delta t$ to compute the primary unknowns $\boldsymbol{\chi}^t$, assuming that the temporal change in $\boldsymbol{F}$ is sufficiently small:

$$\frac{\boldsymbol{\chi}^t - \boldsymbol{\chi}^{t-\Delta t}}{\Delta t} = \boldsymbol{F}^{t-\Delta t}(\boldsymbol{\chi}^{t-\Delta t}) \tag{3.3}$$

The explicit scheme features the advantage that the coefficients in $\boldsymbol{F}^{t-\Delta t}$ can be directly calculated and costly iteration is omitted. For stability reasons, the size of the time-step is limited by a stability criterion that was found by *Courant, Friedrichs, and Lewy* (1928) and is accordingly named CFL-criterion. It connects the temporal and spatial resolution of the discretisation by introducing a domain of dependence in space-time, depicted in grey in Figure 3.1(b). Outside this domain, a front would pass more than one cell per time-step, which would surpass the spacial discretisation length of the new time-step and thus could not be captured. In one dimension and obeying a spatial discretisation length Δx, the CFL-criterion is

$$\frac{|\mathbf{v}|\Delta t}{\Delta x} \leq 1 \tag{3.4}$$

$$\frac{|\mathbf{v}|\Delta t}{\Delta x} = a \cdot 1 \tag{3.5}$$

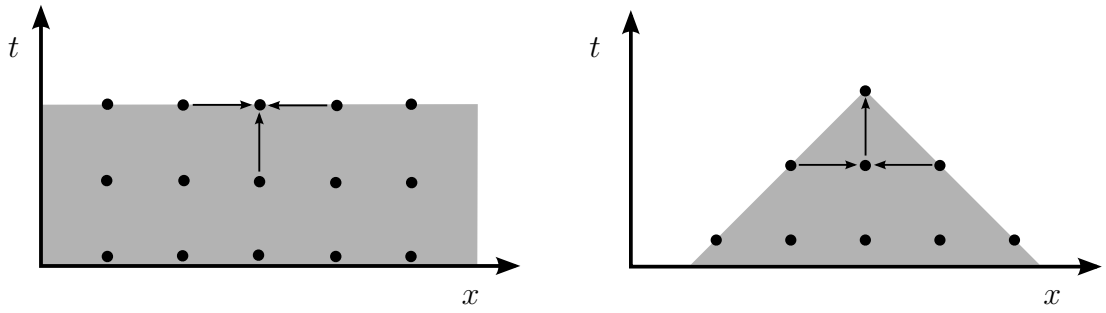

(a) Implicit solution. (b) Explicit solution.

Figure 3.1: Schematic of implicit and explicit solution of transient flow problems.

The inequality is usually ensured by introducing a factor a (Equation (3.5)) that further reduces the size of the time-step to stay on the safe side.

3.1.1 Fully implicit or coupled solution

The balance equations of Section 2.3 are coupled via the $p_c - S$–relationship, the phase mobility, density, the phase composition as well as caloric quantities. Fully implicit solution schemes seek a converged solution of the next time-step by iterating Equation (3.2) until all conservation equations are fulfilled, i.e. the equality is met to a certain tolerance. The secondary variables that appear in $\boldsymbol{F}$, the fluid properties and fluid-matrix interactions discussed in the last section, are dependent on the unknowns of the new time level $\boldsymbol{\chi}^t$, and on the old time level $\boldsymbol{\chi}^{t-\Delta t}$ if they appear in the storage term. To reach convergence, an iterative scheme such as the Newton-Rapson-method is used (*Helmig*, 1997; *Class*, 2008). Therein, the change of $\boldsymbol{F}$ for changes in the primary unknowns $\boldsymbol{\chi}$, i.e. the Jacobian, has to be build for each iteration step, until a set of unknowns $\boldsymbol{\chi}^t$ is found that fulfils Equation (3.2) up to a low tolerance. The number of iterations necessary to reach convergence determines the size of the time-step, because the number of time-steps have to be balanced with the efforts to reach a converged solution.

Converging towards a solution of the overall system may be a cumbersome task, for example if local phase changes are triggered by only a margin (*Class and Helmig*, 2002). Of the various strategies to reach convergence (*Marchand et al.*, 2013) under such conditions, some apply a different choice of primary variables globally (*Neumann et al.*,

2013) or adapt them locally (*Class et al.*, 2002); alternative approaches even include a reformulation of the closure conditions that couple the balance equations (*Jaffré and Sboui*, 2010; *Lauser et al.*, 2011).

3.1.2 Decoupled or sequential solution

As early as the 1960s (*Aziz and Settari*, 1979), an alternative solution strategy to the fully implicit approach was applied in the petroleum literature, and was only gradually adopted by researchers in the field of hydrology (*Wooding and Morel-Seytoux*, 1976; *Binning and Celia*, 1999). The basic idea (*Stone and Jr.*, 1961) is to reformulate the coupled system of equations into one equation to determine the flow field and sequentially solved transport equations obeying that flow field. Such a splitting would allow for an explicit solution of the transport, i.e. solving the balance equations (Section 2.3) in the fashion of Equation (3.3). The flow field itself is deduced in terms of a pressure, the origin of the term "pressure equation", that can be both a physical quantity such as a phase pressure or a rather mathematical global pressure. This pressure equation is solved in a semi-implicit fashion: the pressure variable itself is solved implicitly, but the coefficients in $\boldsymbol{F}$, see Equation (3.2), are based on the solution of the old time level $t - \Delta t$. The combination of **i**mplicit **p**ressure and **e**xplicit transport of **s**aturation/**c**oncentrations is the reason this decoupled solution scheme is typically named IMPES or IMPEC scheme (*Sleep and Sykes*, 1993). I would prefer the term IMPET, because the **t**ransport is explicit regardless of the transported quantity, be it the transport of mass or energy.

A linearisation with the coefficients held constant in time becomes necessary because the pressure solve happens before the transport, so the transported quantities of the new time-level that appear in the coefficients are not yet known. Such a time-lagging of the coefficients is typically justified by the small size of the time-steps, that evolve because of the limitation imposed by the CFL-criterion. The changes in the transported quantities are then sufficiently small that the changes in the derived quantities are considered negligible during each time-step. This might be the case for an iso-thermal in-compressible system of fully immiscible phases with negligible capillary effects, where the system of equations is only weakly coupled through the mobility. The stronger the coupling, the stronger the change in the coefficients, which increases the truncation errors significantly, and eventually causes a failure of the splitting method.

To avoid such failure, the sequential solution scheme can be iterated (e.g. *Bell et al.* (1986); *Jarle Haukas and Reisoa* (2005); *Lu and Wheeler* (2009); *Moortgat et al.* (2011)). The iteration, however, comprises the advantage of the sequential solution method, its pure speed, while in general still being bound to its limitations through the CFL-factor. Plus, iteration is only meaningful if a truly converged solution can be found, which is exactly what the fully implicit methods are designed to accomplish, that are therefore performing better in strongly-coupled cases (*Forsyth Jr. and Sammon*, 1986). As mentioned in Section 3.1.1, even these fully implicit methods sometimes fail to converge, so non-iterative approaches provide a valuable alternative. Another alternative would be a combination of both a sequential and a fully implicit method (*Thomas and Thurnau*, 1983; *Forsyth Jr. and Sammon*, 1986), the adaptive implicit method.

The sequential solution scheme is the method of choice in this work, so it will be presented in detail in the following sections.

3.2 The sequential solution procedure

The chain of the sequential scheme applied in this work is sketched in Figure 3.2: after initialization of the problem, the time-stepping is started; a predictor transport step estimates the changes of the transported quantities per cell that are required to calculate the derivatives in fluid volume (Section 3.3.1) for the pressure equation (Section 3.2.2), that is solved thereafter; the flow field from the solved pressure equation is input for the transport system, that yields transport primary variables on the new time level; finally, flash calculations (Section 3.4.2) solve for the secondary variables, with which the output can be written and the next time-step is ready to be started.

3.2.1 Transport equations

An explicit transport of the conserved quantities is performed along a pressure field that specifies phase velocities. The transport equations are directly formulated from the balance equations (Section 2.3). In the compositional case considered here, the mass

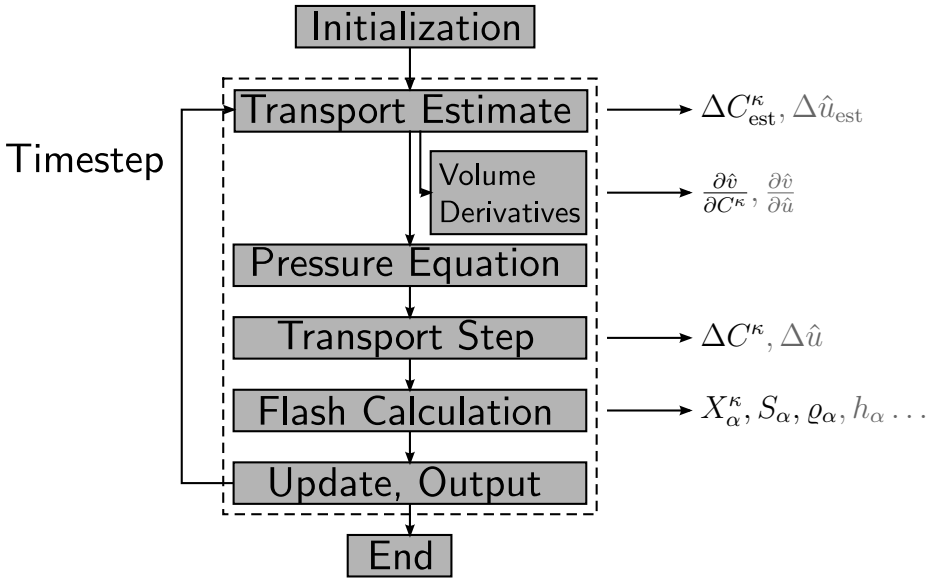

Figure 3.2: The sequential solution scheme, non-isothermal variables depicted in gray.

transport is accomplished for each conserved component κ per unit volume in terms of the total concentration C^κ (Section 2.1.1),

$$\frac{\partial C^\kappa}{\partial t} = -\nabla \cdot \left(\sum_\alpha X^\kappa_\alpha \varrho_\alpha \mathbf{v}_\alpha \right) - q^\kappa \, . \tag{3.6}$$

For non-isothermal systems, conservation of energy has to be included. An apparent choice as a primary variable emerges from the storage term of the energy balance Equation (2.50), the volume specific total internal energy $\hat{u} = \phi \sum_\alpha S_\alpha \varrho_\alpha u_\alpha + (1-\phi)\varrho_s c_s T$, that yields an energy transport equation of the form

$$\frac{\partial \hat{u}}{\partial t} = -\nabla \cdot \left(\sum_\alpha h_\alpha \varrho_\alpha \mathbf{v}_\alpha - \bar{\lambda}_E \nabla T \right) - q^E \, . \tag{3.7}$$

If changes in temperature or heat fluxes do not lead to phase changes, such as boiling, one can linearise Equation (3.7) and use the temperature instead of the internal energy as a primary variable (*Nordbotten and Celia*, 2012). At boiling conditions, however, enthalpy changes while the temperature remains constant, so linearisation fails as the heat capacity approaches infinity.

3.2.2 Pressure equation

The flow field required for the transport step is implicitly calculated in the sequential formulation by means of a single equation, the so-called "pressure equation".
The fractional flow formulation represents the traditional (e.g. *Helmig* (1997); *Aziz and Settari* (1979)) approach arising from a summation of the mass balance equations (2.49) over all components, exploiting Equation (2.3),

$$\frac{\partial(\phi S_\alpha \varrho_\alpha)}{\partial t} + \nabla \cdot (\varrho_\alpha \mathbf{v}_\alpha) + q_\alpha = 0 \,, \tag{3.8}$$

diffusive fluxes $\mathbf{J}_\alpha^\kappa$ are neglected for brevity. If changes of porosity in time are omitted, the product rule gives

$$\phi \left(\varrho_\alpha \frac{\partial S_\alpha}{\partial t} + S_\alpha \frac{\partial \varrho_\alpha}{\partial t} \right) + \varrho_\alpha \nabla \cdot \mathbf{v}_\alpha + \mathbf{v}_\alpha \cdot \nabla \varrho_\alpha + q_\alpha = 0 \,. \tag{3.9}$$

A division by the phase density then provides

$$\phi \left(\frac{\partial S_\alpha}{\partial t} + \frac{S_\alpha}{\varrho_\alpha} \frac{\partial \varrho_\alpha}{\partial t} \right) + \nabla \cdot \mathbf{v}_\alpha + \frac{\mathbf{v}_\alpha}{\varrho_\alpha} \cdot \nabla \varrho_\alpha + \frac{q_\alpha}{\varrho_\alpha} = 0 \,. \tag{3.10}$$

Equation (3.10) is now summed over all phases providing a single equation

$$\phi \left(\sum_\alpha \frac{\partial S_\alpha}{\partial t} + \sum_\alpha \frac{S_\alpha}{\varrho_\alpha} \frac{\partial \varrho_\alpha}{\partial t} \right) + \sum_\alpha \nabla \cdot \mathbf{v}_\alpha + \sum_\alpha \frac{\mathbf{v}_\alpha}{\varrho_\alpha} \cdot \nabla \varrho_\alpha + \sum_\alpha \frac{q_\alpha}{\varrho_\alpha} = 0 \,. \tag{3.11}$$

The first term drops out because the saturations sum up to unity. Equation (3.11) is usually further simplified by assuming an incompressible system,

$$\nabla \cdot \sum_\alpha \mathbf{v}_\alpha = - \sum_\alpha \frac{q_\alpha}{\varrho_\alpha} \,. \tag{3.12}$$

If capillary effects are not neglected, the term on the left-hand side contains as many unknown phase pressures as there are phases, which can not implicitly be solved for by means of one pressure equation. A reformulation is therefore necessary that introduces a "total velocity",

$$\hat{\mathbf{v}} = \sum_\alpha \mathbf{v}_\alpha = -\hat{\lambda} \boldsymbol{K} \left(\sum_\alpha f_\alpha \nabla p_\alpha - \sum_\alpha f_\alpha \varrho_\alpha \mathbf{g} \right) \,. \tag{3.13}$$

The total mobility $\hat{\lambda}$ represents the sum of the phase mobilities, and the fractional flow function, $f_\alpha = \lambda_\alpha / \hat{\lambda}$, was the reason the sequential solution approach is widely known under the name "fractional flow formulation".
In order to get one unique variable through the pressure equation (*Chen and Ewing*, 1997), the total velocity can be based on an artificial "global pressure" p_G, such that $\nabla p_G = \sum_\alpha f_\alpha \nabla p_\alpha$ and all phase pressures drop out of the pressure equation.
As an alternative ansatz, one phase pressure can be chosen as the primary variable and the remaining phase velocities are expressed by the gradients in the remaining phase pressures approximated by ∇p_c of the old time-level.

The volume balance formulation provides an alternative to the traditional fractional flow approach, which does not directly incorporate changes in composition that alter the fluid density. Such neglect increases the errors arising after the transport (*Fritz*, 2010) due to a change of fluid volume. *Ács et al.* (1985) proposed a pressure equation balancing the fluid volume instead of mass. This volume balance formulation is mathematically analysed in *Trangenstein and Bell* (1989); *Chen et al.* (2000). A similar pressure equation can be found in *Watts* (1986); *Coats* (2000). The derivation in this work follows *van Odyck et al.* (2008).

Porosity is defined as the void space in the porous medium that can be accessed by the fluids,

$$\hat{v} = \phi \,, \tag{3.14}$$

where $\hat{v} = \sum_\alpha v_\alpha [\mathrm{m}^3/\mathrm{m}^3]$ is the specific volume that is filled with fluids. To capture transient processes, the left hand side of this volume balance is approximated in time by a Taylor series, because the porosity is assumed constant in time,

$$\hat{v}\,(t) + \Delta t \frac{\partial \hat{v}}{\partial t} + \mathcal{O}\left(\Delta t^2\right) + \ldots = \phi \,. \tag{3.15}$$

If higher order terms are neglected, reordering yields

$$\frac{\partial \hat{v}}{\partial t} = \frac{\phi - \hat{v}}{\Delta t} \,. \tag{3.16}$$

This form of the pressure equation enforces a pressure such that the equation of state, given its truncation errors in time, will not deviate too much from the available pore space.

In the **isothermal** case, the fluid volume changes in time if there are variations of pressure or a change of mass, i.e. $\hat{v} = \mathrm{f}(p, C^\kappa)$

$$\frac{\partial \hat{v}}{\partial t} = \left.\frac{\partial \hat{v}}{\partial p}\right|_{C^\kappa} \frac{\partial p}{\partial t} + \sum_\kappa \left.\frac{\partial \hat{v}}{\partial C^\kappa}\right|_p \frac{\partial C^\kappa}{\partial t} \,. \tag{3.17}$$

Inserting the component transport equation (3.6) into Equation (3.17) and then into the volume balance (3.16) provides the pressure equation for isothermal systems,

$$\frac{\partial \hat{v}}{\partial p}\frac{\partial p}{\partial t} - \sum_\kappa \frac{\partial \hat{v}}{\partial C^\kappa} \nabla \cdot \left(\sum_\alpha X_\alpha^\kappa \varrho_\alpha \mathbf{v}_\alpha \right) - \sum_\kappa \frac{\partial \hat{v}}{\partial C^\kappa} q^\kappa = \frac{\phi - \hat{v}}{\Delta t} \,. \tag{3.18}$$

The first term in this pressure equation accounts for changes in fluid volume caused by pressure variations. It can be rewritten by means of the total compressibility $\hat{c} = \frac{\partial \hat{v}}{\partial p}$ of the fluid mixture. The following summands consists of the changes in fluid volume due to changes of composition, i.e. $\frac{\partial \hat{v}}{\partial C^\kappa} = \frac{\partial \hat{V}}{\partial m^\kappa}$, and the local changes in mass due to fluxes through the cell interfaces, $\frac{\partial C^\kappa}{\partial t}$. The latter incorporates the multi-phase DARCY's law where gradients in pressure need a further discretisation in space.
The term on the right hand side of Equation (3.18) should cancel out if the volume constraint in Equation (3.14) is fulfilled. However, if the fluids involved are partially miscible and compressible and the changes in fluid density are not implicitly incorporated or otherwise iteratively solved for (see references in Section 3.1.2), there remains a residual

$$\epsilon = \frac{\phi - \hat{v}}{\Delta t} \,, \tag{3.19}$$

which will be discussed in detail in Section 3.3.2.

In **non-isothermal** cases where the energy fluxes are significant enough to be balanced, the specific fluid volume is also a function of internal energy, $\mathrm{f}(p, C^\kappa, \hat{u})$,

$$\frac{\partial \hat{v}}{\partial t} = \left.\frac{\partial \hat{v}}{\partial p}\right|_{C^\kappa, \hat{u}} \frac{\partial p}{\partial t} + \sum_\kappa \left.\frac{\partial \hat{v}}{\partial C^\kappa}\right|_{p, \hat{u}} \frac{\partial C^\kappa}{\partial t} + \left.\frac{\partial \hat{v}}{\partial \hat{u}}\right|_{p, C^\kappa} \frac{\partial \hat{u}}{\partial t} \,. \tag{3.20}$$

Inserting the transport equations ((3.6), (3.7)) yields the pressure equation for non-

isothermal systems,

$$\hat{c}|_{C^\kappa,\hat{u}}\frac{\partial p}{\partial t} - \sum_\kappa \frac{\partial \hat{v}}{\partial C^\kappa}\nabla\cdot\left(\sum_\alpha X_\alpha^\kappa \varrho_\alpha \mathbf{v}_\alpha\right) + \frac{\partial \hat{v}}{\partial \hat{u}}\nabla\cdot\left(\sum_\alpha h_\alpha \varrho_\alpha \mathbf{v}_\alpha - \bar{\lambda}_E \nabla T\right) = \sum_\kappa \frac{\partial \hat{v}}{\partial C^\kappa} q^\kappa + \varepsilon, \tag{3.21}$$

The phase velocity is again subject to all phase pressures, so the system has to be reduced to one primary pressure variables to be solved for. It is possible to use the same formulations that are possible for the fractional flow formulation and described in detail in (*Chen et al.*, 2000). Following (*Fritz*, 2010), the phase pressure formulation is preferred over a global pressure in this work because phase pressures are natural quantities to enter the EOS and no special iteration schemes (*Binning and Celia*, 1999) are required on the boundary. Plus, models based on global pressures may produce erroneous results with regards to up-winding (Section 3.3.3) in heterogeneous porous media (*Tveit and Aavatsmark*, 2012).

3.3 Discretisation of the governing equations

3.3.1 Discretisation in space and time

The transport equations (3.6, 3.7) and the pressure equations (3.18, 3.21) are discretised in space by a cell centred finite volume method. Subdivision of the global simulation domain yields the finite volumes or cells i, that are connected via a interface γ of volume A_γ with their neighbours j if the cell does not lie on the boundary. The discretisation points live in the cell center, and the fluid properties are assumed to be constant throughout the cell volume V_i.

The normal vector that appears when replacing volume integrals of divergence terms by fluxes over the discrete interface, $\int_i \nabla\cdot(.) = \oint_\gamma \mathbf{n}\cdot(.) = \sum_\gamma A_\gamma \mathbf{n}\cdot(.)$ would undermine gravitational fluxes if γ lies in accordance to the gravity vector $\mathbf{g}$ in a skewed configuration of the grid. It is thus extended by the normalized vector $\mathbf{d}_{ij} = \frac{\mathbf{x}_j - \mathbf{x}_i}{\Delta x}$ connecting the position vectors $\mathbf{x}$ of the adjacent cells scaled by their centres' distance $\Delta x = |\mathbf{x}_j - \mathbf{x}_i|$.

Adopted for the DARCY flux in (2.44), the extension yields in the case of a linear two-point approximation of the gradient in phase pressure, $\nabla p_\alpha = \frac{p_j - p_i}{\Delta x}\mathbf{d}_{ij}$,

$$\mathbf{n} \cdot \mathbf{v}_\alpha = \mathbf{n}_\gamma^T \boldsymbol{K} \mathbf{d}_{ij} \lambda_\alpha \left(\frac{p_{\alpha,j}^t - p_{\alpha,i}^t}{\Delta x} - \varrho_\alpha \mathbf{g}^T \mathbf{d}_{ij} \right) . \tag{3.22}$$

An expression in the form of Equation (3.22) can alternatively be gained by reforming the influence of gravity in the DARCY velocity: first, the deepness z is introduced, which holds the z-coordinate of the position vector $\mathbf{x}$. Using the gravity as a scalar value g, under the assumption that the gravity acts only in the z-direction, Equation (2.44) can be written as

$$\mathbf{v}_\alpha = -\boldsymbol{K} \frac{k_{r\alpha}}{\mu_\alpha} (\nabla p - \varrho_\alpha g \nabla \mathsf{z}) . \tag{3.23}$$

A two-point approximation of all gradients then yields

$$\mathbf{n} \cdot \mathbf{v}_\alpha = \mathbf{n}_\gamma^T \boldsymbol{K} \mathbf{d}_{ij} \lambda_\alpha \left(\frac{p_{\alpha,j}^t - p_{\alpha,i}^t}{\Delta x} - \varrho_\alpha g \frac{\mathsf{z}_j - \mathsf{z}_i}{\Delta x} \right) , \tag{3.24}$$

which equals Equation (3.22).

The transport system approximates the change in mass ΔC_i^κ over the next time-step for each cell i by applying Equation (3.22) on Equation (3.6),

$$\frac{\Delta C_i^\kappa}{\Delta t} = \sum_\gamma \frac{A_\gamma}{V_i} \mathbf{n}_\gamma^T \boldsymbol{K} \sum_\alpha \varrho_\alpha \lambda_\alpha \mathbf{d}_{ij} \left(\frac{p_{\alpha,j}^t - p_{\alpha,i}^t}{\Delta x} - \varrho_\alpha \mathbf{g}^T \mathbf{d}_{ij} \right) X_\alpha^\kappa - q_i^\kappa . \tag{3.25}$$

The energy transport is formulated analogously

$$\frac{\Delta \hat{u}_i}{\Delta t} = \sum_\gamma \frac{A_\gamma}{V_i} \left[\mathbf{n}_\gamma^T \boldsymbol{K} \sum_\alpha \varrho_\alpha \lambda_\alpha \mathbf{d}_{ij} \left(\frac{p_{\alpha,j}^t - p_{\alpha,i}^t}{\Delta x} - \varrho_\alpha \mathbf{g}^T \mathbf{d}_{ij} \right) h_\alpha - \mathbf{n}_\gamma^T \mathbf{d}_{ij} \bar{\lambda}_E \frac{T_j - T_i}{\Delta x} \right] - q_i^E . \tag{3.26}$$

A simple CFL-like criterion, discussed in detail in Section 3.3.4, determines the size of the time-step Δt. Then, the changes in mass per cell ΔC^{κ_i} are used explicitly to calculate a set of total concentrations $C^{\kappa,t}$ on the new time level t,

$$C^{\kappa,t} = C^{\kappa,t-\Delta t} + \Delta t \cdot \Delta C_i^\kappa \tag{3.27}$$

$$\hat{u}^t = \hat{u}^{t-\Delta t} + \Delta t \cdot \hat{u}^t . \tag{3.28}$$

The pressure equations ((3.18) and (3.21)) have to be discussed in more detail than the straightforward transport step, because the volume derivatives that appear in contrast to the traditional fractional flow formulation (3.11) require special care. This can be exemplified by the iso-thermal pressure equation (3.18), with special focus on the integral of the divergence term. When integrated over the control volume G with surface Γ and its normal $\mathbf{n}_\Gamma$, the pressure equation reads

$$\int_G \frac{\partial \hat{v}}{\partial p}\frac{\partial p}{\partial t} dG - \int_G \sum_\kappa \frac{\partial \hat{v}}{\partial C^\kappa} \nabla \cdot \sum_\alpha X_\alpha^\kappa \varrho_\alpha \mathbf{v}_\alpha dG - \int_G \sum_\kappa \frac{\partial \hat{v}}{\partial C^\kappa} q^\kappa dG = \int_G \varepsilon dG \,, \tag{3.29}$$

$$\text{with } \int_G \sum_\kappa \frac{\partial \hat{v}}{\partial C^\kappa} \nabla \cdot \sum_\alpha X_\alpha^\kappa \varrho_\alpha \mathbf{v}_\alpha dG = \oint_\Gamma \sum_\kappa \frac{\partial \hat{v}}{\partial C^\kappa} \mathbf{n}_\Gamma \sum_\alpha X_\alpha^\kappa \varrho_\alpha \mathbf{v}_\alpha d\Gamma - \int_G \sum_\kappa \nabla \frac{\partial \hat{v}}{\partial C^\kappa} \cdot \sum_\alpha X_\alpha^\kappa \varrho_\alpha \mathbf{v}_\alpha dG. \tag{3.30}$$

The volume integral on the right-hand side of Equation (3.30) can only be neglected in slightly compressible systems (*Pau et al.*, 2012), because the volume derivatives can then be considered piecewise constant in each cell. For other cases, *Fritz et al.* (2012) proposed to subdivide each discrete cell i into one sub-volume per interface γ that is scaled by the face area A_γ and the cells surface area $U_i = \sum_\gamma A_\gamma$. The volume integral with the gradient in volume derivatives is thus replaced by a summation of these sub-volumes $\sum_\gamma \frac{A_\gamma}{U_i} \cdot V_i$. In each of these sub-volumes, the gradient of each volume derivative is approximated linearly between the discrete values in cell i and j, and the remaining flux-expressions in the volume integral equal those in the boundary integral.

In the finite volume context, the total compressibility $\hat{c} = \frac{\partial \hat{v}}{\partial p}$, sources q^κ and the error term ε are considered piecewise constant per volume G so that the integrals can be evaluated by multiplying the terms with the volume V_i of the cell i that relates to G. In the standard case, see the discussion in Section 5.4, the gradients are approximated linearly between cell i and j. The pressure equation in terms of phase pressures is then discretised implicitly in pressure p_α^t(Section 3.1.2), but all coefficients are calculated on

the old time-level $t - \Delta t$,

$$\begin{aligned} V_i \hat{c}_i \frac{p_i^t - p_i^{t-\Delta t}}{\Delta t} \\ + \sum_{\gamma_{ij}} A_{\gamma_{ij}} \mathbf{n}_{\gamma_{ij}}^T \boldsymbol{K} \sum_\alpha \varrho_\alpha \lambda_\alpha \mathbf{d}_{ij} \left(\frac{p_{\alpha,j}^t - p_{\alpha,i}^t}{\Delta x} - \varrho_\alpha \mathbf{g}^T \mathbf{d}_{ij} \right) \sum_\kappa X_\alpha^\kappa \frac{\partial \hat{v}}{\partial C^\kappa} \\ - \sum_{\gamma_{ij}} V_i \frac{A_{\gamma_{ij}}}{U_i} \mathbf{d}_{ij}^T \boldsymbol{K} \sum_\alpha \varrho_\alpha \lambda_\alpha \mathbf{d}_{ij} \left(\frac{p_{\alpha,j}^t - p_{\alpha,i}^t}{\Delta x} - \varrho_\alpha \mathbf{g}^T \mathbf{d}_{ij} \right) \sum_\kappa X_\alpha^\kappa \frac{\frac{\partial \hat{v}_j}{\partial C_j^\kappa} - \frac{\partial \hat{v}_i}{\partial C_i^\kappa}}{\Delta x} \\ = V_i \sum_\kappa \frac{\partial \hat{v}}{\partial C^\kappa} q_i^\kappa + V_i \varepsilon. \end{aligned} \tag{3.31}$$

The pressure equation can only be solved for one pressure that has to be specified a priori if capillary pressure couples the phase pressures. If a phase pressure is selected, such as p_n, the phase fluxes of a two-phase system are formulated in terms of this pressure,

$$\mathbf{v}_w = -\lambda_w \boldsymbol{K} (\nabla p_n - \nabla p_c - \varrho_w \mathbf{g}) \tag{3.32}$$

$$\mathbf{v}_n = -\lambda_n \boldsymbol{K} (\nabla p_n - \varrho_n \mathbf{g}) \, . \tag{3.33}$$

This determination of one phase pressure also specifies the storage or compressibility term in equation (3.31), which then yields in combination with Equations ((3.32) and (3.33)) for two phases and p_n as primary unknown

$$\begin{aligned} V_i \hat{c}_i \frac{p_{n,i}^t}{\Delta t} + \sum_{\gamma_{ij}} A_{\gamma_{ij}} \mathbf{n}_{\gamma_{ij}}^T \boldsymbol{K} \sum_\alpha \varrho_\alpha \lambda_\alpha \mathbf{d}_{ij} \frac{p_{n,j}^t - p_{n,i}^t}{\Delta x} \sum_\kappa X_\alpha^\kappa \frac{\partial \hat{v}}{\partial C^\kappa} \\ - \sum_{\gamma_{ij}} V_i \frac{A_{\gamma_{ij}}}{U_i} \mathbf{d}_{ij}^T \boldsymbol{K} \sum_\alpha \varrho_\alpha \lambda_\alpha \mathbf{d}_{ij} \frac{p_{n,j}^t - p_{n,i}^t}{\Delta x} \sum_\kappa X_\alpha^\kappa \frac{\frac{\partial \hat{v}_j}{\partial C_j^\kappa} - \frac{\partial \hat{v}_i}{\partial C_i^\kappa}}{\Delta x} \\ = - \sum_{\gamma_{ij}} A_{\gamma_{ij}} \mathbf{n}_{\gamma_{ij}}^T \boldsymbol{K} \left[\left(\sum_\alpha \varrho_\alpha \lambda_\alpha \mathbf{d}_{ij} \varrho_\alpha \mathbf{g}^T \mathbf{d}_{ij} \right) + \varrho_w \lambda_w \mathbf{d}_{ij} \frac{p_{c,j} - p_{c,i}}{\Delta x} \right] \sum_\kappa X_\alpha^\kappa \frac{\partial \hat{v}}{\partial C^\kappa} \\ + \sum_{\gamma_{ij}} V_i \frac{A_{\gamma_{ij}}}{U_i} \mathbf{d}_{ij}^T \boldsymbol{K} \left[\left(\sum_\alpha \varrho_\alpha \lambda_\alpha \mathbf{d}_{ij} \varrho_\alpha \mathbf{g}^T \mathbf{d}_{ij} \right) + \varrho_w \lambda_w \mathbf{d}_{ij} \frac{p_{c,j} - p_{c,i}}{\Delta x} \right] \sum_\kappa X_\alpha^\kappa \frac{\frac{\partial \hat{v}_j}{\partial C_j^\kappa} - \frac{\partial \hat{v}_i}{\partial C_i^\kappa}}{\Delta x} \\ - V_i \hat{c}_i \frac{p_{n,i}^{t-\Delta t}}{\Delta t} + V_i \sum_\kappa \frac{\partial \hat{v}}{\partial C^\kappa} q_i^\kappa + V_i \varepsilon. \end{aligned} \tag{3.34}$$

This form of the pressure equation is ordered in the form $\boldsymbol{A}\boldsymbol{\chi} = \mathbf{r}$ that is solved implicitly

in the unknowns $\boldsymbol{\chi}$ but with the coefficients based on the time-level $t - \Delta t$. Selection of p_w as a primary unknown would replace the corresponding flux term on the ride-hand side of Equation (3.34) with

$$\dots \left[\dots - \varrho_n \lambda_n \mathbf{d}_{ij} \frac{p_{c,j} - p_{c,i}}{\Delta x} \right] \dots \tag{3.35}$$

According terms arise in three-phase systems under the influence of capillary pressure, because all three phase pressures need to be expressed in terms of the selected primary unknown. It is formulated here in terms of pressures on the old time-level, as there is no more one single p_c, but several capillary pressures depending on the conceptual model. For the exemplary case of p_g as primary pressure and the remaining phases β, this yields

$$\dots \left[\dots + \sum_\beta \varrho_\beta \lambda_\beta \mathbf{d}_{ij} \frac{(p_{\beta,j}^{t-\Delta t} - p_{g,j}^{t-\Delta t}) - (p_{\beta,i}^{t-\Delta t} - p_{g,i}^{t-\Delta t})}{\Delta x} \right] \dots \tag{3.36}$$

All derivatives of total fluid volume are calculated numerically (Section 3.3.5) based on a prediction step ("transport estimate") using the pressure field of the old time-step $t - \Delta t$. This estimate also defines the upwind directions, see Section 3.3.3.

3.3.2 Volume error term in the pressure equation

After each time-step, the actual fluid volume at the given cell pressure does not necessarily match the available pore volume, because the flow field as well as the transport is not calculated with implicit coefficients. These approximation errors lead to a volume mismatch $(\phi - \hat{v})$ between fluid volume and available pore volume. The current fluid volume is based on the actual quantities C^κ that are present in the control volume combined with the EOS (densities ϱ_α) at the current state (p_α, T),

$$\hat{v} = \sum_\alpha v_\alpha = \left(\sum_\kappa C^\kappa \right) \cdot \sum_\alpha \frac{\nu_\alpha}{\varrho_\alpha} \tag{3.37}$$

To prevent this volume mismatch from building up over the next time-steps, the volumetric discrepancy enters the pressure equation as a source-term. This introduces pressure pulses in the subsequent transport to equal out the errors. Any variation of pressure, however, has a strong influence on the fluid properties, which means that such corrections in the pressure field have to be made with caution.

The volume errors are largest at saturation fronts, where the fluid properties change significantly per time-step. High volume errors introduce a strong correction of the pressure via ε. The induced fluxes might drastically reduce the size of the time-step, further boosting the pressure correction because the size of the time-step appears in the denominator of ε (Equation (3.19)). This can lead to strong oscillations in the pressure field (*Dicks*, 1993) up to a reversal of the flow direction that may terminate the simulation. Avoidance strategies might include significantly reducing the CFL-factor or application of iterative schemes, which both come with drastic losses in performance. Implicitly derived secondary variables might not be enough to stabilize the pressure system (*Dicks*, 1993) sufficiently. Alternatively, *Fritz* (2010); *Pau et al.* (2012); *van Odyck et al.* (2008) prevent abrupt changes in pressure by an artificial damping of the volume error term through a damping factor,

$$\varepsilon = a_\varepsilon \frac{\phi - \hat{v}}{\Delta t} \ . \tag{3.38}$$

This factor is determined heuristically and typically lies in the range between 0.2 and 0.8. After all, the semi-implicit solution framework produces very small volume discrepancies regularly throughout the simulation domain, which cancel out automatically in the course of following time-steps. *Fritz* (2010) proposed an error threshold $\underline{e}$ below which volume errors would not be considered at all for the error term ε in the pressure equation. From this lower bound $\underline{e}$, the error correction ramps up linearly until a specified upper bound $\overline{e}$ is reached and Equation (3.38) is applied, to prevent jumps in the error correction if lower bound is exceeded. This damping procedure is also applied in this work, and being sensitive on the problem at hand, the used values are listed for each simulation.

3.3.3 Flux approximation

In Section 3.3.1, the inter-cellular phase flux through interface γ was written as

$$f_\gamma = -\mathbf{n}_\gamma^T \boldsymbol{K} \sum_\alpha \varrho_\alpha \lambda_\alpha \mathbf{d}_{ij} \left(\frac{p^t_{\alpha,j} - p^t_{\alpha,i}}{\Delta x} - \varrho_\alpha \mathbf{g}^T \mathbf{d}_{ij} \right) \ . \tag{3.39}$$

This form anticipates that the flow is dependent on the information of the two cells adjoining the interface, a classical "two-point flux approximation" (TPFA, see Figure 3.3(a)). An increased flux stencil, a so-called "multi-point flux approximation" (MPFA)

can alternatively be used. Exemplarily, Figure 3.3(b) shows the widely applied "O-method". In order to discuss both approaches consecutively in the following paragraphs, Equation (3.39) is first of all translated into a common form for both methods.
In general, the flux depends on fluid properties, geometric information and soil properties, and an expression of the potential that drives the flow. The index set I is introduced containing all cells k that contribute to the potential gradient, and the vector $\mathbf{d}_k$ points from the centroid of cell k to its neighbour cell while $\mathbf{n}_\gamma$ is the normal of γ always pointing outwards of cell i. This reforms Equation (3.39) to yield

$$f_\gamma = - \underbrace{\sum_\alpha \varrho_\alpha \lambda_\alpha}_{\text{fluid coefficients}} \underbrace{A_\gamma \sum_k \mathbf{n}_\gamma^T \boldsymbol{K} \mathbf{d}_k \frac{1}{\Delta x_k}}_{\text{geometry\&soil}} \underbrace{(p_{\alpha,k} - \varrho_\alpha \mathbf{g}^T \mathbf{x}_k)}_{\text{potential}} . \tag{3.40}$$

$$= - \sum_\alpha \varrho_\alpha \lambda_\alpha \sum_k \tau_k (p_{\alpha,k} - \varrho_\alpha \mathbf{g}^T \mathbf{x}_k) . \tag{3.41}$$

In Equation (3.41), the geometry and soil properties are abbreviated by introducing the "transmissivity coefficient" τ, combining the geometry and the resistance to flow.

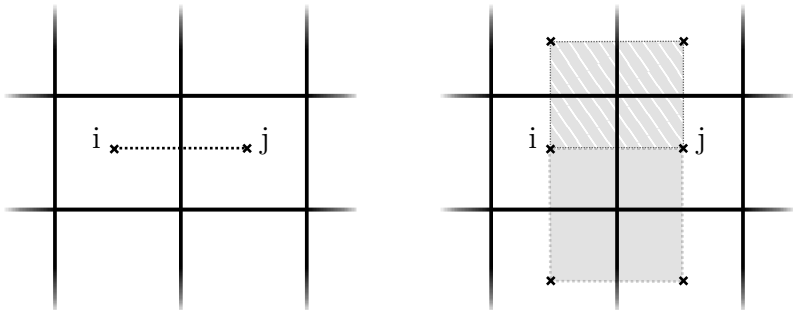

(a) Two-point flux approximation (TPFA)

(b) Multi-point flux approximation (MPFA), with both interaction regions of the "O-method".

Figure 3.3: Schematic of different flux approximations between cell i and j

The two-point flux approximation (TPFA)

This classical approach is obtained when Equation (3.41) is formed with $|I| = 2$, which means that the potential is approximated by a two-point stencil on cell i and its

neighbour j,

$$\nabla\Phi_\alpha = \frac{\Phi_{\alpha,j} - \Phi_{\alpha,i}}{\Delta x}\mathbf{d}_{ij} \ , \quad \Phi_{\alpha,k} = p_{\alpha,k} - \varrho_\alpha \mathbf{g}^T \mathbf{x}_k, \quad k \in I = \{i, j\} \tag{3.42}$$

Despite (or perhaps because) the TPFA is so straightforward, there are limits to its applicability, for example in the case of an-isotropic permeability (*Aavatsmark et al.*, 1996; *Class et al.*, 2006). Hence, TPFA-methods should best be applied if the grid is **K**-orthogonal (*Khattri and Aavatsmark*, 2008).

Yet even in the case of a homogeneous medium, a refined grid destroys the **K**-orthogonal setting and the TPFA method fails to reproduce all fluxes correctly (*Edwards* (1996), and Section 5.5).

The MPFA L-method

For an increased flux stencil, transmissibility coefficients have to be found that would approximate the gradients on the interface by multiple points, i.e. $|I| > 2$, a so-called "multi-point flux approximation" (MPFA-method). A detailed derivation can be found in (*Aavatsmark*, 2007; *Wolff*, 2013). I will briefly derive the L-method following *Aavatsmark et al.* (2010); *Wolff et al.* (2013a), as other types of MPFA methods are not used in this work. In order to keep the derivation dimension-independent, the variable n_{dim} is introduced standing for the number of dimensions considered, i.e. $n_{dim} \in [2, 3]$, and the control variable l in $\sum_{l=1}^{n_{dim}}$ allows for summing up n_{dim} quantities.
To calculate the flux through interface γ_{ij}, the interface is subdivided into $2^{(n_{dim}-1)}$ sub-interfaces $\breve{\gamma}_{ij}$. For each of these sub-interfaces $\breve{\gamma}_{ij}$, an interaction region is created that contains $|\breve{I}| = n_{dim} + 1$ cells $\breve{k}$ (Figure 3.4(a)) and n_{dim} sub-interfaces $\breve{\gamma}^\star$ connecting all cells $\breve{k}$. The name of the L-method comes from the layout of the interaction region in two dimensions, which covers three cells that are shaped like the letter "L".
The flux through each of the sub-interfaces into the accompanying cell $\breve{k}$ can be approximated by

$$f_{\breve{k},\breve{\gamma}^\star} = -\sum_\alpha \varrho_\alpha \lambda_\alpha \mathbf{n}^T_{\breve{k},\breve{\gamma}^\star} \boldsymbol{K}_{\breve{k}} \nabla\Phi_{\alpha,\breve{k}} \tag{3.43}$$

The vector $\mathbf{n}_{\breve{k},\breve{\gamma}^\star}$ is the outward pointing normal from cell $\breve{k}$ with a length equal to the volume of the corresponding sub-face $\breve{\gamma}^\star$. To ease readability, the phase index is omitted from now on until the full flux expression is found (Equation (3.51)), as only there phase

quantities re-enter the calculation procedure.
At each corner of $\breve{\gamma}^\star$, new discretisation points are introduced, denoted by a tilde in the formulas and depicted in gray in Figure 3.4(b). Together with the cell center, they span a variational triangle ($n_{dim} = 2$) or tetrahedron ($n_{dim} = 3$) in each cell (Figure 3.4(c)). The gradient in Equation (3.43) is approximated linearly using both the potential in the cell center and the newly introduced potentials on the interfaces,

$$\nabla\Phi_{\breve{k}} = \frac{1}{T_{\breve{k}}} \sum_{l=1}^{n_{dim}} \nu_{\breve{k},l}(\tilde{\Phi}_{\breve{k},l} - \Phi_{\breve{k}}) \tag{3.44}$$

The vector $\nu_{\breve{k},l}$ is a vector in cell $\breve{k}$ that is normal to the entity connecting the other points opposite of $\tilde{\mathbf{x}}_l$ that span the variational triangle (or tetrahedron) in $\breve{k}$ (Figure 3.4(c)). Its length again equals the volume of that entity and it points inwards into the variational triangle. The determinant $T_{\breve{k}}$ contains the vector product of the n_{dim} vectors that connect $\mathbf{x}_{\breve{k}}$ with $\tilde{\mathbf{x}}_l$.

Flux continuity demands that for each sub-face $\tilde{\gamma}^\star$, the flux should be equal from both sides. Exemplary, for the sub-face $\tilde{\gamma}^\star_{ij}$ equality of fluxes yields

$$-\sum_\alpha \varrho_\alpha \lambda_\alpha \mathbf{n}^T_{\breve{\gamma}^\star_{ij}} \boldsymbol{K}_i \frac{1}{T_i} \sum_{l=1}^{n_{dim}} \nu_l(\tilde{\Phi}_{i,l} - \Phi_i) = -\sum_\alpha \varrho_\alpha \lambda_\alpha \mathbf{n}^T_{\breve{\gamma}^\star_{ij}} \boldsymbol{K}_j \frac{1}{T_j} \sum_{l=1}^{n_{dim}} \nu_l(\tilde{\Phi}_{j,l} - \Phi_j) \tag{3.45}$$

$$-\mathbf{n}^T_{\breve{\gamma}^\star_{ij}} \boldsymbol{K}_i \frac{1}{T_i} \sum_{l=1}^{n_{dim}} \nu_l(\tilde{\Phi}_{i,l} - \Phi_i) = -\mathbf{n}^T_{\breve{\gamma}^\star_{ij}} \boldsymbol{K}_j \frac{1}{T_j} \sum_{l=1}^{n_{dim}} \nu_l(\tilde{\Phi}_{j,l} - \Phi_j) \tag{3.46}$$

Equation (3.45) can be reduced to (3.46) if the the phase mobility is not considered to be part of the transmissivity. This is not always feasible (*Wolff*, 2013), especially if the mobilities are derived from up-scaling and are of tensorial nature (*Wolff et al.*, 2012; *Class et al.*, 2006). The fluid coefficients need to be nevertheless included after the MPFA transmissivities are found to recover the flux.
The Equations (3.46) for all $\tilde{\gamma}^\star$ yield a system of n_{dim} equations that contain the potentials in the $\breve{k}$ cell centres, plus yet too many potentials at the introduced points on the interfaces. A linear interpolation in cell i allows to calculate the potentials that do not lie in the midpoint of an interface γ_k in the interaction region,

$$\Phi_r = \nabla\Phi_r(\tilde{\mathbf{x}}_r - \mathbf{x}_i) + \Phi_i = \frac{1}{T_i} \sum_{l=1}^{n_{dim}} \nu_{i,l}(\tilde{\mathbf{x}}_r - \mathbf{x}_i)(\tilde{\Phi}_{i,l} - \Phi_i) + \Phi_i \ . \tag{3.47}$$

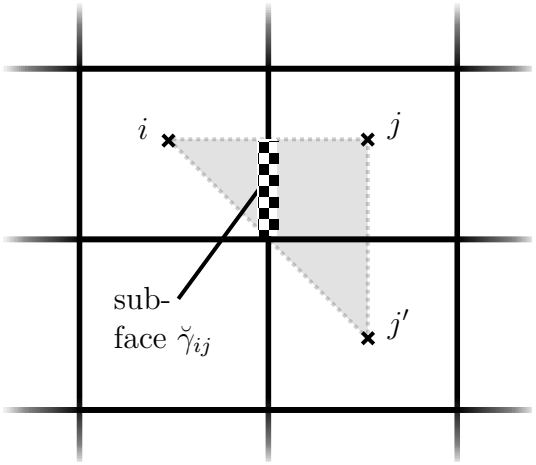

(a) Interaction region (grey) for the sub-face $\breve{\gamma}_{ij}$ between cell $\breve{k} = i$ and $\breve{k} = j$ that also includes the third cell $\breve{k} = j'$.

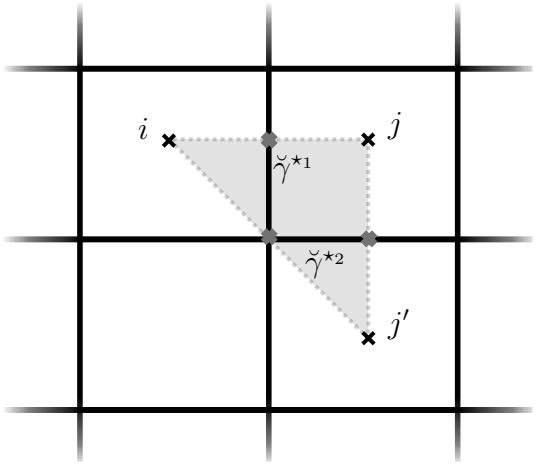

(b) Approximation of potential gradients with additional grey points on the sub-faces $\breve{\gamma}^{\star}$.

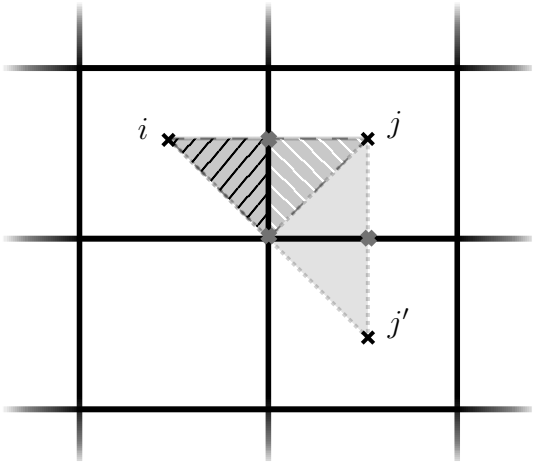

(c) Variational triangles for one sub-face $\breve{\gamma}^{\star_1}$ of the interaction region used to express the fluxes through $\breve{\gamma}_{ij}$ from both cells $\breve{k} = i, j$

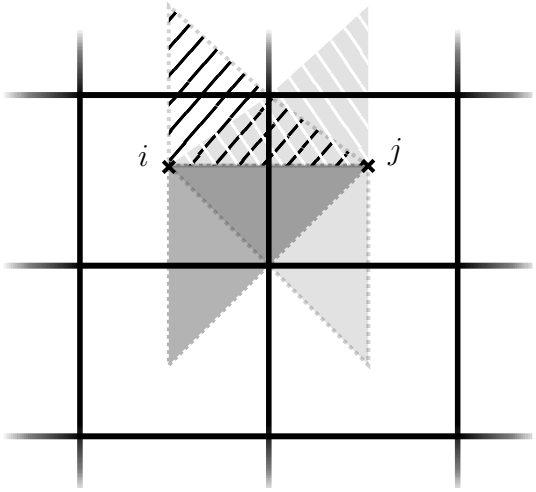

(d) Possible choices of interaction regions for the two sub-faces of face γ_{ij}.

Figure 3.4: The schematic of the MPFA L-method in two dimensions.

This allows to remove (hence index "r") one unknown in two dimensions and three unknowns in three dimensions. The flux equity of Equation (3.46) can be written in matrix form

$$\boldsymbol{A}\tilde{\mathbf{v}} = \boldsymbol{B}\mathbf{u} \tag{3.48}$$

$$\tilde{\mathbf{v}} = [\tilde{\Phi}_1, \ldots, \tilde{\Phi}_{n_{dim}}]^T, \mathbf{u} = [\Phi_1, \ldots, \Phi_{|I|}]^T \tag{3.49}$$

Likewise, the fluxes through all sub-faces in the interaction region are

$$\mathbf{f}_{\breve{\gamma}^\star} = [f_{\breve{\gamma}_1^\star}, \ldots, f_{\breve{\gamma}_{n_{dim}}^\star}]^T = \boldsymbol{C}\tilde{\mathbf{v}} + \boldsymbol{D}\mathbf{u} \tag{3.50}$$

If both equations are combined, a flux expression in the form of Equation (3.45) can be formulated that includes the information from all $\breve{k} \in |\breve{I}|$ cell midpoints in the interaction region,

$$\mathbf{f}_{\breve{\gamma}^\star} = \sum_\alpha \varrho_\alpha \lambda_\alpha \boldsymbol{T}\mathbf{u}, \text{ with } \boldsymbol{T} = \boldsymbol{C}\boldsymbol{A}^{-1}\boldsymbol{B} + \boldsymbol{D} \tag{3.51}$$

The matrix $\boldsymbol{T}$ that holds the transmissibility coefficients τ represent the MPFA interpretation of Equation (3.41) with $|\breve{I}| > 2$, which yields a first order approximation instead of zeroth order. The total flux through γ_{ij} is then expressed by all interaction regions, i.e. the summation over all $k \in \sum |\breve{I}| = |I|$.

The selection of the interaction region for sub-face $\breve{\gamma}_{ij}$ discussed here is not unique, which means that another interaction region can be build by using a different choice of cells $\breve{k}$ (Figure 3.4(d)). This is also the case for the other sub-faces contributing to face γ_{ij}. Criteria to select the most stable L-stencil are proposed in *Aavatsmark et al.* (2008); *Wolff* (2013)

Upwinding

The coefficients related to the flux terms of the discretised equations of the last sections are determined by fully upwinding (*Helmig*, 1997). The upwind direction is based on the sign of flux function (Equation (3.41)). For fluxes derived by a TPFA, it is sufficient to consider the sign of projection of the potential gradient in Equation (3.42) on the distance vector. If an MPFA is used, the necessary parts of Equation (3.51) are

considered, namely

$$sign\left(\sum_k \tau_k(p_{\alpha,k} - \varrho_\alpha \mathbf{g}^T \mathbf{x}_k)\right) . \tag{3.52}$$

If the result is positive, the coefficients are taken from cell i; they are based on the neighbour cell j otherwise. Only if the result is zero, the coefficients are centrally averaged. The phase densities in Equation (3.52) are centrally averaged because the result should be independent of the assumed upwind direction. This averaging can be interpreted as the averaged density at the flux interface.

The upwind direction for the pressure equation is determined by the preceding transport estimate that is based on the coefficients and the pressure field at the old time level $t-\Delta t$. On the new time level t, the new pressure field might indicate a reversed direction of flow, for example if the entry pressure of the neighbour cell j is exceeded. This may lead to large errors in cases where the mobility differs greatly with the upwind direction. If a zero-mobility in cell j prevents flow, large gradients in Φ_α are allowed as a solution for the next time-step without a feedback on the volume balance. Any reversion of the upwind direction on the new time level t would then allow flow because of a non-zero mobility from cell i, and too much fluid will get transported. This produces a large volume error, that gets introduced as a pressure pulse via the storage term on the following time level $t + \Delta t$. A local error in the flux is thus translated into a non-local variation in pressure, inducing a change on corresponding secondary variables in the vicinity of the error, that might introduce even more stability problems, or just increase and spread the error. To avoid this, if the upwind direction changes during a time-step from pressure to the transport step, the upwind scheme is replaced by a harmonic average, which prohibits fluxes if one phase-mobility is zero. For the simulations presented here this was only required if one of the neighbouring cells had a zero mobility.

The direction of flow is unknown during initialization of the problem. This means that the initial flow field of the initialization procedure is determined by centrally averaged coefficients.

3.3.4 CFL-factor, size of the time-step

As mentioned in Section 3.1, the explicit transport scheme has to obey the CFL-criterion. The one-dimensional Equation (3.5) can be generalized (*Coats*, 2003)

$$\Delta t = a\left(\frac{S_i}{F_i}\right), \qquad a \leq 1. \tag{3.53}$$

It relates the storage S_i to a representative flux F_i.

Limitation for the time-step for mass transport

For mass transport, the mass flux per time-step may not exceed the available storage, which equals the pore space available to fluids

$$S_i = \phi_i V_i = \sum_{\kappa} C^{\kappa} \tag{3.54}$$

The expression F_i can get rather involved if established by theoretical analysis of the nonlinear hyperbolic transport system (*Coats*, 2003). In practice, most simulation tools employ rather empirical models to control the time-step (*Aziz and Settari*, 1979). For compositional multiphase flow, the simple time-step restriction proposed in (*Helmig et al.*, 2010, 2013) is employed that considers the maximum observed outflux from or influx into cell i,

$$F_i = \max\left\{\left(\sum_{\alpha}|\mathbf{n}_{\gamma}^{T}\mathbf{v}_{\alpha,\gamma}A_{\gamma}|, \sum_{\alpha}|-\mathbf{n}_{\gamma}^{T}\mathbf{v}_{\alpha,\gamma}A_{\gamma}|\right) : \gamma \in i\right\} \tag{3.55}$$

Limitation for the time-step for energy transport

For thermal systems, a corresponding CFL criterion has to be formulated for energy transport. The criterion proposed in (*Fritz*, 2010) was found to be too restrictive, because the small temperature gradients observed in this work do not require such a dramatic reduction in the size of the time-step that are necessary if diffuse heat conduction is dominant. *Geiger et al.* (2006) proposes a criterion derived from the linearised form of

(3.7) via (2.11),

$$\hat{c}_p \frac{\partial T}{\partial t} = -\nabla \cdot (\sum_\alpha c_{p,\alpha} \varrho_\alpha \mathbf{v}_\alpha T - \bar{\lambda}_E \nabla T) + q^E \tag{3.56}$$

where $\hat{c}_p = (1-\phi)\varrho_s c_{p,s} + \phi \sum_\alpha \varrho_\alpha c_{p,\alpha} S_\alpha$ abbreviates the combined heat capacity of all fluids and the solid. This equation can be reformulated in terms of S and F of Equation (3.53) if internal sources of energy and conduction are neglected, and by dropping the mixed term $-T\nabla \cdot F$, by

$$S \frac{\partial T}{\partial t} = -F \nabla \cdot T. \tag{3.57}$$

This constrains the size of the time-step for thermal systems according to a flux function $F_i = A_i \sum_\alpha c_{p,\alpha} \varrho_\alpha \mathbf{v}_\alpha$ and a storage $S_i = V_i \hat{c}_p$. In *Geiger et al.* (2006), it is formulated in view of Equation (3.5) by means of a "heat transfer velocity" $\mathbf{v}_{th}$,

$$\mathbf{v}_{th} := \frac{\partial x}{\partial t} = \frac{\sum_\alpha c_{p,\alpha} \varrho_\alpha \mathbf{v}_\alpha}{\hat{c}_p} \tag{3.58}$$

The conduction term in Equation (3.56), however, can only merge into the form of Equation (3.57) if the temperature T can be factored out of the gradient $\nabla \cdot T$ in (3.56). This can be achieved by finding a specific interpolation of $\nabla \cdot T$ that is described in the following for one dimension.

Given a regular grid, cell i lies between its neighbour j and $\bar{j}$ (Figure 3.5). Then, the values of the gradient in temperature at both interfaces γ_j and $\gamma_{\bar{j}}$ are given by

$$\Theta_j = \mathbf{n}_{\gamma_j}^T \nabla T(\gamma_j) = \frac{T_j - T_i}{\Delta x} \tag{3.59}$$

$$\Theta_{\bar{j}} = \mathbf{n}_{\gamma_{\bar{j}}}^T \nabla T(\gamma_{\bar{j}}) = \frac{T_{\bar{j}} - T_i}{\Delta x} \tag{3.60}$$

Let $\Theta(x)$ be the interpolating function for the gradient $\nabla \cdot T$ that satisfies

$$\frac{\partial \Theta(x)}{\partial x} = \xi \Theta(x) \ , \tag{3.61}$$

for a constant value of ξ on cell i, i.e. $x \in (\gamma_j, \gamma_{\bar{j}})$. The requirement (3.61) allows to factor out the temperature T in Equation (3.56), if the value of ξ can be determined by the discrete values Θ_j and $\Theta_{\bar{j}}$ at the boundary of cell i. From (3.59) and (3.61), it follows that

$$\Theta(x) = \Theta_j e^{\xi(x-\gamma_j)} \ . \tag{3.62}$$

Inserting (3.60) for x at the position of $\gamma_{\bar{j}}$ gives

$$e^{\xi(\Delta x)} = \frac{\Theta_{\bar{j}}}{\Theta_j} \tag{3.63}$$

$$\xi = (\Delta x)^{-1} \cdot \ln \frac{\Theta_{\bar{j}}}{\Theta_j} \tag{3.64}$$

In one dimension, the heat transfer velocity is therefore bounded by

$$\mathbf{v}_{th} := \frac{\sum_\alpha c_{p,\alpha} \varrho_\alpha \mathbf{v}_\alpha + \bar{\lambda}_E \xi}{\hat{c}_p} \,, \tag{3.65}$$

which enhances the formulation for convective fluxes, Equation (3.58).

In the notation of Equation (3.53), integral measures of F_i per cell are desired. For each cell, every principal direction yields an approximate value for the constant ξ based on two opposing interfaces, given the grid is regular. The maximum ξ encountered provides an upper limit for ξ_i that enters the calculation of F_i. The largest convective flux per interface, compare Equation (3.55), is considered. Combined, this yields

$$F_i^E = \max \left\{ \sum_\alpha |\mathbf{n}_\gamma^T \mathbf{v}_{\alpha,\gamma} \varrho_\alpha c_{p,\alpha} A_\gamma| : \gamma \in i \right\} + \bar{\lambda}_E \xi_i \tag{3.66}$$

The advantage of this CFL criterion is that it only reuses quantities that have to be calculated anyway in the transport scheme, thus requiring negligible additional computational efforts. An alternative mapping of the gradients at the cells' interfaces to its center has to be found if irregular grids are used. Likewise, the method presented here implicitly assumes that the temperature gradient is always in the same direction of convection. After all, it provides a working starting point for further investigation.

An additional restriction of the size of the time-step is imposed for system that approach boiling conditions (*Fritz* (2010), p.94 ff): the size of the time-step is reduced in the case of large negative volume errors to prevent a cell from being drained artificially in the next time-step. If the time-step is reduced according to

$$a_E = a \cdot (1 + \frac{\hat{v}_i - \phi_i}{\phi_i} \cdot \Delta t^{(t-\Delta t)}), \tag{3.67}$$

the error correction can balance out the volume mismatch. This correction starts to have a significant effect on the size of the time-step if the volume balance errors are

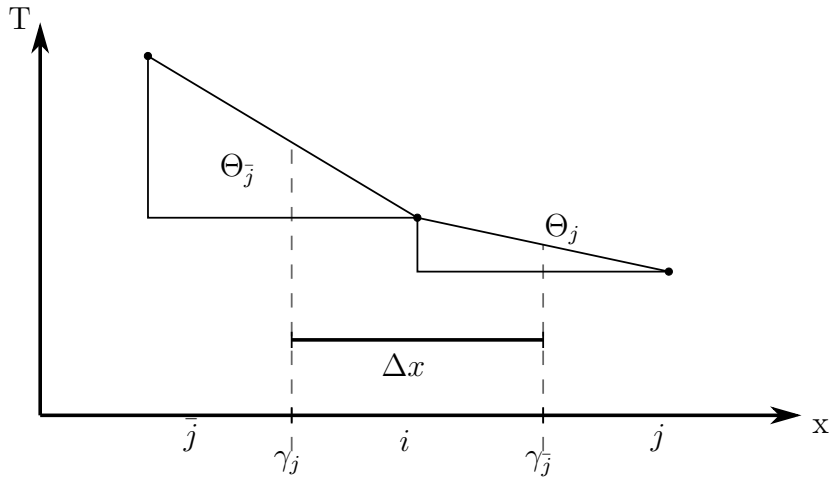

Figure 3.5: Schematic one-dimensional description of the time-step limitation for the conduction term.

exceptionally large, which is the case if a fluid boils off. If boiling is not possible, however, it provides too harsh a restriction on the time-step and is thus omitted.

3.3.5 Volume derivatives

The storage term of the pressure equation contains the combined compressibility of the fluids, $\hat{c}$. It can be determined numerically by increasing the pressure slightly and calculating the change in fluid density. If this yields a positive compressibility, which can not be possible (*Trangenstein and Bell*, 1989), the increment in pressure is inverted, and the derivative is formed by a decrease in fluid pressure.

Considering the remaining derivatives of fluid volume, *Fritz* (2010) argued that a secant method captures the non-linearities in total specific volume better than building the derivatives by a tangent. A predictor transport step based on the flow field of the last time-step estimates the increment of the conserved quantities $C^\kappa, \hat{u}$, and thereby providing the "run" of the secant. The "rise" of the specific total volume function is the difference between current fluid volume $\hat{v}^t$, Equation (3.37) exploited with the current set of state variables, and the fluid volume $\hat{v}_{\text{est}}^{t+\Delta t}$ based on a variable set including the estimate. To build the latter, the quantity of the partial derivative is altered by the amount that stems from the estimate step, while the remaining variables are kept constant.

The partial derivatives with respect to composition at constant temperature (or internal energy if non-isothermal) are thus

$$\frac{\partial \hat{v}}{\partial C^{\iota}} = \frac{\hat{v}(C^{\kappa} + \Delta C^{\iota}_{\mathrm{est}}) - \hat{v}(C^{\kappa})}{\Delta C^{\iota}_{\mathrm{est}}} \,. \tag{3.68}$$

Here, $\hat{v}(C^{\kappa})$ denotes the specific volume based on the quantities C^{κ} for all components κ, whereas the second volume $v(C^{\kappa} + \Delta C^{\iota}_{\mathrm{est}})$ of the "rise" is gained by adding the estimate $\Delta C^{\iota}_{\mathrm{est}}$ of one component $\iota \in \kappa$ to the full set C^{κ} and keeping all other concentrations constant.
The derivative with respect to internal energy is build by

$$\frac{\partial \hat{v}}{\partial \hat{u}} = \frac{\hat{v}(C^{\kappa}, \hat{u} + \Delta \hat{u}_{\mathrm{est}}) - \hat{v}(C^{\kappa}, \hat{u})}{\Delta \hat{u}_{\mathrm{est}}} \,. \tag{3.69}$$

If the estimated changes in composition are too small ($\Delta C^{\kappa} \leq 1 \cdot 10^{-8} \cdot \varrho_{\alpha}$), the numerical differentiation can fail (*Fritz*, 2010). This is avoided by regularising the increment to a minimum limit of $\Delta C^{\kappa} \leq 1 \cdot 10^{-8} \cdot \varrho_{\alpha}$ to avoid failure.

Compressibility at boiling conditions

In Section 2.1.2, the compressibility β_{α} that allows for changes of fluid density with pressure was explained. At boiling conditions, the compressibility is dominated by the fraction of substance that undergoes a phase change and the accompanied expansion of the system instead of the functional dependency of density with pressure and temperature. Such phase change is considered in the approach of *Grant and Sorey* (1979) while fully neglecting the pure phase compressibility β_{α}.

At boiling conditions ($p = p_{vap}$), a drop in pressure forces a change in fluid temperature, because the boiling mixture is bound to the vapour pressure curve. For infinitesimal changes in Temperature, changes of vapour pressure can by described by the Clausius Clapeiron equation (e.g. *Poling et al.* (2001)), which combined yields

$$\Delta p = \Delta T \frac{dp_{vap}}{dT} = \Delta T \frac{\varrho_{liq} \varrho_{g}}{\varrho_{liq} - \varrho_{g}} \frac{h_{g} - h_{liq}}{T} \tag{3.70}$$

If the temperature drops, both the solid and the rock release heat

$$\Delta Q = V \left[(1-\phi)\varrho_s c_{p,s} + \phi \sum_\alpha S_\alpha \varrho_\alpha c_{p\alpha} \right] \Delta T \tag{3.71}$$

which has to be absorbed by evaporizing some mass m of liquid,

$$\Delta Q = \Delta m (h_g - h_{liq}) \tag{3.72}$$

When in liquid state, it occupied a volume of $\Delta m/\varrho_{liq}$, and after phase change expanded to $\Delta m/\varrho_g$, which means the volume of the boiling system is increased by

$$\Delta V = \Delta m (\frac{1}{\varrho_g} - \frac{1}{\varrho_{liq}}) \tag{3.73}$$

Equations (3.70) to (3.73) combined describe the compressibility for boiling systems,

$$\beta_{boil} = \frac{1}{\phi} \left[(1-\phi)\varrho_s c_{p,s} + \phi \sum_\alpha S_\alpha \varrho_\alpha c_{p\alpha} \right] \left(\frac{\varrho_{liq} - \varrho_g}{(h_g - h_l)\varrho_{liq}\varrho_g} \right)^2 \cdot T \tag{3.74}$$

In *Grant and Sorey* (1979) the authors propose an approximation of Equation (3.74),

$$\beta_{boil} = \frac{1}{\phi} \left[(1-\phi)\varrho_s c_{p,s} + \phi \sum_\alpha S_\alpha \varrho_\alpha c_{p\alpha} \right] \cdot (1.92 * 10^{-5} (p * 10^5)^{-1.66}) * 10^{-5} \,, \tag{3.75}$$

that is reasonably valid in the pressure range considered in this work. The application of $\hat{c} = \beta_{boil}$ at boiling conditions also provides the numerical benefit of less fluctuations in pressure, thus stabilising the solution method.

3.4 Equilibrium calculations

Determining the real configuration of the fluid mixture in the case of a compositional multi-phase system depends on the choice of the primary variables. If the saturation and pressure is known, the composition can readily be determined by using equilibrium mass or mole fractions (*Class*, 2008). The choice made in this work, the total mass per unit volume, means that both phase composition (i.e. mass fractions) as well as phase distribution (i.e. saturation) is unknown. These quantities are required compute

the secondary variables, such as density or macro-scale capillary pressure. Therefore, composition and phase distribution are determined after each time-step before the secondary variables can be updated. In thermodynamics, these calculations are called "flash calculations": once a specific amount of matter is fed into a container at a certain pressure, a part of the liquid feed "flashes" into vapour. Such a phase split depends on the state of the system, yet being independent of the size of the container. Therefore, absolute quantities of the components, despite being volume-specific like the primary variable C^κ, are not relevant. Instead, relative quantities in terms of fractions are introduced:

- The feed mass fraction

$$Z^\kappa = \frac{m^\kappa}{\sum\limits_\kappa m^\kappa} = \frac{C^\kappa}{\sum\limits_\kappa C^\kappa} = \frac{\sum\limits_\alpha (S_\alpha X_\alpha^\kappa \varrho_\alpha)}{\sum\limits_\kappa \sum\limits_\alpha (S_\alpha X_\alpha^\kappa \varrho_\alpha)} \tag{3.76}$$

  relates the mass of a specific component to the total mass.

- The phase mass fraction

$$\nu_\alpha = \frac{m_\alpha}{\sum\limits_\alpha m_\alpha} = \frac{S_\alpha \varrho_\alpha}{\sum\limits_\alpha (S_\alpha \varrho_\alpha)} \tag{3.77}$$

  is a measure of mass present in a specific phase compared to the total mass in all phases. By means of the phase density, the phase mass fraction directly translates to the saturation

$$S_\alpha = \frac{\nu_\alpha / \varrho_\alpha}{\sum\limits_\alpha \left(\nu_\alpha / \varrho_\alpha\right)} \tag{3.78}$$

  Since the saturation is the quantity appearing in the governing equation, the phase mass fraction is mainly used on the road to calculate it, thus is principally appearing in Section 3.4.2.

The quantities presented in this Section can also be expressed in molar fashion, for example the feed mass fraction Z^κ can be transferred to a feed mole fraction

$$z^\kappa = \frac{Z^\kappa / M^\kappa}{\sum_\kappa Z^\kappa / M^\kappa} \,. \tag{3.79}$$

Accordingly, the phase mass fraction can be calculated from a molar based fraction $\nu_\alpha|_{\text{mole}}$ by

$$\nu_\alpha|_{\text{mass}} = \frac{\nu_\alpha|_{\text{mole}} \sum_\kappa x_\alpha^\kappa M^\kappa}{\sum_\alpha \nu_\alpha|_{\text{mole}} \sum_\kappa x_\alpha^\kappa M^\kappa} \tag{3.80}$$

This also holds for the presented methodologies of Section 3.4. The way it is presented here is based on the fact that while molar values are typically used in the thermodynamics framework of the applied EOS, the conservation equations are mass-based. The actual place where the transformation occurs is irrelevant.

3.4.1 Equilibrium ratios

Flow through natural porous media is typically slow compared to the speed of phase transitions so the fluids are locally assumed to be in equilibrium (Section 2.1.3). The composition of a component in a mixture can be related to a reference phase by Equation (2.17). As equal pressures in both states drop out, the equation can be rearranged

$$\frac{x_\alpha^\kappa}{x_r^\kappa} = \frac{\varphi_r^\kappa}{\varphi_\alpha^\kappa} := k_\alpha^\kappa \,, \tag{3.81}$$

which defines the mole equilibrium ratio. The notation $k_\alpha^\kappa|_r$ would explicitly declare the reference system. It can be formulated independently of the applied thermodynamic model (Section 2.1.3, i.e. Equation (2.29) or (2.35), or the simplifications (2.34) and (2.32)), so perfectly suited for a common framework for different fluids. In general, as are fugacities, the equilibrium ratios are dependent on the composition, so an iterative update is required (*Michelsen and Mollerup*, 2007) for consecutive solutions of composition. For the fluid mixtures applied in this work, the equilibrium ratios remain constant and allow for a direct solution for the composition (*Fritz et al.*, 2012). This assumption has to be justified by an appropriate choice of the applied material law, or EOS.

In fluid systems with an equal amount of components and phases, each component typically resides predominantly in its respective phase. It thus seems natural to use that as the reference phase, e.g. relate the water component to the water phase, and get $k_a^A = k_b^B = k_c^C = 1$ for the components A, B, C and phases a, b, c. Yet the flash calculations require a set of equilibrium constants that are all based on the same reference phase. The transformation from any reference phase r to another phase, such as water

component κ		A≙water	B≙gas		C≙oil	
reference phase r		w	w	g	w	n
water	$k_w^\kappa\big\vert_r = {}^{x_w^\kappa}/_{x_r^\kappa}$	1	1	${}^{p_g}/_{H_w^B}$	1	${}^{p_{vap}^C}/_{H_w^C}$
gas	$k_g^\kappa\Big\vert_r = {}^{x_g^\kappa}/_{x_r^\kappa}$	${}^{p_{vap}^A}/_{p_g}$	${}^{H_w^B}/_{p_g}$	1	${}^{H_w^C}/_{p_g}$	${}^{p_{vap}^C}/_{p_g}$
oil	$k_n^\kappa\vert_r = {}^{x_n^\kappa}/_{x_r^\kappa}$	${}^{p_{vap}^A}/_{H_n^A}$	${}^{H_w^B}/_{p_{vap}^B}$	${}^{p_g}/_{H_n^B}$	${}^{H_w^C}/_{H_n^C}$	1

Table 3.1: Equilibrium ratios up to a three-component three-phase system, after *Fritz et al.* (2012).

w, is possible only if the whole set of k-values are available for the old reference phase by

$$k_\alpha^\kappa\vert_w = \frac{x_\alpha^\kappa}{x_w^\kappa} = \frac{{}^{x_\alpha^\kappa}/_{x_r^\kappa}}{{}^{x_w^\kappa}/_{x_r^\kappa}} = \frac{k_\alpha^\kappa\vert_r}{k_w^\kappa\vert_r} \,. \tag{3.82}$$

Table 3.1 lists the equilibrium ratios according to Section 2.1.3 for three phases in the lower rows. The columns for the three components are split into two parts, each showing the equilibrium ratios based on a differently chosen reference phase. Transformation into one common reference, as an example shown for $k_w^B\vert_g \rightsquigarrow k_w^B\vert_w$ from Table 3.1, is possible by Equation (3.82),

$$k_w^B\Big\vert_w = \frac{k_w^B\Big\vert_w}{k_g^B\Big\vert_g} = \frac{1}{{}^{p_g}/_{H_w^B}} = \frac{H_w^B}{p_g} \,. \tag{3.83}$$

The same consideration holds for mass-related quantities.

3.4.2 Isothermal isobaric flash calculation

Flash calculations "partition the total amount of a substance into the different fluid [phases]" (*Pinder and Celia*, 2006). The equilibrium ratios from the previous Section 3.4.1 and the fact that all fractions have to sum up to unity in each phase yields an equation for each phase,

$$\begin{aligned} \sum_\kappa x_\alpha^\kappa &= 1 \\ \sum_\kappa k_\alpha^\kappa x_{ref}^\kappa &= 1 \quad \forall\alpha \,. \end{aligned} \tag{3.84}$$

Its solution for given state variables pressure and temperature provide the composition of a reference system in which all components reside in equilibrium. This reference configuration is then used to back-calculate the potential composition at the solubility limit in all phases that could potentially be present. After being transformed to mass fractions via (2.2), these hypothetical values are then compared with the actual amount of each component that is present in the control volume. The summed mass over all phases of each component has to equal the actual feed mass fraction Z^κ (3.76),

$$\sum_\alpha \nu_\alpha X_\alpha^\kappa = Z^\kappa \quad \forall \kappa \ . \tag{3.85}$$

Assembled for each component this yields a system of equations that can be solved for the phase mass fractions ν_α. The result is then tested for validity: if the amount of a component in the total mixture is too small to surpass the solubility limits in the other phases, it can not form its own phase, and the respective phase mass fraction becomes negative. The phase is in this case removed from the material balance (3.85) and its solution repeated until only non-negative values of ν_α are found.

The Rachford-Rice equation

Rachford Jr and Rice (1952) realized that one phase, preferably the reference phase r, can be eliminated from the system of equations. For the total number of n phases of the multi-phase system denoted by α, the subset β contains $n-1$ phases because the reference phase r is eliminated. Equation (3.85) is transformed to

$$\left(1 - \sum_\beta \nu_\beta\right) X_r^\kappa + \sum_\beta \nu_\beta X_\beta^\kappa = Z^\kappa \quad \forall \kappa \ , \tag{3.86}$$

and insertion of the equilibrium ratios (3.81) and elegant reordering yields

$$X_r^\kappa (1 + \sum_\beta \nu_\beta (K_\beta^\kappa - 1)) = Z^\kappa \quad \forall \kappa \ . \tag{3.87}$$

The mass balance requires

$$\sum_\kappa (X_\beta^\kappa - X_r^\kappa) = 0 \ , \tag{3.88}$$

and substitution therein of X_β^κ with (3.81) and X_r^κ with (3.87) fully eliminates quantities of the reference phase r to get

$$\sum_\kappa \frac{Z^\kappa(K_\beta^\kappa - 1)}{1 + \sum_\beta \nu_\beta (K_\beta^\kappa - 1)} = 0 \quad \forall \beta \ , \tag{3.89}$$

the so-called RACHFORD-RICE equation.

Once the phase mass fractions are found, the composition of the phases is calculated by the combination of (3.87) (3.81)

$$X_\beta^\kappa = \frac{Z^\kappa K_\beta^\kappa}{1 + \sum_\beta \nu_\beta (K_\beta^\kappa - 1)} \ . \tag{3.90}$$

The (p, T)-flash for two phases

In a two-phase system, there remains only one phase β which means that only a single RACHFORD-RICE equation needs to be solved. Once the phase mass fraction is found and checked for validity ($0 \leq \nu_\beta \leq 1$), the composition in the reference phase can be determined. For the case of only two components A and B, Equation (3.87) simplifies to

$$X_r^A = \frac{1 - K_r^B}{K_r^A - K_r^B} \ , \tag{3.91}$$

which can then be used to calculate X_β^A with Equation (3.81). This already provides the full set of all four mass fractions, and the composition is determined.

A two-phase three-component mixture evolves if one phase is not present in a three-phase thee-component system because its component is fully dissolved in the other phases. The vanishing phase can very well be the reference phase, so removing it from Equation (3.85) to proceed would result in a detour because it does not directly yield the properties of the phases of interest. Derivation of a modified RACHFORD-RICE Equation (*Fritz*, 2010; *Michelsen and Mollerup*, 2007) by removing a phase a other than the reference phase yields

$$\sum_\kappa \frac{Z^\kappa(K_a^\kappa - K_b^\kappa)}{1 + \nu_b (K_a^\kappa - K_b^\kappa)} = 0. \tag{3.92}$$

For three components $\kappa = A, B, C$ and phases a, b, Equation (3.92) has the form of an quadratic equation

$$c_1 \nu_b^2 + c_2 \nu_b + c_3 = 0 \tag{3.93}$$

with the coefficients

$$\begin{aligned}
c_1 =& \left(K_b^A - K_a^A\right)\left(K_b^B - K_a^B\right)\left(K_b^C - K_a^C\right) \\
c_2 =& \quad Z^A \left(K_b^A - K_a^A\right)\left(\left(K_b^B - K_a^B\right) K_a^C + \left(K_g^C - K_a^C\right) K_a^B\right) \\
&+ Z^B \left(K_b^B - K_a^B\right)\left(\left(K_b^A - K_a^A\right) K_a^C + \left(K_b^C - K_a^C\right) K_a^A\right) \\
&+ Z^C \left(K_b^C - K_a^C\right)\left(\left(K_b^A - K_a^A\right) K_a^B + \left(K_b^B - K_a^B\right) K_a^A\right) \\
c_3 =& Z^A \left(K_b^A - K_a^A\right) K_a^B K_a^C + Z^B \left(K_b^B - K_a^B\right) K_a^A K_a^C + Z^C \left(K_b^C - K_a^C\right) K_a^A K_a^B \ .
\end{aligned}$$

In case these calculations are performed with molar-based quantities, the phase mass fraction is transformed via (3.80) and the mole fractions via (2.2).

3.4.3 Isoenergetic isobaric flash calculation

Iso-energetic isobaric flash calculations seek for the composition, phase distribution and temperature at a given pressure, feed fraction and energy. It can be solved by a nested iteration, as proposed by *Fritz et al.* (2012) following *Agarwal et al.* (1991): an inner loop with an isothermal isobaric flash (last Section 3.4.2) at an intermediate temperature is nested in an outer loop calculating a temperature that matches the specified energy. For the outer loop, an objective function is defined that relates the internal energy u_m at iteration step m with the specified internal energy from after the transport solution,

$$g_{E,m} = u_m - u_{given} = \left((\sum_\kappa C^\kappa) \sum_\alpha u_\alpha \nu_\alpha + (1-\phi)\varrho_s c_s T_m \right) - u_{given} \tag{3.94}$$

To avoid computing costly derivatives of thermodynamic functions, a secant method is applied to update the temperature and minimise the function (3.94),

$$T_{m+1} = T_m - g_{E,m} \frac{T_m - T_{m-1}}{g_{E,m} - g_{E,m-1}} \tag{3.95}$$

Fritz et al. (2012) proposes to use the boiling temperature of the dominant component of the mixture $T_{m-1} = T_{boil}$ and the temperature of the last time-step $T_m = T^{t-\Delta t}$ for

the initialization of the iteration. If the fluid-system remains far away from the boiling temperature, iteration can also be started with an arbitrary initialization point such as $T_{m-1} = T^{t-\Delta t} - 10°C$, because the system properties at as high temperatures as T_{boil} might be unavailable. One way or the other, the according internal energies u_{m-1}, u_m are determined by a p-t-flash at those temperatures. The newly found temperature enters the regular p-t-flash, which yields the necessary quantities $\varrho_\alpha, \nu_\alpha, S_\alpha$ and hence also the new capillary pressure p_c to update the internal energy and determine the new residual g_E. Iteration is stopped as soon as a the fraction $\frac{g_E}{u_{given}}$ lies below a given tolerance.

The procedure converges if the mixture contains an equal number of components as possible phases (*Agarwal et al.*, 1991), which poses a problem if the dominant phase starts boiling. Then, water can be dominant in both liquid and gaseous state, and its phase distribution is independent from the temperature that is varied in the outer loop, as it remains at the boiling temperature. In this case, however, the phase mass fraction is a linear function of the internal energy, so the phase split can be directly determined by means of a lever rule,

$$\nu_{liq} = \frac{g_{E,gas}}{g_{E,gas} - g_{E,liq}} \; . \tag{3.96}$$

The deviation from a pure liquid state $g_{E,liq}$ is gained via the artificial formulation of a state (through a p-t-flash at $Tboil$) where the whole feed is assigned to the liquid phase $\nu_{liq} = 1$,

$$u^*_{liq} = (\sum_\kappa C^\kappa) u_{liq} \tag{3.97}$$

with $g_{E,gas}$ being found accordingly. Again, an iteration becomes necessary if the capillary pressure that is found through S_α after determining ν_α (Equation (3.78)) alters the pressure that is not used as the primary variable, which changes either $g_{E,liq}$ or $g_{E,gas}$.

The choice to prefer the lever rule over the temperature- iteration has to be done at the very beginning of the flash calculations. This also means that the reference states u^*_{liq} and u^*_{liq}, as well as $T_{boil,water}$ and all secondary variables at this state are known before entering the iteration. If $g_{E,gas} < 0$, the system has to be in fully gaseous state, and $g_{E,gas}, T_boil$ can serve as lower boundaries in the outer iteration loop. In the case of $g_{E,liq} > 0$, there is no gas present, which provides an upper boundary for temperature and residual in the loop. The boundaries prevent failure of the secant method over discontinuities. The lever rule is applied only if $g_{E,gas} > 0$ and simultaneously $g_{E,liq} < 0$, which means $u^*_{liq} < u_{given} < u^*_{gas}$.

3.4.4 Implementation of the flash calculations

All flash routines that are applied in this work are summarized in the Figures 3.6, following the implementation sequence implemented in DuMu$^{\text{x}}$. In the top row (Sub-figures 3.6(a) and 3.6(b)), the two types of (p, T)-flash are depicted for two and three phases. The flash routine for non-isothermal systems is depicted in the lower row (Sub-figure 3.6(c)). Each calculation step yields the encircled quantities, while dark gray boxes indicate the application of a full flash routine as depicted in the other sub-figure. The (p, T)-flash routine that is called by the non-isothermal flash does not iterate for capillary pressure, as this iteration is included in the outer iteration for temperature for efficiency reasons. Iteration is marked by the index m, and the "update" procedure on the left side of each routine increases this index by one before entering the next iterative loop.

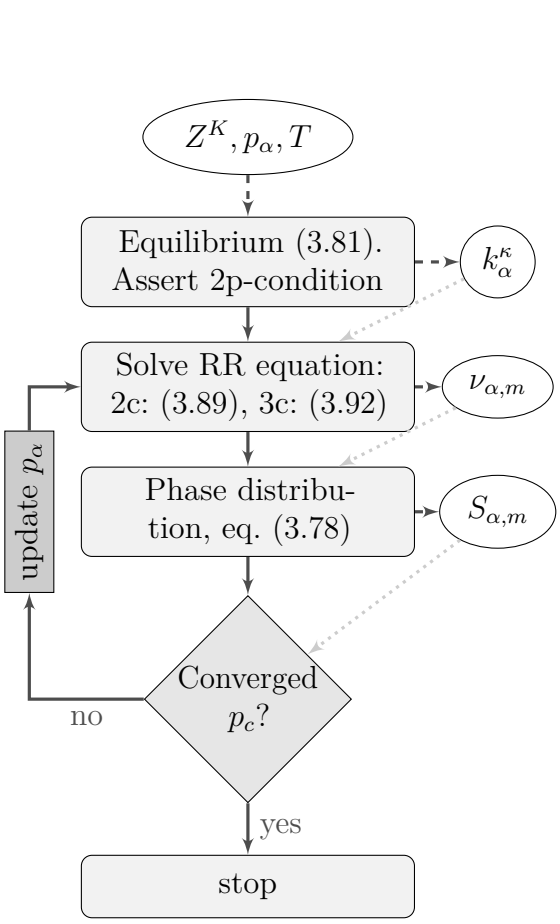

(a) 2p flash routine

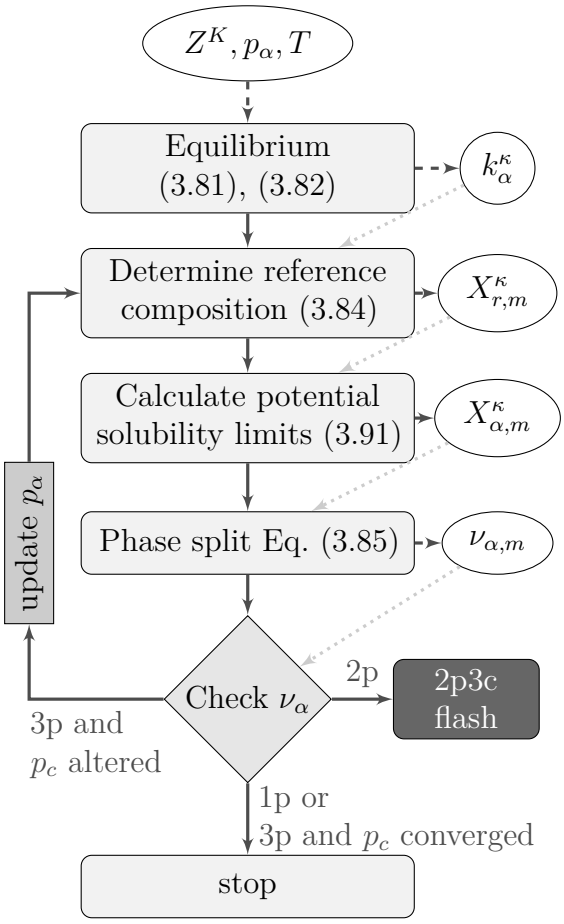

(b) 3p flash routine

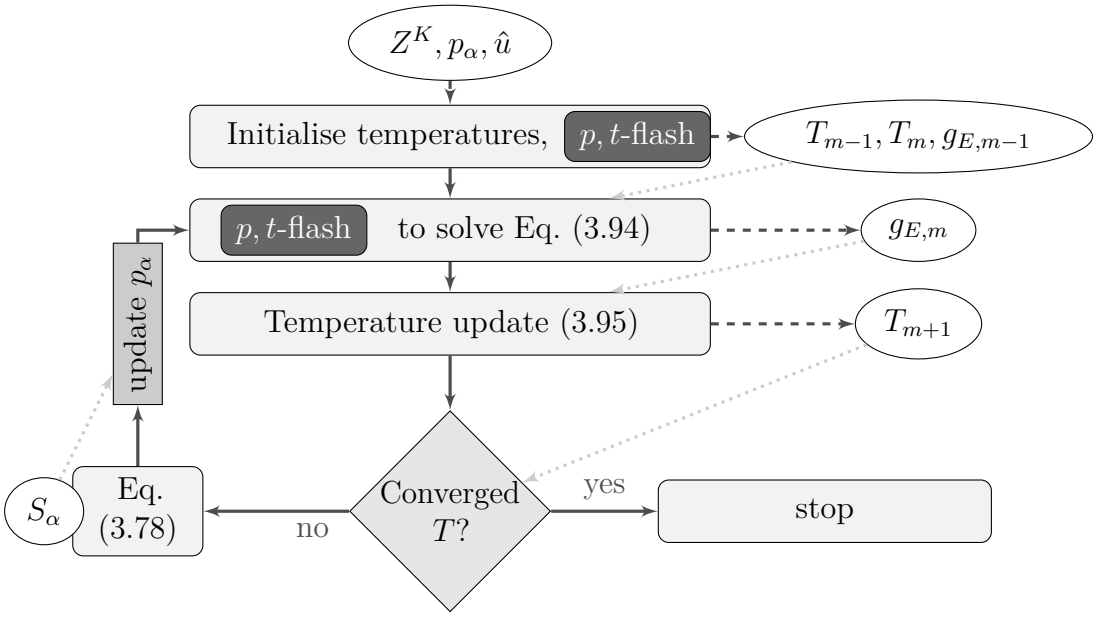

(c) NI flash for non-boiling fluids

Figure 3.6: Scematics of Flash calculation: “p” abbreviates phase, “c” abbreviates component

3.5 Numerical Examples

The modelling approach for multi-component multi-phase flow presented here was applied in the work of *Fritz et al.* (2012), and the non-isothermal model was validated with experiments and the numerical model HYDROTHERM in (*Fritz*, 2010). This work extends the model by also considering capillary effects which increase the coupling of the equations. The applicability is shown in the following briefly by comparison with appropriate fully implicit models implemented in DuMu^{x}.

3.5.1 One-dimensional injection with capillary pressure

Water is injected into a homogeneous porous medium that is initially fully saturated by the pseudo-component air. The domain is 300 m long and is discretised with a grid resolution of 100, 200, 400 and 600 cells. On the right side of the domain, there is a DIRICHLET boundary condition of $2.5 \cdot 10^5$ Pa and $S_n = 1$, and a flow of $0.5\,{}^{\mathrm{kg}}/_{(\mathrm{s\,m^2})}$ water is imposed on the left side, while gas can escape freely. Soil properties and numerical settings are summarized in Table 3.2. A fully implicit implementation (where diffusion and dispersion are switched off for comparison) is compared with the sequential solution approach of this work.

The fluid system air-water was selected as a numerically challenging example of a very compressible system at moderate pressures. Likewise, the parameters of the $p_c(S)$–relationship were chosen to produce capillary effects large enough to take the sequential solution scheme to its limits, as no iteration is performed. It is noted that in one dimension, the flux restriction discussed in Section 3.3.3 has to be omitted and the scaling of the volume integral in Equation (3.30) equals $1/2$.

If the phase pressure of the compressible phase p_n is chosen as the primary variable, the result of the front after 20000 s shows a good agreement with the fully implicit

Table 3.2: One-dimensional injection of water into a gas-filled porous medium.

Porosity	Permeability	BC-Parameter p_d	BC-Parameter λ	CFL factor a	Error factor a_e	Error bound $\underline{e}$	Bound limit $\overline{e}$
0.2	$1 \cdot 10^{-9}\mathrm{m}^2$	4000 Pa	2	0.6	0.7	0.002	0.5

scheme (Figure 3.7(a)). The fully implicit solution shows more numerical diffusion, but the solution converges (Figures 3.7(c), 3.7(d)). If the comparatively in-compressible phase is chosen as the pressure primary variable, the simulation can only be completed by reducing the CFL factor to 0.2 and the error factor to 0.35, to smooth the error correction. The spikes in the pressure field can clearly be seen in Figure 3.7(b) at approximately 55 m from the injection, near the saturation front.

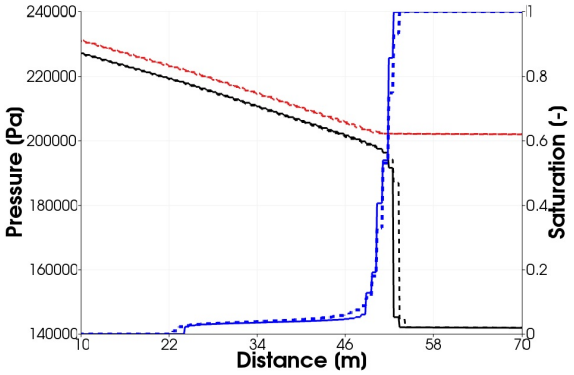

(a) Model comparison: phase pressures and saturation on finest grid (600 cells), the fully implicit model is dashed.

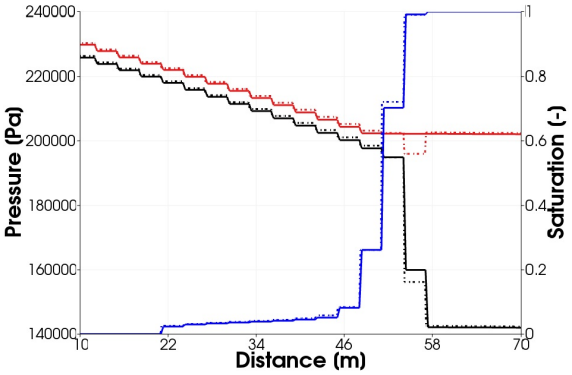

(b) Phase pressures and saturation on coarsest grid for different pressure primary variables, p_w as primary variable shown dotted.

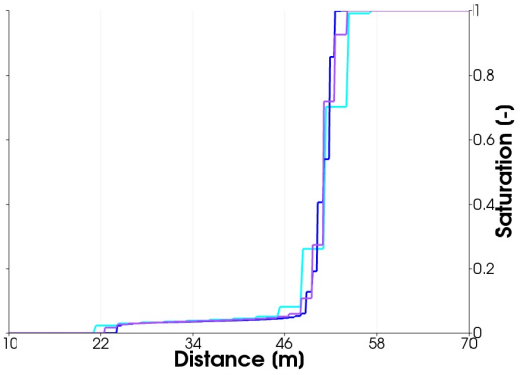

(c) Grid convergence (100-400 cells) of the saturation profile: decoupled solution.

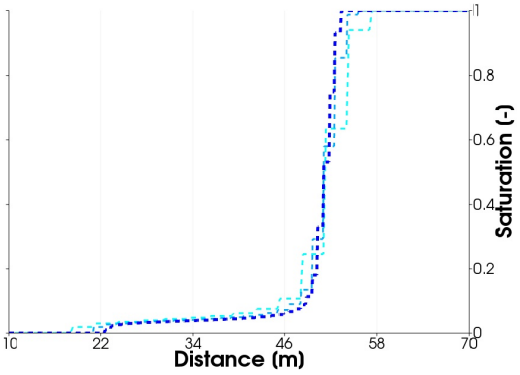

(d) Grid convergence (100-400 cells) of the saturation profile: fully implicit solution.

Figure 3.7: Water phase pressure p_w (black), gas pressure p_n (red) and saturation S_n (blue) over the distance from injection for the one-dimensional infiltration example.

3.5.2 Three-phase three-component flow with capillary pressure

A two-dimensional numerical study undertaken in *Class* (2001) serves as the basis for a comparison of the sequential approach for three-phase three-component systems with

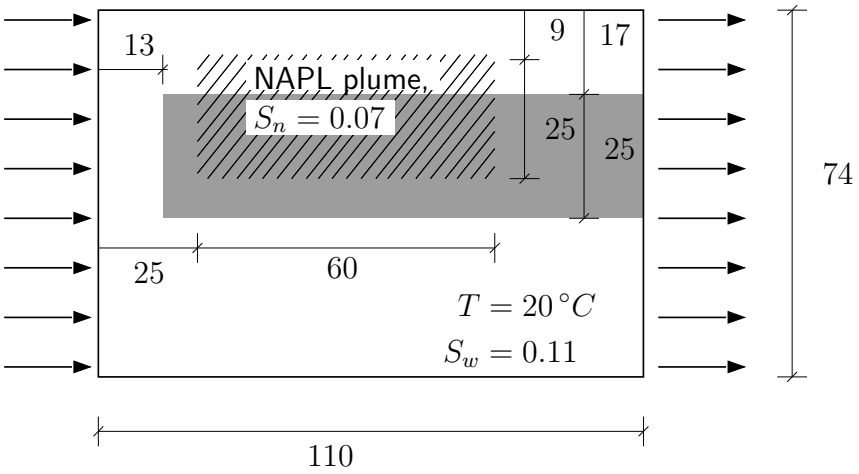

Figure 3.8: Setup of the contamination example, adapted from (*Fritz*, 2010)

a fully implicit approach. $0.3435\,\mathrm{mol/s}$ of pure air is injected from the left side into a domain of $1.1\,\mathrm{m} \times 0.74\,\mathrm{m}$, that is filled with a coarse sand ($K = 9 \cdot 10^{-10}\,\mathrm{m}^2$) surrounding a block heterogeneity ($K = 6 \cdot 10^{-12}\,\mathrm{m}^2$), see Figure 3.8. The top and bottom are closed, and a DIRICHLET boundary condition with atmospheric pressure (101300 Pa) is imposed on the right side. The domain is further filled with water at $S_w = 0.11$ and a NAPL (Non-Aqueous Phase Liquid, in this case mesitylene) contamination is located in the middle of the domain.

In the original setup, all phases but the gas phase reside below or at residual saturation, so capillary pressure does not play a role. To see some effects, the residual saturation $S_{n,res}$ was lowered in the coarse sand from 0.7 to 0.4, which draws NAPL into the fine sand lens. The numerical parameters to run the simulation are listed in Table 3.3.
Figure 3.9(a) and 3.9(b) show the NAPL and the water saturation after 7 hours of injection. Roughly a third of the NAPL plume was removed by evaporation to the air flowing by, and residual water evaporated near the injection zone. A linear plot over the white line is depicted in Figure 3.9(c), showing very good agreement of the mole fraction of mesitylene in the gas phase and the non-wetting saturation profile. The fully implicit model is slightly more diffusive, probably due to numerical diffusion. The same agreement is observed if other compositional variables are compared.

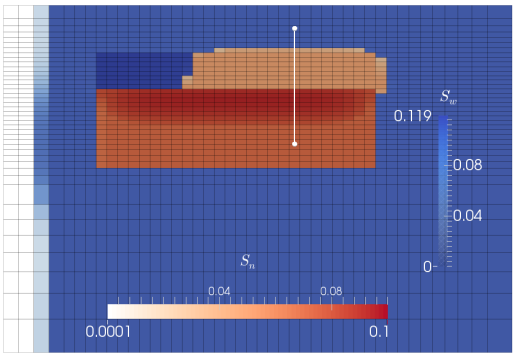

(a) Water saturation (blue) and Napl saturation (red) after 7 hours simulated sequentially.

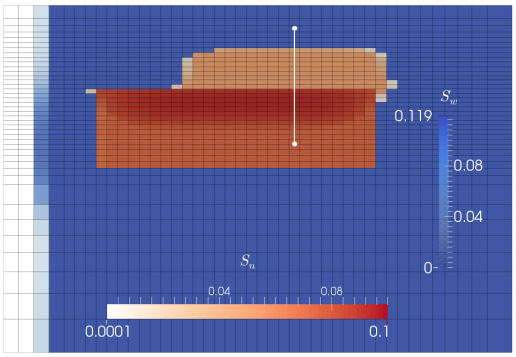

(b) Water saturation (blue) and NAPL saturation (red) after 7 hours simulated fully implicit.

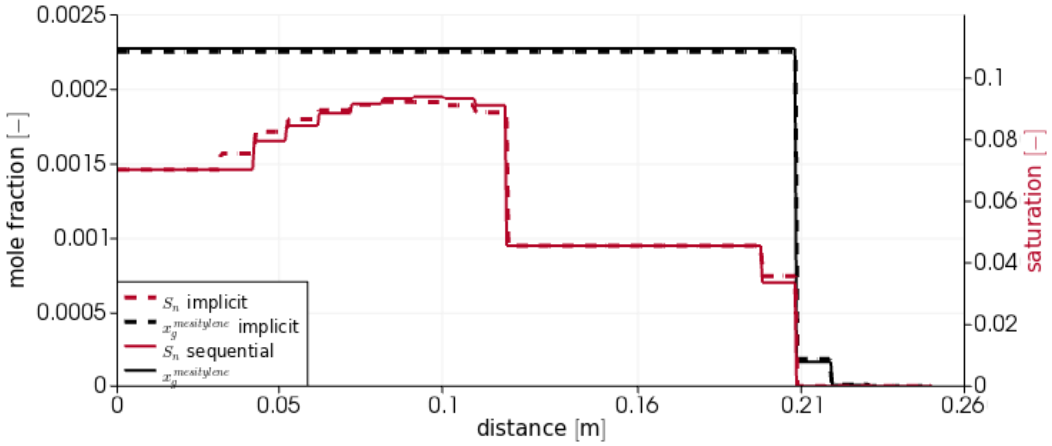

(c) Line plot of the saturation S_n (red) and mole fraction $x_g^{mesithylen}$ (black) over the distance (upwards). Fully implicit is dashed, sequential drawn with a straight line.

Figure 3.9: Three-phase three-component problem simulated sequentially and with a fully implicit model.

Table 3.3: Numerical settings for the three-phase example.

VG-Parameter			CFL	Error	Lower error	Bound
n	α_{coarse}	α_{fine}	factor a	factor a_e	bound $\underline{e}$	limit $\overline{e}$
4	0.0015	0.0005	1.	0.5	0.002	0.3

4 The multi-physics framework

In many subsurface applications, far-field effects such as pressure build-up or background flow occur under relatively simple, since fully water-saturated conditions, compared to a small region where much more complex physics prevail, for example around the injection well or the location of a contaminant spill. As can be seen in Chapter 3, huge efforts are undertaken to capture the compositional multi-phase effects of the compressible system in the pressure equation. Methods developed to describe complicated systems might be an artificial source of errors if the system is simple, such as almost incompressible single-phase flow of water: even with traces of another dissolved substance, the density of water hardly changes with composition. Inaccuracies in the increment to get the secant (Section 3.3.5) may introduce more spurious troubles than positive benefits. Under these circumstances, an inclusion of the gradients of such changes in volume (Equation (3.30)) is even more questionable.
At the least, some of those efforts exhibit excess computational work: the changes in fluid volume of a single-phase cell, for example filled with water, can be approximated by $\frac{\partial \hat{v}_\alpha}{\partial C^\kappa} = \frac{1}{\varrho_\alpha}$, so Equation (3.31) simplifies for a single-phase system to

$$V_i c_{p,w} \frac{p^t_{\alpha,i} - p^{t-\Delta t}_{\alpha,i}}{\Delta t} + \sum_{\gamma_{ij}} A_{\gamma_{ij}} \mathbf{n}^T_{\gamma_{ij}} \mathbf{K} \lambda_\alpha \mathbf{d}_{ij} \left(\frac{p^t_{\alpha,j} - p^t_{\alpha,i}}{\Delta x} - \varrho_\alpha \mathbf{g}^T \mathbf{d}_{ij} \right) = V_i \frac{\sum_\kappa q^\kappa_i}{\varrho_\alpha} + V_i \alpha_r \frac{v_\alpha - \phi}{\Delta t}. \quad (4.1)$$

In comparison to Equation (3.31), the potential to save efforts and reduce the errors described above is clearly visible.

In addition, no flash calculation has to be performed in such simple areas to find the phase distribution: the phase-state is already known to be single phase. With that knowledge,

the mass fractions can be directly assigned by means of the total concentration without the need of equilibrium calculations.

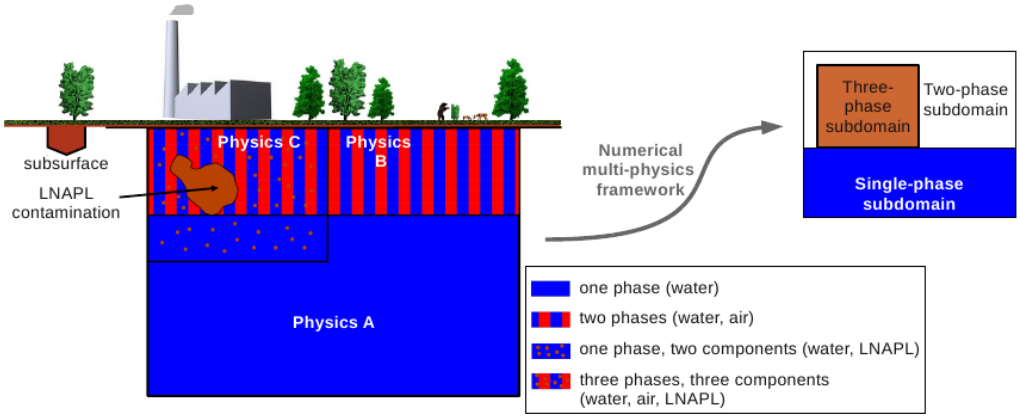

Figure 4.1: The multi-physics concept for the case of a groundwater contamination scenario, applying different numerical models according to the underlying physical processes.

The aim of this chapter is to introduce the so-called multi-physics framework that applies different numerical models locally to solve the overall system in an efficient manner and by applying the most appropriate numerical model available (Figure 4.1). The multi-physics coupling becomes manageable in this case because in the sequential solution procedure, the mathematical structure and primary variables remain similar for all levels of complexity.

4.1 The definition of sub-domains

To use different numerical model abstractions in one simulation, the global domain of interest needs to be fragmented into regions of differing physical complexity. Once these regions are identified, the appropriate and least complex numerical model can be applied locally. The global domain is thus subdivided into sub-domains that directly relate to the level of model complexity (Figure 4.1 towards the upper right). The most complex sub-domain has to cover not only cells of this complexity, but also extends a little bit further to capture transient problems. Fortunately, the *CFL* condition of the sequential solution scheme requires that fronts can not traverse more than one cell within one time-step. Therefore, a sub-domain spanning the region of highest complexity plus a "safety zone" of one cell does capture the whole complex extent for the duration of a

time-step. After each time-step, naturally, the sub-domain has to be adapted (Figure 4.2). Such adaptation can readily be done because the secondary variables have to be updated anyhow. As soon as the sub-domains are defined, the appropriate matrix entries

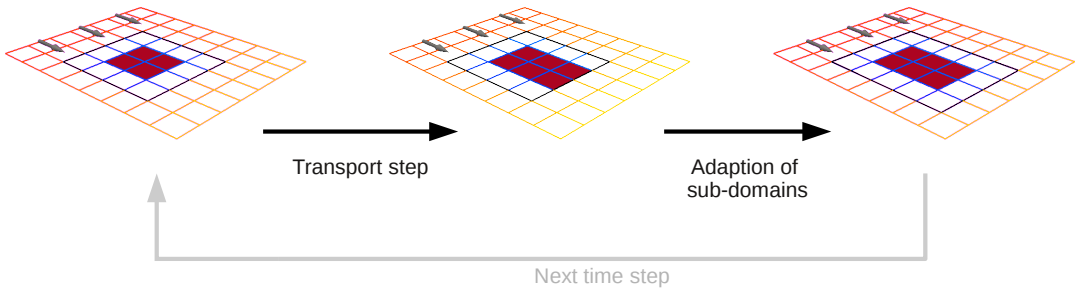

Figure 4.2: Adaptation of the complex sub-domain (blue) if the red plume spreads.

are assembled accordingly to solve the global flow field, and the correct flash calculation procedure is selected after the transport step.

The number of different sub-domains coincides with the number of different models that are applied. Under isothermal conditions, a compositional single-phase and a compositional two-phase sub-domain is sufficient to model *2p2c* systems. The obvious criteria to identify the cells in single-phase condition is the saturation. For non-isothermal (NI) flow, an additional NI–sub-domain contains all cells where the non-isothermal effects are considered important. *Fritz* (2010) proposed to use the temperature as the criterion for the NI–sub-domain: cells are assigned whose temperature had already altered more then a given temperature threshold ΔT_{thresh} compared to their initial state.

4.2 Multi-physics for non-isothermal systems

Under non-isothermal conditions, the fluid volume can change drastically in single-phase regions as well. Henc, the volume derivatives and their gradients cannot be neglected as

was done in Equation (4.1). The pressure equation can nevertheless be simplified to

$$
\begin{aligned}
&V_i c_{p,\alpha} \frac{p^t_{\alpha,i} - p^{t-\Delta t}_{\alpha,i}}{\Delta t} \\
&+ \sum_{\gamma_{ij}} A_{\gamma_{ij}} \mathbf{n}^T_{\gamma_{ij}} \left[\mathbf{K} \lambda_\alpha \mathbf{d}_{ij} \left(\frac{p^t_{\alpha,j} - p^t_{\alpha,i}}{\Delta x} - \varrho_\alpha \mathbf{g}^T \mathbf{d}_{ij} \right) (1 + \varrho_\alpha h_\alpha \frac{\partial v_\alpha}{\partial u_\alpha}) + \mathbf{d}_{ij} \bar{\lambda}_E \frac{T_j - T_i}{\Delta x} \frac{\partial v_\alpha}{\partial u_\alpha} \right] \\
&- \sum_{\gamma_{ij}} V_i \frac{A_{\gamma_{ij}}}{U_i} \mathbf{d}^T_{ij} \left[\mathbf{K} \lambda_\alpha h_\alpha \mathbf{d}_{ij} \left(\frac{p^t_{\alpha,j} - p^t_{\alpha,i}}{\Delta x} - \varrho_\alpha \mathbf{g}^T \mathbf{d}_{ij} \right) + \mathbf{d}_{ij} \bar{\lambda}_E \frac{T_j - T_i}{\Delta x} \frac{\partial v_\alpha}{\partial u_\alpha} \right] \frac{\frac{\partial v_{\alpha,j}}{\partial u_\alpha} - \frac{\partial v_{\alpha,i}}{\partial u_\alpha}}{\Delta x} \\
&\qquad = V_i \frac{\sum_\kappa q^\kappa_i}{\varrho_\alpha} + V_i \alpha_r \frac{v_\alpha - \phi}{\Delta t}. \quad (4.2)
\end{aligned}
$$

In principle, the temperature in simulations with the non-isothermal model is the result of the iterative u, p-flash (Section 3.4.3). A linear approximation of the temperature is sufficient if the system is single-phase and far away from boiling conditions,

$$T = T_{\text{init}} + \frac{1}{\hat{c}_v} \left(\hat{u} - \hat{u}(T_{\text{init}}) \right) , \quad (4.3)$$

$$\hat{c}_v = (1 - \phi) \varrho_s c_s + \phi \varrho_\alpha c_{v,\alpha} \quad (4.4)$$

Outside the NI–sub-domain, Equation (4.3) provides a temperature that is directly used in the p, T-flash to obtain the secondary variables. This linear approximation can also provide an approximation for the estimated change in temperature, which allows a direct calculation of volume derivatives in Equation (4.2) by means of an additional p, T-flash with $T + (\Delta T)_{\text{est}}$.

4.3 Multi-physics summary

For each cell i, the appropriate and least complex pressure equation is solved (see Table 4.1). If volume derivatives are required for this cell, the transport estimate is performed, else it is omitted. The regular transport step is unaffected by the multi-physics framework because all transported quantities (or their derived quantities in the case of the temperature) are required for the definition of the sub-domains; And the transport is computationally too cheap due to its explicit nature to provide enough efficiency potential. After the transport, the simplest possible flash calculations are performed, avoiding costly detours. Each cell is then assigned to the sub-domain that

Table 4.1: Multiphysics summary.

sub-domain	P. Equation	Volume derivatives	Flash
1pNc	(4.1)	no	no
1pNc-NI	(4.2)	$\partial v_w/\partial u_w$ via secant based on (4.3)	u, p-flash
2pNc	(3.31)	all but $\partial \hat{v}/\partial \hat{u}$	p, t-flash, T via (4.3)
2pNc-NI	(3.21)	all	u, p-flash
3pNc	(3.31)	all but $\partial \hat{v}/\partial \hat{u}$	p, t-flash for $3p$

coincides with the updated fluid state, the fluid configuration and the phase distribution after the transport step.

4.4 Numerical example for the multi-physics approach

To show the potential and practical applicability of the multi-physics approach, a benchmark example of geological storage of CO_2 was selected. The benchmark description can be found in (*Class et al.*, 2009), the model domain is shown in Figure 4.3(a). 15 kg/s of supercritical CO_2 (Figure 2.1) is injected for 25 years, and simulation ends after a total of 50 years using the numerical parameters listed in Table 4.2.

During the injection phase, high flow velocities yield a relatively stable time-step size of 3-4 days, injection stops after approximately 2650 time-steps. In the post-injection phase, the pressure gradient ceases, the fluxes become smaller and the size of the time-steps increases. The flux is then driven by gravitational and capillary forces, that are both strongly coupled phenomena: the weak point of the decoupled solution scheme. As the size of the time-steps grows, so does the volume error because the changes in density increase over larger time periods. Then, pressure pulses from the error term ϵ are the main causes for a reduction in time-step size, which again magnifies the term itself: exceptionally large time-steps are thus typically followed by a series of small time-steps where the method tries to balance out the errors made in that large time-step. To get a more stable behaviour, the maximum size of the time-step was restricted to $3 \cdot 10^6$s (35 days), which ensures that the post-injection phase is simulated with at least 260 time-steps. A method that gradually "ramps up" the size of the time-step, and by this avoiding excessive fluctuations, might be a promising solution.

Table 4.2: Numerical parameters for the Johansen benchmark

CFLfactor a	Error factor a_e	Lower error bound $\underline{e}$	Bound limit $\overline{e}$
0.7	0.4	$1 \cdot 10^{-2}$	0.5

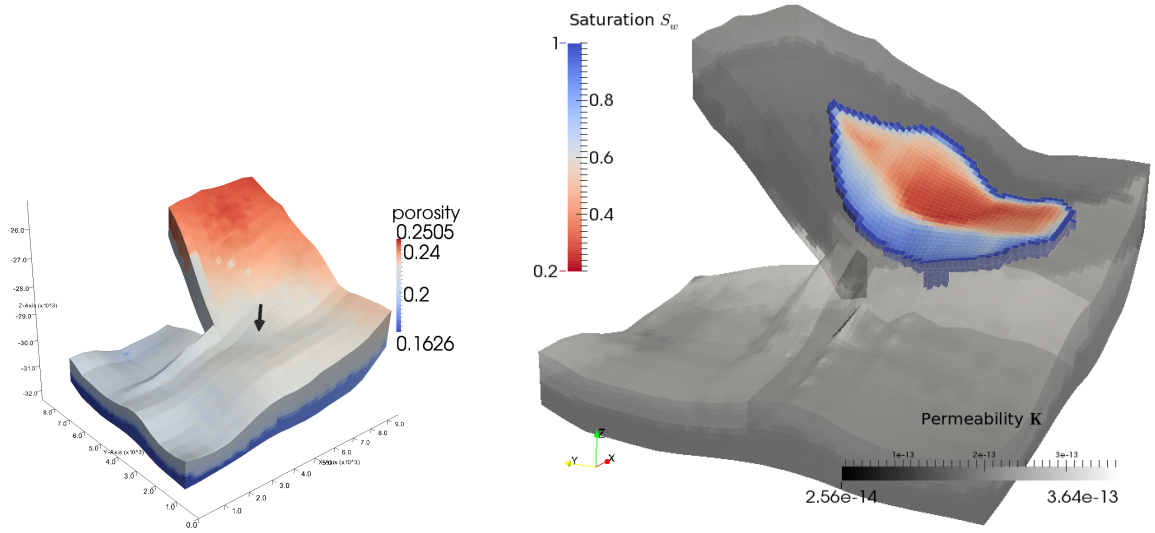

(a) The porosity of the injection formation, an arrow marks the injection well.

(b) Plume of CO_2 after simulation of 50 years. The solution on the simple sub-domain is cut out and not visualised.

Figure 4.3: Injection of CO_2 into the Johansen formation (*Class et al.*, 2009).

Table 4.3 shows the benchmark parameters of four simulation runs applying a uniformly complex model and four simulations employing the multi-physics framework. The margins of the differences introduced by the modeller's decision, which contributes to the model uncertainty, are visualised by repeated model runs that differ only in the regularization bounds to build the volume derivatives (Section 3.3.5).

Failure of the numerical differentiation for small changes in composition is avoided by setting a lower limit for the increment ΔC^κ. The derivatives in volume are necessary to model compositional multi-phase flow, and regularisation gets necessary because the single-phase regions are modelled with the same equation. Naturally, the observed feedbacks are secondary effects, such as volume errors or changes in time-step sizes, that are somehow triggered by different regularisation bounds, and not direct effects of them. The standard regularisation bound ($\Delta C^\kappa \leq 1 \cdot 10^{-8} \cdot \varrho_\alpha$) is flanked by simulations with a lower and a higher bound, and the deviances in model outcome compared to the standard case are listed in brackets in Table 4.3. The deviations between the individual uniformly complex runs are in the same order as the difference to the simulation applying

Table 4.3: Results of the Johansen benchmark, "multi-physics" is abbreviated by MP.

	Secant limit $\frac{\partial \hat{v}}{\partial C^\kappa}$	Dissolved CO_2 in Brine		Residually trapped CO_2		Centre of Mass x	y	z
Uniform	$5 \cdot 10^{-9} \varrho_\alpha$	13.19 %	(-1.6%)	17.59 %	(0.1%)	6264	3242	-2862
Uniform	$1 \cdot 10^{-8} \varrho_\alpha$	13.40 %	(±0%)	17.57 %	(±0%)	6261	3236	-2863
Uniform	$2 \cdot 10^{-8} \varrho_\alpha$	13.19 %	(-1.6%)	17.56 %	(-0.1%)	6264	3242	-2862
Uniform	$3 \cdot 10^{-8} \varrho_\alpha$	13.49 %	(0.7%)	17.70 %	(0.7%)	6265	3244	-2862
MP	$5 \cdot 10^{-9} \varrho_\alpha$	13.07 %	(-0.3%)	17.44 %	(-0.3%)	6261	3241	-2862
MP	$1 \cdot 10^{-8} \varrho_\alpha$	13.11 %	(±0%)	17.49 %	(±0%)	6264	3244	-2862
MP	$2 \cdot 10^{-8} \varrho_\alpha$	13.14 %	(0.2%)	17.50 %	(0.1%)	6263	3243	-2862
MP	$3 \cdot 10^{-8} \varrho_\alpha$	13.14 %	(0.2%)	17.50 %	(0.1%)	6263	3243	-2862

the multi-physics framework.

The individual multi-physics runs differ only marginally because regularisation is hardly necessary: in areas of negligible changes in composition, the multi-physics framework applies the appropriate single-phase pressure equation (4.1) where there are no such volume derivatives. Remaining differences in the solution arise because regularisation still occurs in single-phase cells that belong to the complex sub-domains "safety zone" around the multi-phase plume. It can be nevertheless concluded that the multi-physics framework introduces less bias in the simulation results because the best model is applied locally. However, both approaches encounter difficulties to model the density instability due to dissolved CO_2 in the post-injection period.

4.4.1 Efficiency potential

Figure 4.4 shows the computational efforts for specific tasks throughout the simulation to investigate potential efficiency increases for such large-scale examples. The largest efforts are required to calculate the pressure field, because an implicit solution requires assembling and solving a large system of equations. The multi-physics concept reduces the assembling time, as well as the total time needed for flash calculations. At the end of the simulation, the complex sub-domain covers only 4 % of the total number of cells, which for this case leads to a total speed-up of roughly 40 %. Further reduction in computational efforts is possible if the global degrees of freedom are reduced, for example by coarsening the simulation grid. As no information or accuracy should be lost,

an adaptively refined and coarsened grid provides the required accuracy to produce good results while reducing overall computational costs. Such a strategy will be explained in the following chapter.

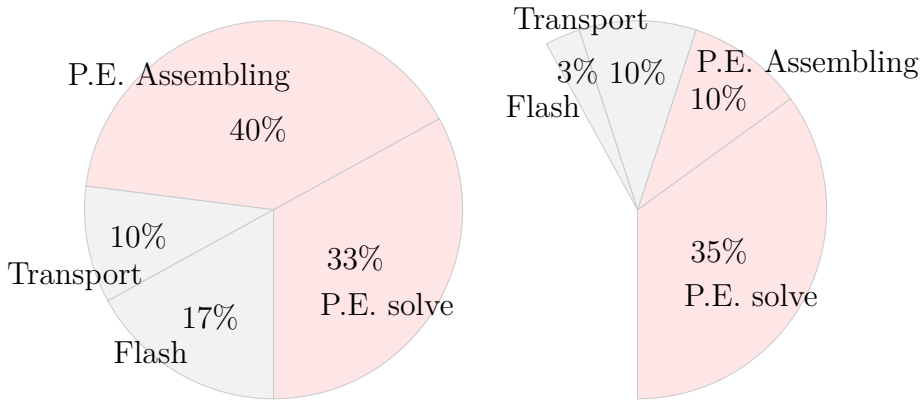

(a) Uniformly complex model (b) Multi-physics framework

Figure 4.4: Computational efforts over the course of simulation, percentages based on total computing time of the uniformly complex model. The pressure equation (P.E., shaded in red) is computationally most expensive.

5 Adaptive grid

One of the modelling challenges, predominantly in the field of petroleum engineering, is to include the considerably smaller geometry of well-heads in comparison with the sheer size of the reservoir cells. In view of limited computational power, global refinement to the desired level is not always possible or feasible. Earliest attempts nested locally refined grids around the wells into the coarse simulation grids (*Akbar et al.*, 1974; *Mrosovsky and Ridings*, 1974) to get measurement data of well pressures into the flow models. Later, the refined areas were properly embedded into the global the global domain (e.g. *Heinemann et al.* (1983); *Ewing* (1988)), providing the flexibility for an extensive use in the petroleum industry. Furthermore, through the use of dynamic grids (e.g. *Han et al.* (1987); *Trangenstein and Bell* (1989)) also transient features such as shock fronts can be refined.

In this work and the references therein, we limit ourselves to manipulations on regular grids, where it is geometrically simple to avoid degenerate elements and the refinement step is a local and hence fast operation (*Bangerth et al.*, 2007). Any local refinement of a regular grid leads to an irregular mesh (Figure 5.1(b)) which can be met by two approaches: a conforming closure of the irregular mesh as a post-processing step by introducing triangles or tetrahedrons versus allowing the hanging nodes and treat them in a special manner. The latter is aimed for in this work, as it preserves the advantages of a regular grid.

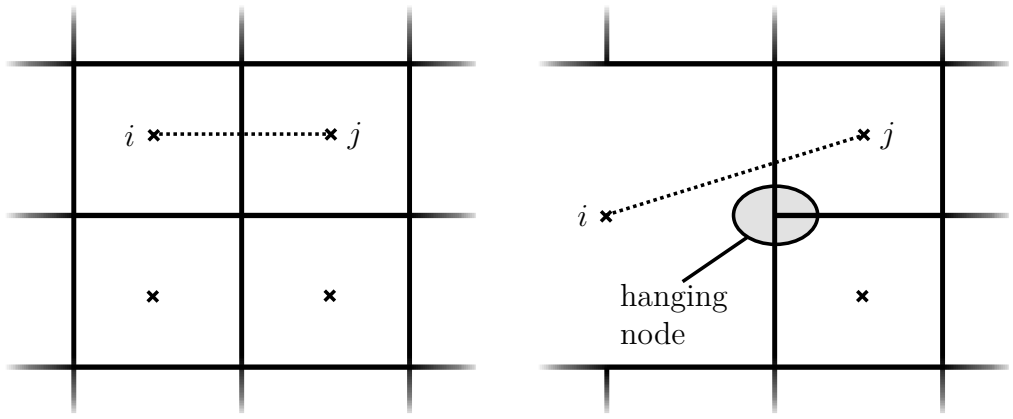

(a) TPFA approximation on a regular grid.

(b) Hanging node configuration because cell i was coarsened.

Figure 5.1: Hanging node situation because of a locally refined/coarsened grid.

5.1 Hierarchical grid structure and general implementation

The simulation grid discretises the whole simulation domain by finite entities. These entities, or cells, are initially created on the same grid level. Grid refinement produces new cells by subdividing the cells of the initial grid (Figure 5.2). Each "father" cell on the zeroth level is replaced by l smaller cells ("sons", Figure 5.3) on the first grid level . In the same allegory, all sons of a father cell can be referred to as "brothers". Subsequent refinement introduces ever higher levels, and a tree structure evolves that contains the father cell and all its descendants. Through this hierarchical tree structure, a unique mapping between levels is possible, a necessary requirement to transfer data (Section 5.2). Naturally, all considerations also hold for the process of coarsening, the amalgamation of several sons to their father cell. Spatial properties such as porosity are defined on a certain level, and this information can simply propagate through higher levels of the grid. The outer cells of this refinement tree form a so-called "leaf grid" (*Bastian et al.*, 2008b). This is the grid on which the balance equations are solved, although the entities of the leaf grid may be on different refinement levels.

A sequential solution procedure on an adaptive grid is shown in Figure 5.4. An adaptivity module is inserted (compare Figure 3.2) at the beginning of each time-step with the following workflow:

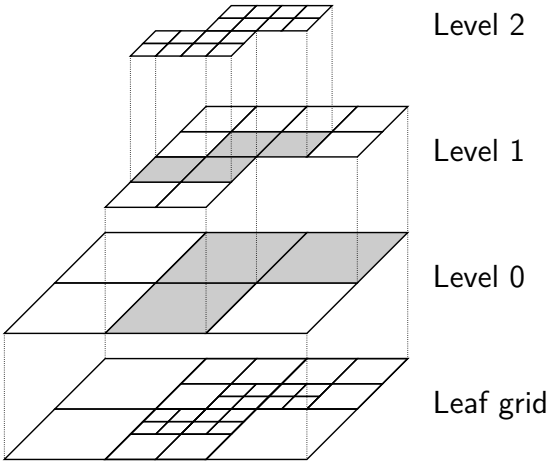

Figure 5.2: Hierarchy of the grid (*Sinsbeck*, 2011).

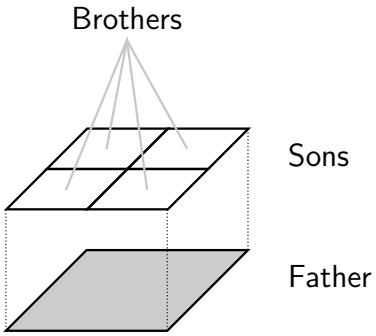

Figure 5.3: Naming conventions.

1. One or a combination of several indicators are calculated locally for each cell. Its comparison with appropriate refinement and coarsening criteria specifies whether and how the cell has to be modified (Section 5.3). Afterwards, each cell is flagged for refinement or coarsening, or remains unchanged.

2. The old solution, essentially the primary variables plus some additional information (Section 5.2), is stored.

3. The grid is modified, starting with a refinement loop and subsequent recessive coarsening wherever possible.

4. A reconstruction step maps the stored old solution on the new grid and thus reassembles the old solution for the next time-step.

5. Flash calculations provide the secondary variables. When applying the multi-physics framework, the sub-domain information is only mapped and not updated to minimise the effects of the grid adaptation.

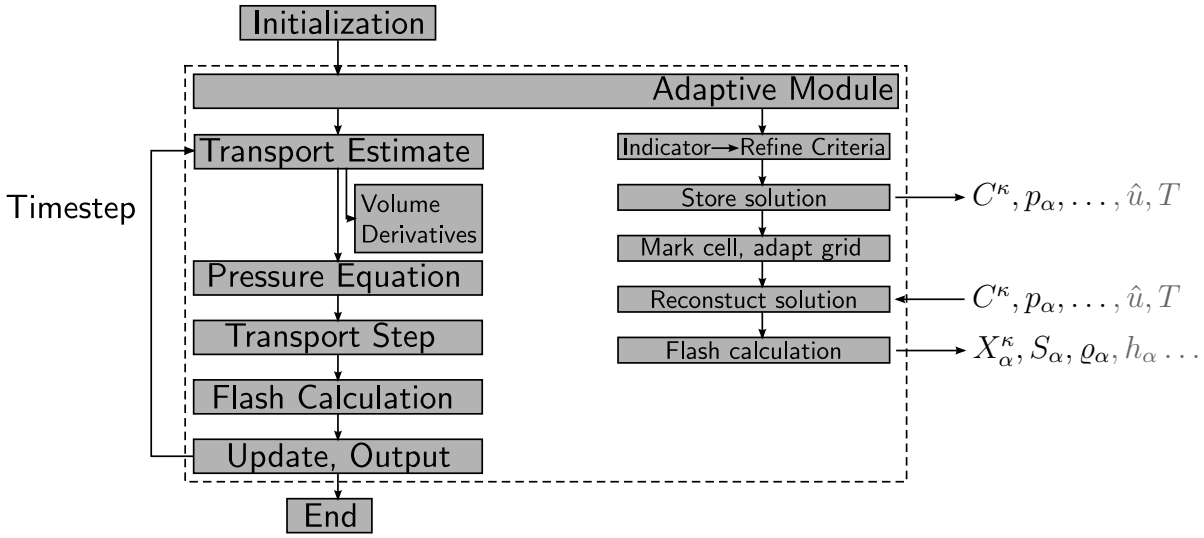

Figure 5.4: The sequential solution scheme on adaptive grids, non-isothermal variables depicted in gray.

5.2 Transformation of the solution, treatment of new cells

After the refinement process of the grid, the old solution has to be transferred to the new grid before solving the next time step. The data of cells that remain on the same level after grid manipulation have to be copied because the grid indexing and thus the internal data strucutre has changed. More work is necessary for cells whose grid level was changed, as either new information has to be generated in the case of refinement or information has to be amalgamated if cells are coarsened. In n_{dim} dimensions, each father is refined to $2^{n_{dim}}$ sons. For each new cell that arises after grid adaptation, the primary variables have to be recomputed (Sections 5.2.1, 5.2.2, 5.2.3). In addition, the specifics of the applied numerical scheme benefit from transferring additional information from the old grid, which is discussed in Section 5.2.4. It is assumed here that the soil properties remain constant between the grid levels, thus up/downscaling methods can be omitted. When the primary variables are transferred, the remaining secondary variables such as density, composition etc. are recalculated through regular flash calculations. The transformation onto the new grid intends to introduce as little bias and errors as possible while being as efficient as possible.

5.2.1 Transformation of the total concentrations

Mass should always be conserved, including the re-gridding process. The total concentrations are specific masses per available volume, which should remain constant if there are no perturbations. Hence, the total concentrations can simply be copied from father cells to their sons, even if the cell volume differs between the l brothers. For the case of a coarsened cell, all mass of the sons have to aggregate to the father cell:

$$C^{\kappa}_{father}\phi V_{father} = m_{father} = \sum_{l=1}^{2^{n_{dim}}} m_{son,l} = \sum_{l=1}^{2^{n_{dim}}} C^{\kappa}_{l}\phi V_{son,l} \tag{5.1}$$

$$C^{\kappa}_{father} = \frac{1}{V_{father}} \cdot \sum_{l=1}^{2^{n_{dim}}} C^{\kappa}_{l} V_{son,l} \tag{5.2}$$

These transformations do not necessarily match thermodynamic densities, as pressure and temperature can change as well during the adaptation. That creates a volume mismatch, which exists anyway due to the sequential non-converged scheme. Compared with the latter, the volume error induced by the transformation of the grid is typically very small.

5.2.2 Transformation of pressure

If a cell is refined, the son cells do not necessarily lie on the same elevation as their father. In the case of a vertical hydrostatic pressure distribution, this difference in altitude would produce different pressures between the brothers, which also affects their density and composition. At best, these changes in pressure caused by changes in elevation should be anticipated during grid adaptation to prevent artificial fluxes or errors introduced by the time-dependent storage term in the pressure equation. To do so, the vector $\mathbf{z}_l$ is defined which points from the cell centre of the son l to the centre of the father. Then, the new pressure of the sons can be gained by

$$\begin{aligned} p_{son,l} &= p_{father} - \hat{\varrho}\mathbf{g}^T\mathbf{z}_l \\ &= p_{father} - \frac{1}{\phi}\sum_{\kappa} C^{\kappa}_{father}\mathbf{g}^T\mathbf{z}_l \ . \end{aligned} \tag{5.3}$$

Accordingly, the pressure in coarsened cells is averaged from l son cells that are adjusted for height differences, so to speak that are elevated to the father's position:

$$p_{father} = \frac{1}{2^{n_{dim}}} \sum_{l=1}^{2^{n_{dim}}} \left(p_{son,l} - \frac{1}{\phi} \sum_{\kappa} C^{\kappa}_{son,l} \mathbf{g}^T \mathbf{z}_l \right) . \tag{5.4}$$

For regular grids where the father's cell centre is in the middle of the son's, a simple averaging of the pressure would be sufficient. Note that this static transformation only maps the old pressure solution to the new grid, which is needed in the storage terms to calculate the (correct) pressure field for the next time-step. I therefore refrain from using more elaborate methods, such as *Nordbotten et al.* (2008). In addition to the pressure primary variable, the capillary pressure is copied from father to the son to speed up the iterative flash calculation, because of an improved initialization of the corresponding phase pressure.

5.2.3 Transformation of internal energy

Energy should be conserved as well. The specific internal energy can thus be treated analogously to Section 5.2.1,

$$\hat{u}_{father} = \frac{1}{V_{father}} \cdot \sum_{l=1}^{2^{n_{dim}}} \hat{u}_l V_{son,l} \tag{5.5}$$

Such a transformation would alter the cells temperature because the pressure is changing according to Section 5.2.2.
As an alternative mapping strategy, the temperature can be copied from father to sons. Then, the corresponding internal energy is recalculated after an isothermal flash at the mapped temperature is carried out. In the course of this work, no significant difference of either method is observed.

5.2.4 Transformation of additional data

Upstream weighting of coefficients in the pressure equation is determined by the pressure field of the last time-step. If the cell is adapted, this is also possible for the outer interfaces of refined sons if the information of flux direction is copied from the father. Fluxes

between the brothers, however, are approximated using central averaging, as the direction of flow is unknown and the quantities to be weighted differ only slightly. After the new pressure field is solved for, the direction is again known and up-winding for the transport and subsequent time-steps becomes possible.

The transport estimate cannot produce meaningful results before the new pressure field is known. The outer fluxes between the modified cells and their neighbours are substantially altered by the grid transformation (Section 5.2.2), and because the flux between the brothers is negligibly small on the transformed pressure field, these fluxes through the outer faces would have an unreasonably high weight: if a dissolved component is allowed to enter a percolated cell but any out-flux (to its brothers) is permitted, the change in mass ΔC^κ might even yield a formation of a second phase, accompanied with a large derivative in specific volume $^{\partial \hat{v}}/_{\partial C^\kappa}$. While originally, this is exactly what the estimate is supposed to accomplish, it would in this case falsely predict a drastic change in volume solely caused by the refinement. Such errors are avoided by copying all fluid derivatives during the transformation process, as they should not differ vastly between father and sons.

Likewise, the sub-domain information is copied during refinement, despite of new flash calculations that are carried out after grid modifications. An update of the sub-domains might jeopardize the accuracy of the safety zone around the areas of high complexity, because the transformation is a local process. During coarsening, the son assigned to the most complex sub-domain dominates its father's assignment.

5.3 Refinement criteria

On adaptive grids, the decision where cells have to be refined or coarsened has to be made according to appropriate criteria or indicators. These criteria might be static in time if geometric features such as wells or fractures are to be captured, or dependent on the dynamics of flow. With regards to the latter, the criteria have to be tailored to the specific simulation example, because its choice critically affects the accuracy of the simulation.

Some criteria are mathematically derived from a certain definition of the discretisation error (*Verfürth*, 1996; *Eriksson et al.*, 1995). They are improved to include non-linear

conservation laws (*Kräner and Ohlberger*, 2000; *Klöfkorn et al.*, 2002) and are being generalized for the type of grid or discretisation used (*Vohralik*, 2008). An alternative refinement strategy tries to gauge each cell's relevance or impact on the global system in order to determine which cells need to be refined (*Vakili-Ghahani and Jansen*, 2012). For the engineering practice, most authors prefer rather simple and heuristic indicators to steer their grid refinement, most-often because of efficiency reasons. Some of these heuristic indicators lean against derived estimators (*Klieber and Riviere*, 2006; *Lavie and Kamp*, 2011), or are related to fluxes or gradients (*Hornung and Trangenstein*, 1997; *Chellamuthu and Ida*, 1995; *Nilsson et al.*, 2005; *Khattri et al.*, 2007; *Pau et al.*, 2012). Heuristic criteria without formal derivation are used in this work as well. While the term "error estimator" is well defined, there is no consensus about the term "error indicator" in the literature (cf. *Paul* (2003); *Chellamuthu and Ida* (1995); *Chen and Dai* (2002)). The latter expression is nevertheless used by some authors to differentiate between heuristic criteria and mathematically derived criteria.

An indicator based on the saturation is selected in the following as an example to explain the common cycle of such indicators:

1. A local indicator is defined, such as the largest difference in saturation over the interfaces γ_{ij} of each cell, $\eta_i = \max_{\gamma_{ij}} |S_i - S_j|$.

2. The range $\tilde{\eta}_{\max}$ of the indicator is determined to normalize the local indicator values. For example, a loop over all cells determines the minimum and maximum saturation $\underline{S_w}, \overline{S_w}$ throughout the simulation domain, then $\tilde{\eta}_{\max} = \overline{S_w} - \underline{S_w}$.

3. The tolerance levels for refinement and coarsening $\underline{tol}, \overline{tol}$ and maximum and minimum grid levels are specified.

4. A second loop over all cells marks the cell i if the condition $\eta_i > \overline{tol} \cdot \tilde{\eta}_{\max}$ is fulfilled and i is not already refined to the maximum refinement level. A loop over the neighbours of i ensures a refinement ratio of $2:1$, i.e. a maximum difference of one level, by also marking the neighbours for refinement if necessary.

5. Mark all cells i for coarsening where $\eta_i < \underline{tol} \cdot \tilde{\eta}_{\max}$ if i has not yet been coarsened to the maximum level and is not yet marked for refinement. Again, a loop over the neighbours prevents coarsening if the refinement ratio will be violated or the marks of all brothers do not allow coarsening.

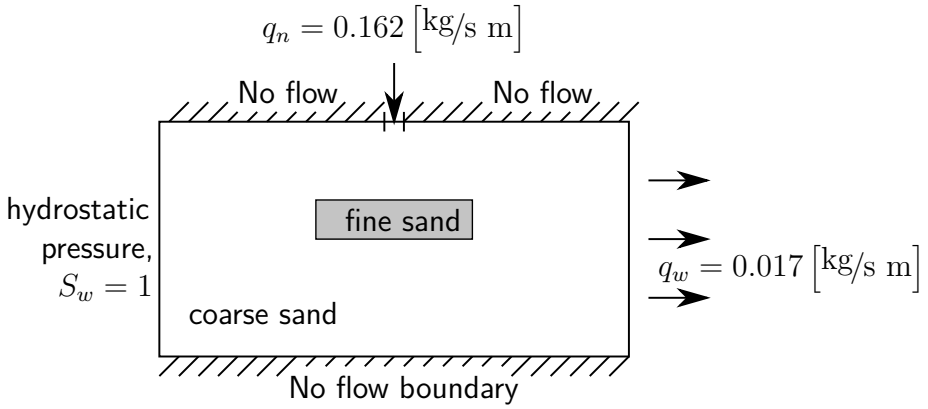

Figure 5.5: Schematic setup of the NAPL injection scenario.

Refinement indicators for compositional multiphase flow are examined an discussed in (*Futter*, 2012), and the major findings relevant to this work are summed up briefly in the following.

5.3.1 On the numerical formulation of the local indicator

A local indicator based on a gradient $\eta_i = \max_{\gamma_{ij}} {}^{|\chi_i - \chi_j|}/_{\Delta x_{ij}}$ would provide an obvious alternative to the absolute difference, as flow is also driven by gradients. The local indicator is thus also affected by its refinement level, through the discretisation length. This favours small cells to be refined and weakens the refinement of coarser cells, and thus increases the overall number of cells (also observed by *Pau et al.* (2012)). The effects of both approaches on the global modelling error are studied in a two-dimensional example of a NAPL (TCE) that infiltrates into a water-saturated porous medium with a horizontal fine-sand lens (Figure 5.5). The NAPL concentration was monitored at three distinct times through the simulation and compared with a fully refined reference solution. The refinement bounds are chosen such that the overall number of cells produced by the different indicators are comparable. The results of the simulation (Table 5.1) favours the indicator based on the local difference, especially towards the later stages of the simulation where least cells remain on level 0. It has to be mentioned though that the system investigated here was single-phase transport, so no capillary flux was involved. Nevertheless, I assume that neglected refinement of coarse cells would also increase the modelling error in multiphase simulations.

Table 5.1: Global L^2-type error ($\sum_i (C_{ref}^{TCE,i} - C^{TCE,i})^2$) in TCE concentration for local indicators dependent on the gradient and the difference of the indicator value.

Simulation time	Gradient	Difference
2000	$7.386 \cdot 10^{-10}$	$5.465 \cdot 10^{-10}$
4000	$3.321 \cdot 10^{-9}$	$2.363 \cdot 10^{-9}$
7500	$1.241 \cdot 10^{-8}$	$5.813 \cdot 10^{-9}$

5.3.2 On the type of variable in the local indicator

In the IMPET framework, the transport is performed along the flow field calculated by the pressure equation. One might be tempted to chose an indicator that directly improves the quality of this flow field based on its related properties: an indicator either based directly on pressure, or alternatively based on the flux calculated from the flow field. Their performance in simulations of multiphase flow and compositional transport is examined here by comparing the error with respect to a fully refined reference solution. As a comparative base case, the standard indicator (Section 5.3) is used for refinement, taking both saturation and mass fraction of dissolved NAPL into account to refine the front of compositional transport as well. Both the refinement and the coarsening bounds are chosen such that the total number of cells produced by the different indicators are similar. This is achieved by trial and error and therefore only an approximate agreement is reached.

A homogeneous porous medium would produce a uniform flow field such that the different indicators have no significant effect. Therefore, simulations are performed on a heterogeneous porous medium where a spatial distribution of porosity values is generated by a "program for geostatistical modelling, prediction and simulation" (GSTAT, *Pebesma and Wesseling* (1998)) and the permeability is calculated with Equation (2.39). The simulation domain of 9 m x 4 m is initially filled with water at $p_w = 2 \cdot 10^5$ Pa and kept closed on top and bottom boundary. Initially, a plume of NAPL resides in residual saturation of $S_n = 0.1$, and the plume's center is located 2 m from left, upper and bottom boundary. A water outflow of $q_w = 0.02\,\mathrm{kg/(s\,m)}$ is imposed on the right side of the domain to keep their influence on the solution as small as possible. The NAPL dissolves gradually into the water and is transported predominantly in horizontal direction because no gravitational forces act.

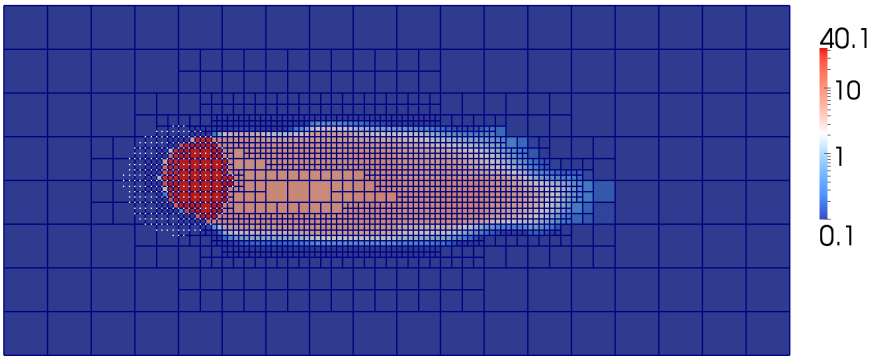

Figure 5.6: NAPL Concentration C^{NAPL} $\left[\text{kg/m}^2\right]$ modelled with the standard indicator set based on differences in saturation and mass fraction X_w^{NAPL}. The initial NAPL plume is marked by white dots.

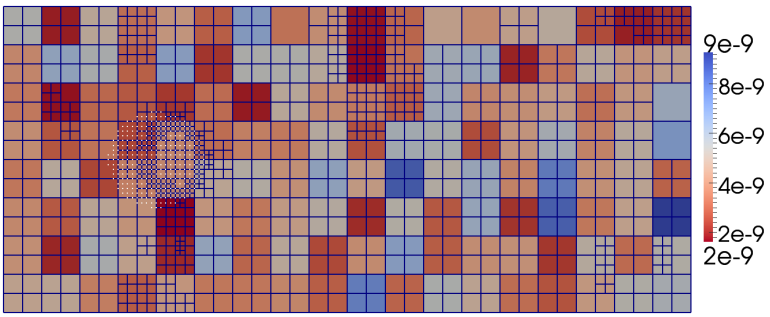

(a) Simulation grid for the indicator based on differences in pressure.

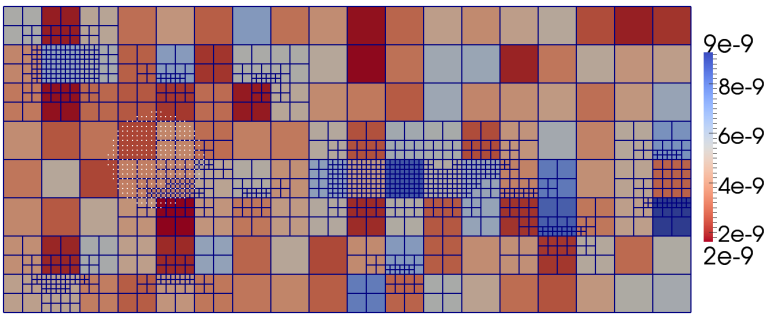

(b) Simulation grid when applying the flux indicator.

Figure 5.7: Permeability of the heterogeneous porous medium, in $\left[\text{m}^2\right]$.

The lowest error is achieved using the standard indicator, because it refines both the transported front and the dissolution zone, but leaves other regions as coarse as possible (Figure 5.6). The pressure indicator leads to fluctuating adaptation of the grid, which yields a higher total error by magnitudes despite keeping the dissolution area refined via differences in capillary pressure: changes in pressure occur when the grid is adapted (Section 5.2.2), which means that the indicator for refinement is dependent on the refinement itself. Secondly, the immanent fluctuations in pressure caused by the error term lead to oscillations in both the grid and thus also the volume discrepancy. The latter issue becomes even more pronounced in a system with significant compressibility and variations of the density with composition, because in comparison, the system of water and NAPL considered here produces only volume discrepancies of below 0.5 %.

The indicator based on the total flux does capture regions of higher flow velocities, but does not keep the dissolution zone refined if the fluxes are low. Overall, the grid rests almost unchanged during the simulation run, which therefore produces the highest errors in NAPL concentration of all three indicator alternatives. As this finding was not anticipated and largely caused by limiting the total amount of cells, the investigation was repeated for the case of gravity-driven flow, where the NAPL initially resides on top of a water-filled heterogeneous porous medium (Figure 5.8(a)). It gradually dissolves in the surrounding water and sinks downwards as the dissolution increases the density of the contaminated water. In this case, the flux indicator (Figure 5.8(c)) is able to refine both regions of higher permeability and the dissolution and propagation fronts. Here, the indicator based on the total flux produces a lower error compared to the standard indicator (based on saturation and mass fraction, Figure 5.8(b)), but also requires more cells and therefore computational time. The global error differs by merely 50 %, which brings forth the conclusion that the standard indicator is a comparably sound and good overall solution, but not necessarily the best for any given problem.

Naturally, the investigations presented here rely on the definition of the soil properties on the coarsest possible grid level. If they live on the finest level and coarse-scale properties are derived via upscaling techniques, the parameter heterogeneity introduces new features on the fine refinement level that are not visible if the grid is coarse. Then, indicators for flux are essential to keep fine-scale flow paths refined (*Wolff*, 2013).

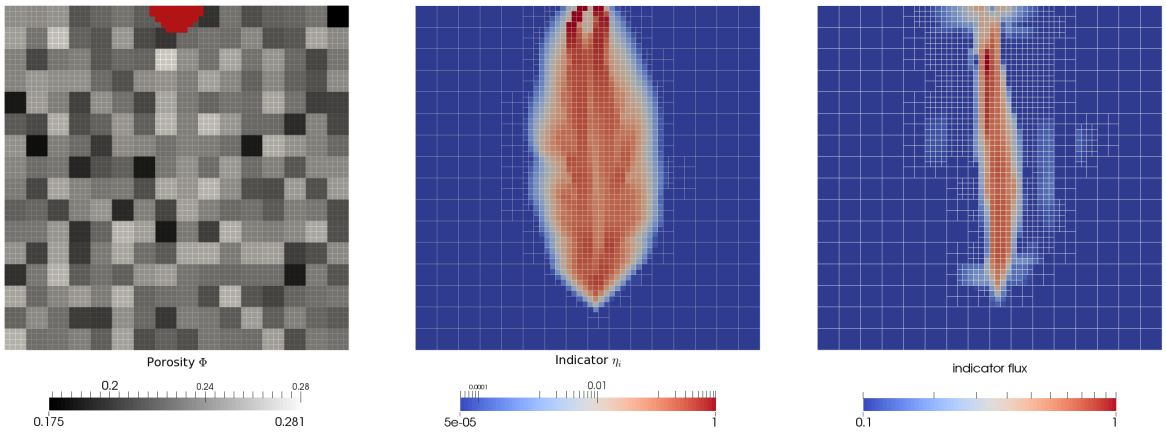

(a) Porosity and initial saturation of the NAPL.

(b) Values of the standard indicator, scaled to refine bound.

(c) Values of the flux indicator, scaled to refine bound.

Figure 5.8: Comparison of the flux and the standard indicator for gravity induced flow.

5.4 Fluxes through irregular faces

In Section 3.3.3, some of the shortcomings of the TPFA method were mentioned. On irregular grids, even in the case of a homogeneous medium, the TPFA fails to reproduce fluxes around the hanging nodes correctly (*Edwards*, 1996), because the two-point stencil does not capture the complex geometry (see also Section 5.5). Several approaches have been developed to address this issue, e.g. *Pau et al.* (2012); *Edwards* (1996); *Wheeler et al.* (2002); *Mehl and Hill* (2002). *Rodrigues and Dickstein* (1996) simply create linearly interpolated pressures along the coarser cells to calculate the flux between cells of different levels.

I solve the problem by using the MPFA method (Section 3.3.3) to increase the flux stencil near the hanging nodes (Figure 5.1(b)). In the case of an irregular face γ_{irreg}, there is always one sub-face with a unique interaction region (Figure 5.9(a)). For the remaining sub-faces (Figure 5.9(b)), different interaction regions are possible that can contain neighbours of both cell i and j, and an appropriate criterion has to be used to select the best flux stencil.

For increased efficiency, I use a combination of the simple TPFA for all regular cell interfaces γ_{reg} whose neighbours are on the same grid level and the local application of the MPFA for all irregular interfaces γ_{irreg} bordering on a hanging node. Therefore, only

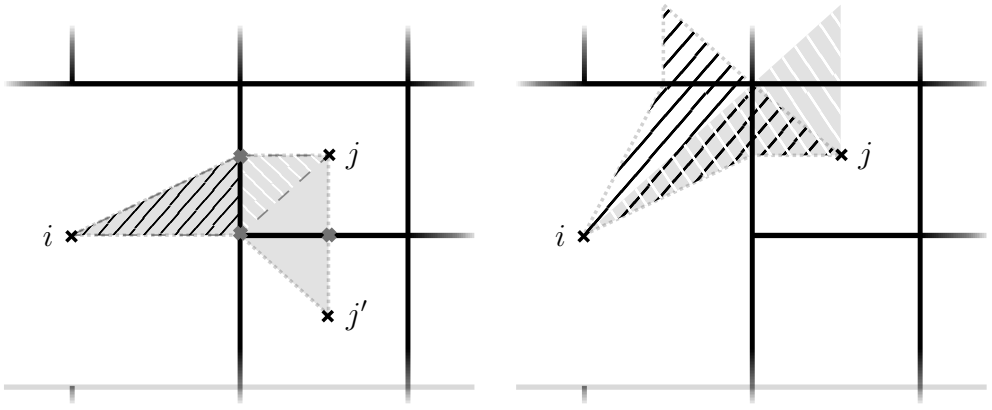

(a) Hanging node configuration approximated with MPFA L-method for the first sub-face between cell i and j. One unique (grey) interaction region also includes the third cell j'.

(b) MPFA: For all remaining sub-faces, several interaction regions are possible, dashed in white and black.

Figure 5.9: Treatment of fluxes around refined cells.

one entry of the flux vector $\mathbf{f}_{\breve{\gamma}^\star}$ is used, so only the respective transmissibility coefficients τ of the full matrix $\boldsymbol{T}$ from Section 3.3.3. The pressure equation (here Equation (3.31) as an example) therefore extends to

$$
\begin{aligned}
& V_i \hat{c} \frac{p_i^t - p_i^{t-\Delta t}}{\Delta t} \\
& - \sum_\gamma \sum_\alpha \varrho_\alpha \lambda_\alpha \left(\sum_k \tau_k p_{\alpha,k}^t - \varrho_\alpha \sum_k \tau_k \mathbf{g}^T \mathbf{x}_k \right) \sum_\kappa X_\alpha^\kappa \frac{\partial \hat{v}_t}{\partial C^\kappa} \\
+ \sum_\gamma \frac{V_i}{U_i} & \sum_\alpha \varrho_\alpha \lambda_\alpha \left(\sum_k \tau_k p_{\alpha,k}^t - \varrho_\alpha \sum_k \tau_k \mathbf{g}^T \mathbf{x}_{\hat{k}} \right) \sum_\kappa X_\alpha^\kappa \frac{\frac{\partial \hat{v}_j}{\partial C_j^\kappa} - \frac{\partial \hat{v}_i}{\partial C_i^\kappa}}{\Delta x} \\
& = V_i \sum_\kappa \frac{\partial \hat{v}}{\partial C^\kappa} q_i^\kappa + V_i \alpha_r \frac{v_t - \phi}{\Delta t} \, . \qquad (5.6) \\
& \text{with } k = \{i, j\} \text{ and } \tau_k = A_\gamma \mathbf{n}_\gamma^T \boldsymbol{K} \mathbf{d}_k \frac{1}{\Delta x} \text{ if } \gamma = \gamma_{\text{reg}} \, , \\
& \text{and } k \in |I| \text{ and } \tau_k \text{ according to Section 3.3.3 if } \gamma = \gamma_{\text{reg}} \, .
\end{aligned}
$$

In the matter of an irregular face, the flux through γ_{ij} is the sum of the fluxes of all considered sub-faces. If there are not as many interaction regions considered as there are sub-faces, the available flux is projected on the total area by multiplication with ${}^{A_{\gamma_{ij}}}/_{(\sum_{\breve{\gamma}_{ij}} A_{\breve{\gamma}_{ij}})}$. Such weighting is performed at the boundary to circumvent costly calculations that mitigate the deficiencies of the MPFA at dirichlet boundaries, because

the domains considered in this work are typically large enough that the influence of the boundary should be minimal. Plus, it allows to investigate the effects of the number of interaction regions considered in Section 5.5. The capillary flux is also gained via the MPFA, because all corresponding phase pressures in the interaction region have to be calculated

$$f_{pc} = A_\gamma \mathbf{n}_\gamma^T \mathbf{K} \lambda_w \varrho_w \frac{\partial v_t}{\partial C^\kappa} \nabla p_c^{t-\Delta t} = \lambda_w \varrho_w \frac{\partial v_t}{\partial C^\kappa} \sum_k \tau_k p_{ck}^{t-\Delta t} \ . \tag{5.7}$$

The indices on the secondary variables in Equation (5.7) are again for the case of p_n being primary variable. The gradient in volume derivatives is not interpolated by an MPFA-ansatz, as it is only an interpolation between cells where mass transport actually takes place. To summarise the formulas, all gradients that drive flow through irregular interfaces that are normally approximated by a TPFA are now expressed through the MPFA-L-method. Although this is done in all types of pressure equations and all transport equations, only the compositional multiphase pressure equation is chosen as an example.

5.5 Numerical example on an adaptive grid in two dimensions

A two-dimensional domain with homogeneous soil parameters that is fully filled with brine and confined by closed boundaries on top and bottom is chosen for a comparative study of the different flux approximations for the irregular faces. The simulation parameters are listed in Table 5.2. Supercritical CO_2 is injected from the left side into the reservoir (2.5 km depth) at a rate of $0.55^{\text{tons}}/(\text{day m})$, and gravity drives the plume upwards. The evolution of the plume is simulated using a static fine grid (the reference), an adaptive gridding with a TPFA approach (tpfa) and two different MPFA-schemes on the hanging nodes: simulations entitled "mpfa 1 IR" use only one interaction area per irregular interface. Those labelled "mpfa" regard both half-edges separately, therefore building two transmissivity matrices for each edge near hanging nodes. Note that fluxes through all conventional faces are treated by the TPFA method, regardless of the differing treatment on hanging nodes.

Figure 5.10 depicts the saturation of the wetting phase after a 2 year injection period. The vertical lines mark the centre of mass of the CO_2 plume, and one black line marks

Table 5.2: Parameters for the two-dimensional injection of supercritical CO_2 into brine.

Porosity	Permeability	BC-Parameter p_d	λ	CFL factor a	Error factor a_e	Lower bound $\underline{e}$	Bound limit $\overline{e}$
0.15	$1 \cdot 10^{-13}\,\mathrm{m}^2$	500 Pa	2	0.7	0.5	0.001	0.9
Adaptive grid properties:		Indicator η_i		Levels	$\underline{tol}$	$\overline{tol}$	
		$\max_{\gamma_{ij}} \lvert S_i - S_j \rvert$		0-5	0.05	0.04	

the reference tip of the plume. Below, the simulation grid of the current time-step is shown. Both the tip of the front and the centre of mass prove that both simulations using the MPFA method improve the resemblance of the fluxes, which yields a better match with the static reference than the TPFA simulation. Figure 5.11 visualises the error in form of a L^1-type norm ($(S^i_{w,ref} - S^i_w)$). The improvement in accuracy is clearly visible, especially at the injection front. The simulation results are mapped on the reference grid, so an additional volumetric weighting of the error (see *Sun and Takayama* (2003)) is not necessary. The accumulated L^2-norms,

$$\xi = \sum_i (S^i_{w,ref} - S^i_w)^2 / \sum_i (S^i_{w,ref})^2 \tag{5.8}$$

read $143.4 \cdot 10^{-5}$ for tpfa, $7.6 \cdot 10^{-5}$ for mpfa 1 IR and $1.35 \cdot 10^{-5}$ for mpfa. These findings indicate that the simpler MPFA-version with only one interaction region might be a reasonable compromise between improvement in accuracy and computational as well as programming efforts: the second interaction region is heavily influenced by the configuration of surrounding cells, which requires non-local operations. The computation times for this simple example including also a subsequent post-injection phase of three years are very encouraging: compared to the reference solution on the static grid (representing 100 % CPU time), the h-adaptive grid lowered that to 16.5 % for tpfa and 15.6 % for mpfa 1 IR, or 15.8 % for mpfa, respectively.

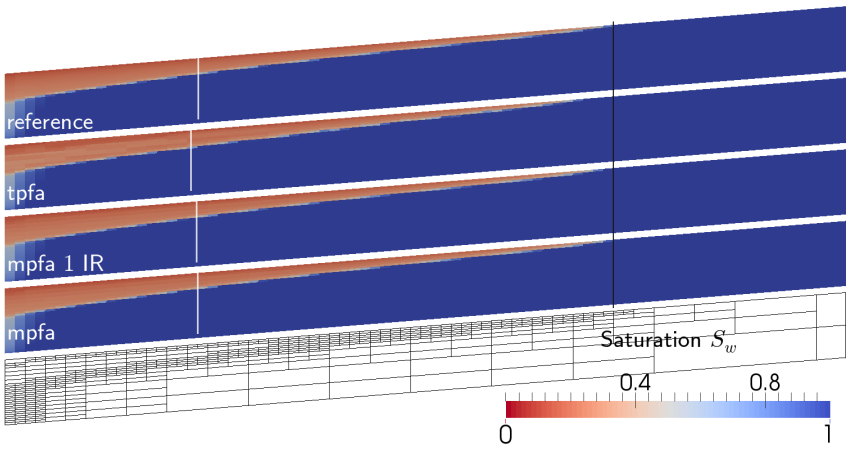

Figure 5.10: Comparison of a saturation front on a static grid (top) with an adaptive TPFA approximation (below) and two ways of using the MPFA-method (bottom).

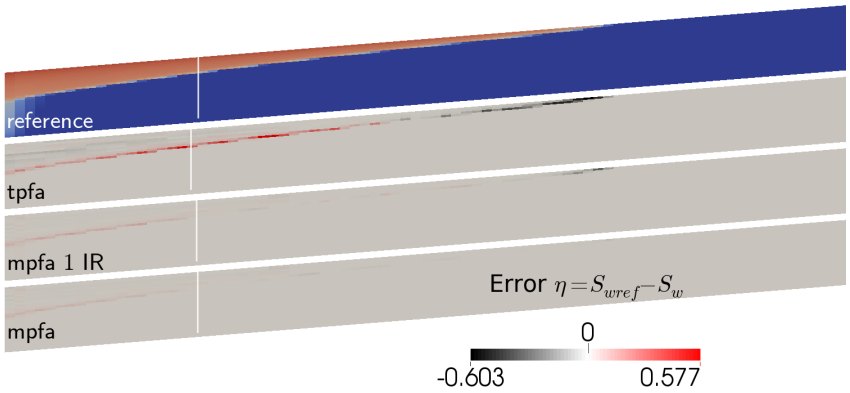

Figure 5.11: Comparison of a saturation front on a static grid (top) with an adaptive TPFA approximation (below) and two ways of using the MPFA-method (bottom).

5.6 Extension to three dimensions

In three dimensions, it is possible to build 4 interaction volumes per irregular face: again, there is one unique interaction region around the hanging node, see Figure 5.12. The remaining three interaction volumes heavily depend on the surrounding cells, that can even lie on different grid levels (Figure 5.13(a)). Each interaction volume is not unique, hence multiple versions have to investigated (see Figures 5.13(b), 5.13(c)) and the best is selected according to appropriate criteria (*Aavatsmark*, 2007; *Wolff et al.*, 2013a).

After the experience from two dimensions (Section 5.5) one might be tempted to disregard

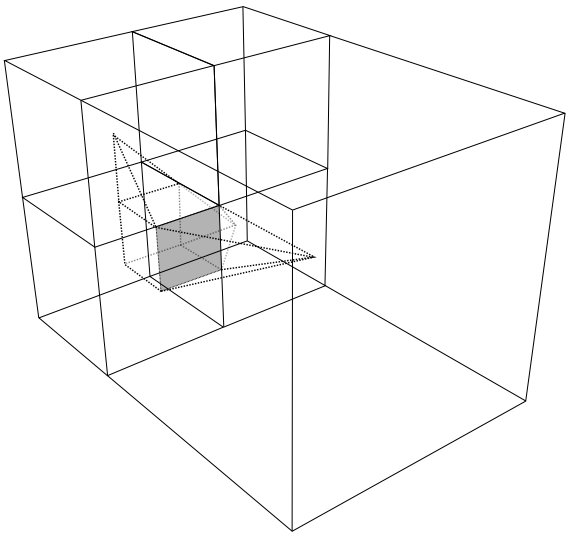

Figure 5.12: The unique interaction region determining the flux through the greyed sub-face.

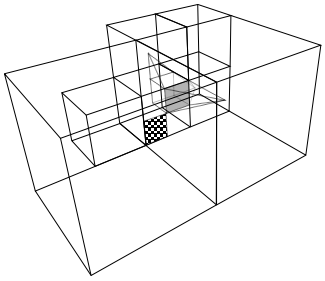

(a) Neighbours can be on different levels.

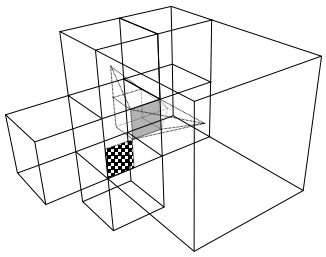

(b) Possible interaction region with two small cells.

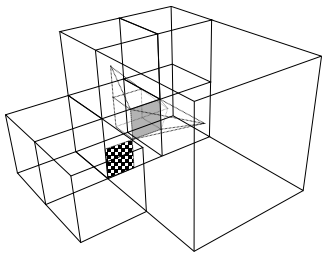

(c) One exemplary alternative interaction region.

Figure 5.13: Interaction regions for the same sub-face marked by a checkerboard pattern.

the complex interaction regions in three dimensions for efficiency reasons. With flux expressions based on only one interaction region, though, problems with monotonicity arise (*Aavatsmark et al.*, 2010). Non-monotone solutions might occur on plank-shaped cells even in homogeneous material. To briefly visualise these, a small example (Figure 5.14) is set up with cells with an unfavourable height-ratio, where injection takes place on one side into the central upper 6 cells. The simulation parameters are the same as listed in the upper part of Table 5.2, and the injection rate is $8.64^{\text{tons}}/\text{day}$. The grid had 3 different levels and was statically refined near the injection. Gravitational effects and capillary pressure are neglected, and a direct solver is used. The solution with one interaction region (Figure 5.12) shows a non-physical pressure field (Figure

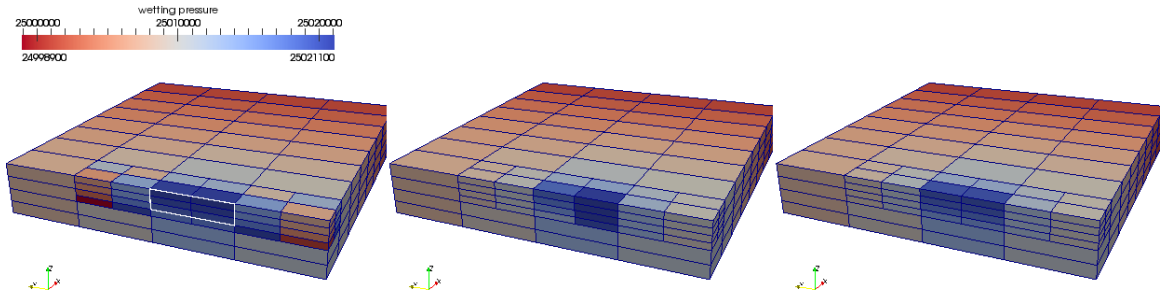

Figure 5.14: Pressure fields produced by using one interaction region per face (left), two (middle) and complete four interaction regions per sub-face (right), after approximately 160 days of injection.

5.14 on the left). Two interaction regions (Figures 5.13) produce a meaningful, however still non-symmetric, solution (Figure 5.14 middle). Only a full consideration of all four interaction regions yields a good pressure field (Figure 5.14 right).

6 Large-scale numerical examples

Both large-scale examples in this Section intend to show the applicability of the proposed concepts on field-scale problems. They shed light on the strengths and potential on one side, but on the other side expose the deficiencies of the methods presented.

6.1 Injection into the Johansen formation

By modelling the fluxes near hanging nodes with an MPFA, it is possible to simulate the large-scale example from Section 4.4 on an adaptively refined grid. As described at the end of the last chapter, a successful simulation of the whole 50 year period is only possible if all four interaction regions are considered in the vertical direction. A TPFA on an adaptive grid produced too large errors in the flux that the decoupled solution scheme eventually failed, at the latest during the post-injection phase. The parameters and setup remain as the simulations on the static grid (Table 4.2), with additional parameters to steer grid adaptation listed in Table 6.1.

Figure 6.1(a) shows the saturation of water at the end of the simulation on an adaptively refined grid. Compared with the coarse solution (Section 4.4), the CO_2 plume of the upper layer extends wider, especially in the up-dip direction. Figure 6.1(b) depicts the plume at the end of the injection period, with more coarsened cells in the middle of the plume, which become refined again after injection stopped because the CO_2 accumulates under the overlying cap-rock. Figure 6.1(c) is clipped up to the injection well for better visibility, showing still several layers of coarsened cells.
The dissolved amount of CO_2 is reduced to 11.3 % on the adaptive grid (compared to 11.5 % on a static globally refined grid), a trend that was also reported by others (e.g. *Bergmoa et al.* (2009); *Green and Ennis-King* (2012)). Integral indicators are important aspects to asses the storage potential, and their sensitivity to the grid

Table 6.1: Parameters for grid adaptation of the Johansen benchmark

Indicator η_i	Levels	$\underline{tol}$	$\overline{tol}$
$\max_\gamma \lvert S_i - S_j \rvert$	0-1	0.05	0.03

resolution emphasises the need for refined simulations of field-scale problems: a solution with grid convergence has obviously not yet been reached. A resolution of effects such as gravity fingers would require even more refinement (*Elenius and Johannsen*, 2012). Global refinement, however, demands such high computational resources that parallel code became essential, while the adaptive simulation is still feasible on a single-processor infrastructure.

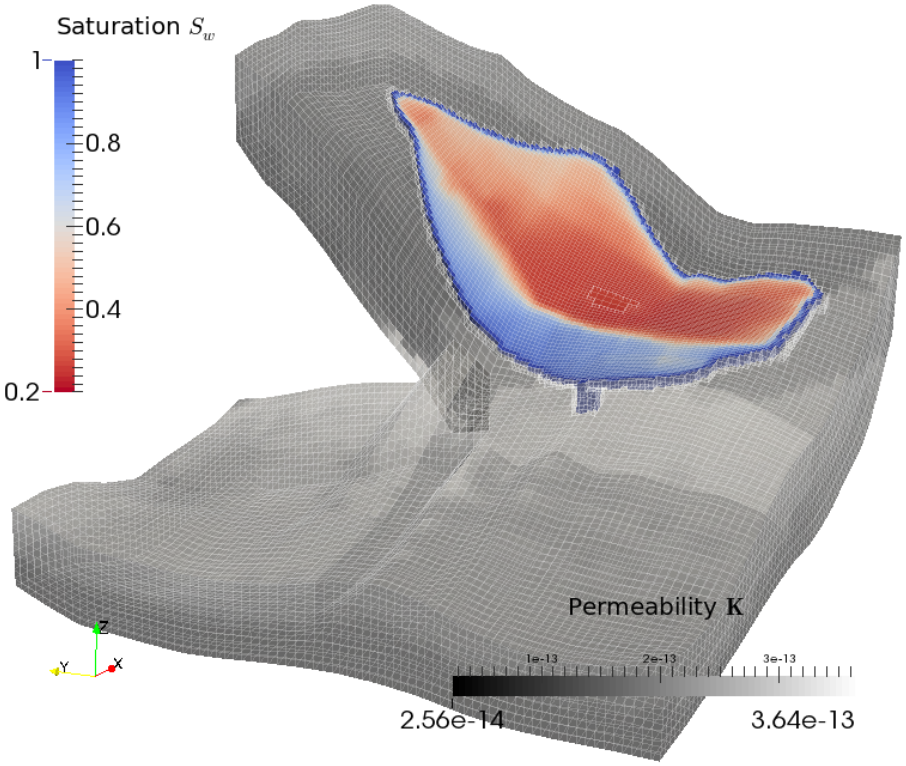

(a) Plume of CO_2 after simulation of 50 years on an adaptively refined grid.

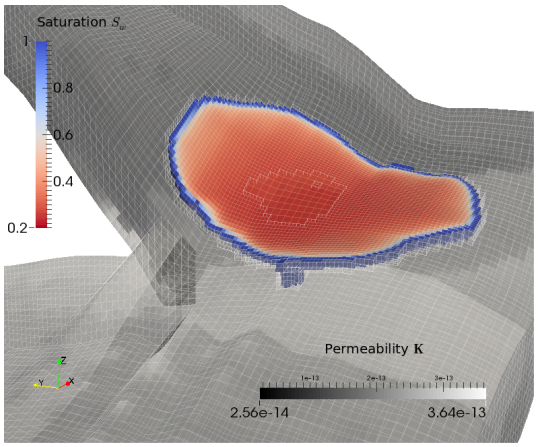

(b) Plume of CO_2 at the end of the injection period (25 years).

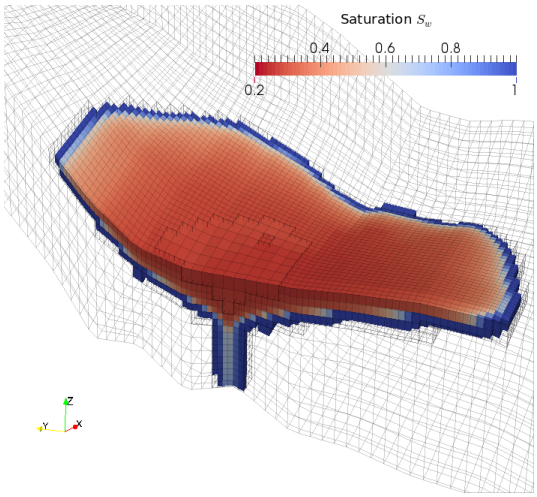

(c) Clip thorugh the grid and CO_2-plume after 25 years.

Figure 6.1: The Johansen benchmark simulated on an adaptively refined grid. Visible is always only the most complex sub-domain.

6.2 Modelling of the Tensleep formation

A further large-scale example has been selected to show the general applicability of the concepts presented in this work for a very challenging physical problem. The Tensleep formation contains to the only federally owned and operated oil field in the US, with the benefit that the reservoir data are in the public domain. In the course of its operation, strategies such as gas injection for enhanced oil recovery were introduced in the field, because water has been produced for decades (*Friedmann and Stamp*, 2006). It can be thus assumed that the accessible flow paths are already fully filled with brine water.

Due to its dome structure (Figure 6.2), being one interval within the "teapot dome" oil

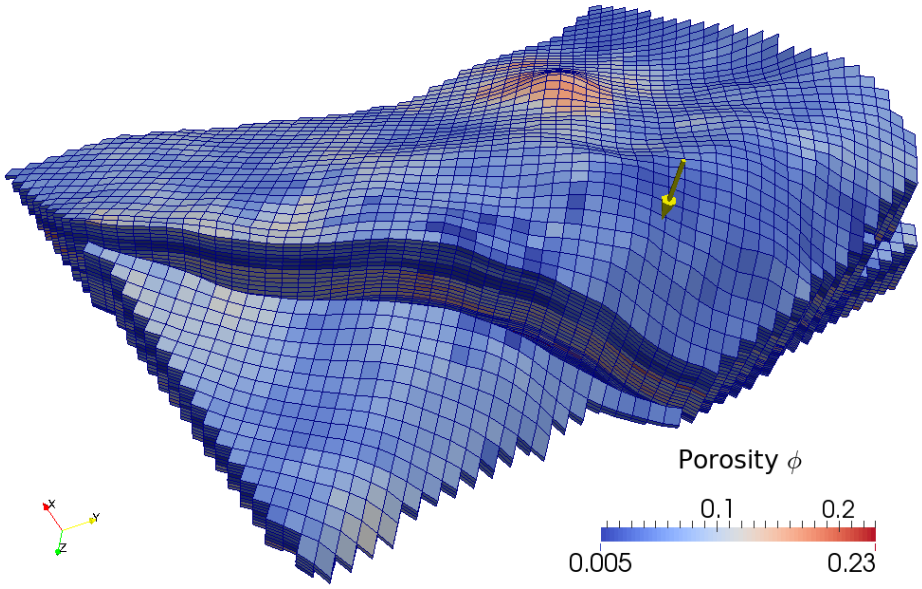

Figure 6.2: Porosity distribution in the tensleep formation, vertically exagerated by a factor of 4. The yellow arrow marks the injection well.

field, and its detailed data availability, this formation is perfectly suited for scientific studies on CO_2 injection. The combination of underground CO_2 storage and withdrawal of hot reservoir fluid to produce geothermal energy is currently attracting increasing interest (e.g. *Randolph et al.* (2013); *Salimi and Wolf* (2012); *Buscheck et al.* (2013)). After decades of production, the Tensleep formation still remains at approximately 88 °C and abundant wells are available as well, thus a concurrent geothermal usage of extracted formation fluid is considered. Such a scenario provides an excellent challenge to apply the concepts presented in this work to a real-world subsurface problem: using

the Tensleep formation for concurrent CO_2 storage and geothermal extraction requires a numerical framework that can handle the complex physical processes pertinent to both applications. Considering the global simulation domain, both types of physical complexity occur in constricted regions, which is perfectly suited for the multi-physics framework. Covering almost 40 000 cells, the model domain is large enough that efficient methods are essential.
This section attempts to show a proof of concept under challenging conditions and is neither intended to investigate the feasibility of such an operation nor evaluate the injection strategy. An extensive discussion of the simulation results is therefore omitted, the focus lies on possible weaknesses that arise when simulating with the adaptive concepts.

6.2.1 Description of the formation and simulation setup

The full simulation domain is depicted in Figure 6.2, featuring a dome structure that is intersected by a large sealing fault. The simulation grid follows the geological model, which was built using seismic data and data from 15 well logs, which also yields the porosity values of the rock matrix. This field is populated with fractures from a stochastic model, derived from well and outcrop data, that is validated by history matching against the production curves (*Jamal et al.*, 2013). An application of an appropriate dual-continuum–model is beyond the scope of this work, although the heavily fractured reservoir demands it. As the matrix permeability is very low and the fracture network highly connected, the simulations in this chapter use the fracture permeability but the porosity of the matrix, fully acknowledging that the exchange processes between the two continua are not properly modelled.
The bottom and top of the domain is confined by a no-flow boundary, with hydrostatic pressure conditions on the side boundaries at 2370 psi ($\approx$ 16 MPa) on the reference level of 60 m below sea level (*Chiaramonte et al.*, 2012). As done in that study, the well "44-1-TpX-10" is the injection well, open to the flow of 104 $\frac{\text{tons}}{\text{day}}$ of CO_2. It is injected at 35 $^\circ$C into the sandstone layer, which has the highest storage capacity.
The grid managers accessible by DUNE providing grid adaptivity are not able to manage the non-conforming cell interfaces along the faults. In order to apply grid refinement, the cells behind the faults (that *Chiaramonte et al.* (2008) showed to be sealing) are

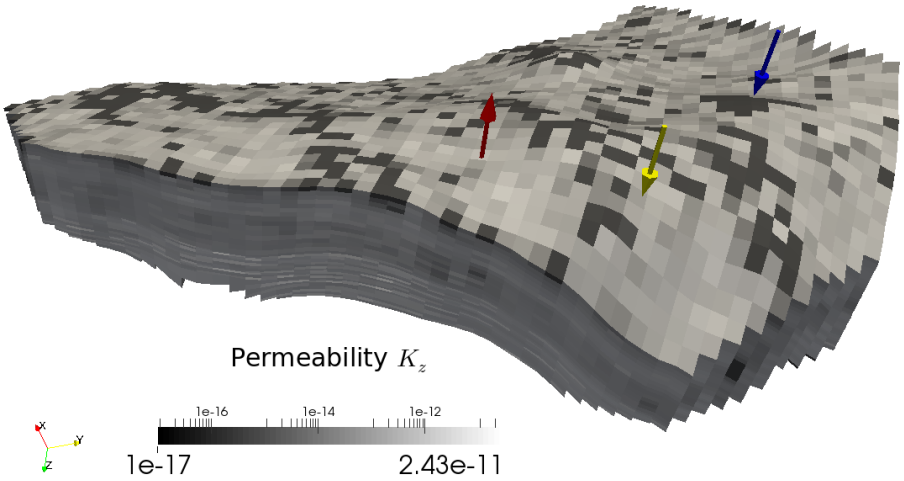

Figure 6.3: Simulation domain for adaptive simulation runs without degenerating elements, showing the vertical permeability K_z in [m^2], vertically scaled by factor four.

cut out and only the main area where the wells are located remain in the simulation domain (Figure 6.3).

The multi-physics framework considers four different levels of complexity, all include compositional and compressible effects (Table 4.1):

- A full non-isothermal two-phase region evolves near the CO_2 injection well. This is the most complex model, which is also applied in all cells containing wells.

- A two-phase model with a linear approximation of temperature is applied in regions where the CO_2 plume has already reached the reservoir temperature.

- Full non-isothermal effects under single-phase conditions are modelled near the cold brine injection well, and below the CO_2 injection well where gravitational forces prevent CO_2 in phase but where the reservoir temperature has been altered by the injection.

- A single-phase model with a linear approximation of temperature is applied in the far-field region of the reservoir.

Table 6.2: Simulation parameters for the Tensleep formation.

Residual saturations		BC-Parameter		CFL	Error	Lower	bound
$S_{w,r}$	$S_{n,r}$	p_d	λ	factor a	factor a_e	Bound $\underline{e}$	limit $\overline{e}$
0.1	0.1	2000 Pa	2	0.7	0.3	$1 \cdot 10^{-5}$	0.9
Adaptive grid properties:		Indicator η_i			$\underline{tol}$	$\overline{tol}$	Levels
		$\max_\gamma \lvert S_i - S_j \rvert$			0.05	0.001	0-1
		$\max_\gamma \lvert T_i - T_j \rvert$			0.05	0.001	
		F_i after Equation 3.55			0.5		

6.2.2 Numerical obstacles to simulate the field

Due to the combined constraints on the geometrical dome structure and the underlying rock properties, some grid cells suffer from strongly deformed ("twisted") cell faces, see Figure 6.4. The grey cell i resides above the black-edged cell j, thus the vector connecting the cell's centres $\mathbf{d}_{ij}$ points downwards. The figure also depicts the normals $\mathbf{n}_{\gamma_i}$ on the centre points of all interfaces γ_i. In the case of the interface γ_{ij} between the gray and black-edged cell, $\mathbf{n}_{\gamma_{ij}}$ points upwards because this interface γ_{ij} is strongly twisted. Direct exploitation of Equation (3.39) would yield a reverted flux because $\mathbf{n}_\gamma^T \mathbf{d}_{ij}$ becomes negative. Such a inversion is avoided by using the absolute value of the term $|\mathbf{n}_\gamma^T \mathbf{K} \mathbf{d}_{ij}|$ to calculate the fluxes.

The parameter range of the initial soil data set was found too broad and required some regularisation: the porosity is limited to a minimum of $\phi = 0.005$, and the minimum fracture permeability in each direction is not allowed to surpass $K = 1 \cdot 10^{-17}$. The average matrix permeability is $K \approx 8.5 \cdot 10^{-15}$, so lower values are very unlikely and such a limit still allows for permeability variances around six orders of magnitude.

Any simulation only with a standard indicator to refine the injection fronts, in a combination of temperature and saturation indicator, eventually leads to a non-physical pressure field which terminates the simulation abruptly. Only the additional implementation of a flux indicator in combination with the standard indicators allowed for successful simulation. To prevent oscillating refinement and coarsening (Section 5.3.2), each cell that is refined by the flux indicator can only be coarsened thereafter if four consecutive adaptation steps do not call for a refinement. This check is performed on the lowest grid level, so the condition has to be met by all sons.

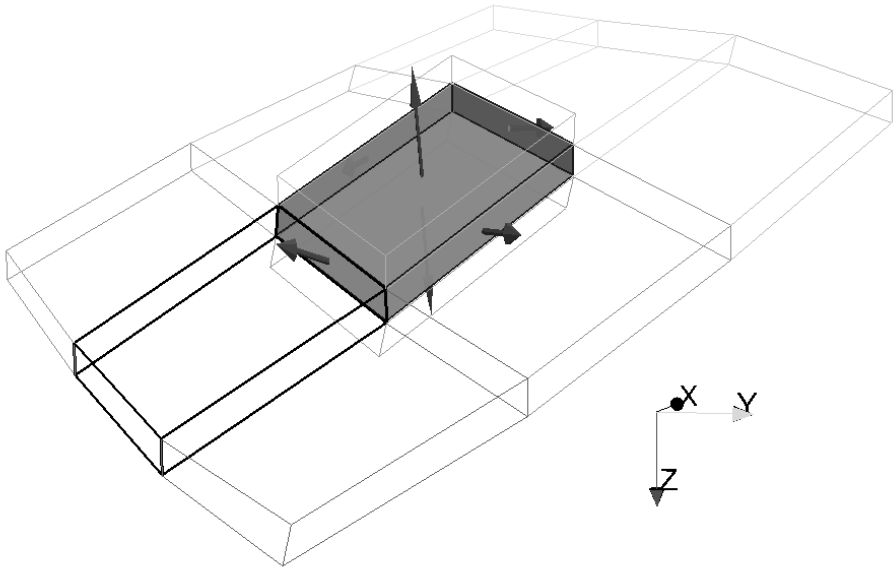

Figure 6.4: Twisted faces may lead to skewed face normals and require a modified flux term.

6.2.3 Simulation Results

Preliminary runs show that the injected CO_2 rapidly rises through the fracture network and accumulates below the cap-rock (see also *Chiaramonte et al.* (2012)), where the plume spreads above the target interval whose large porosity would provide the desired storage capacity. In fact, the front approaches the domain border after only a year of injection (Figure 6.5). For the coupled geothermal usage, I decided to inject brine at 40 °C into well "56-TpX" (blue arrow), and extract the hot reservoir fluid from well "54-TpX" (red arrow). This creates a counter-current flow of water to slow down the propagating CO_2 front while maintaining flow into the extraction well.

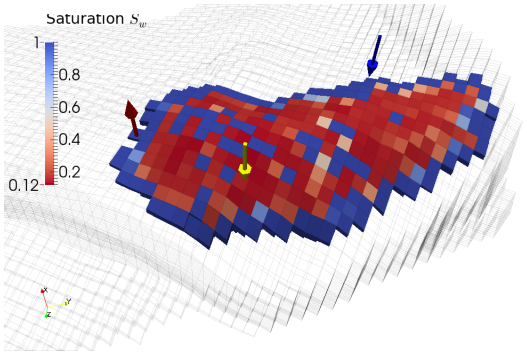

Figure 6.5: CO_2 plume after roughly one year of injection.

Highly heterogeneous flow-paths through cells with a very low porosity yield severely small time-steps down to 20 minutes. Although the comparison of computational efforts

is to be treated with care, simulation with a uniform model (2p2cni) demanded around seven times the computation time of the multi-physics model during the first month, with equal number of time-steps and no detectable differences in the results.

Within one year of injection, the cold CO_2 does not lead to a substantial decrease in temperature in the vicinity of the well. The injection of cold water, however, reduces the formation temperature gradually, leading to a zone of significant temperature differences around the injection well. After 290 days, this zone begins to interact with the CO_2 plume, depicted in Figures 6.6. The extend of the two-phase and the non-isothermal sub-domains are depicted in Figure 6.6(a). Figure 6.6(b) visualises how CO_2 remains above the desired storage formation, while temperature effects through water injection is observable in this layer. In that period, the injection of 60 ktons of brine and an extraction of 75 ktons of hot water (and 57 tons of CO_2) could not significantly influence the CO_2 injection of 30 ktons.

On adaptive grids, the size of the time-step is restricted significantly stronger, which translates to 10 000 time-steps to simulate $2 \cdot 10^6$ seconds. Figures 6.7 show the CO_2 plume and the temperature decrease at two time-steps. All single-phase quasi-isothermal cells are removed to show the adaptively refined grid. The Sub-figure 6.7(b) shows the CO_2 injection area on the coarse grid at approximately the same time as Sub-figure 6.7(a), clearly showing the lack of detail due to the coarse mesh.

Figure 6.8 provides a more detailed view of the CO_2 injection area viewed from below. The detailed flow paths of the CO_2 start to be visible. Under the extraction well, some cells are refined by the flow indicator which might not necessarily improve the simulation result, but due to their small grid-size in the vertical direction have an influence on the size of the time-step. Here, further development of the flux indicator would be beneficial to trigger refinement only to prevent simulation failure.

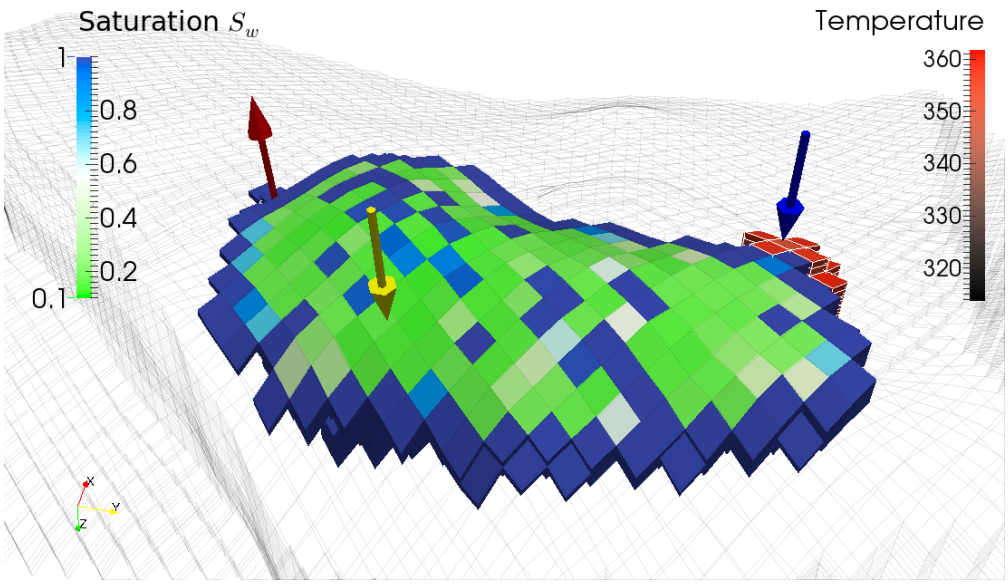

(a) Plume of CO_2 and extend of the two-phase-subdomain. Cells that belong to the non-isothermal sub-domain have white corners and show the temperature distribution around the injection wells.

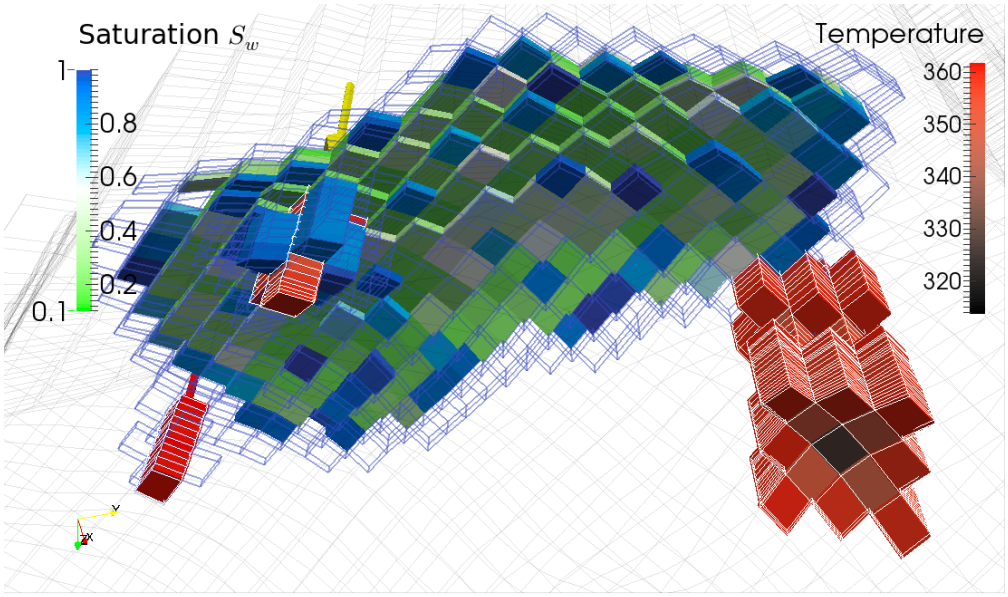

(b) View from below the formation at the two-phase cells and cells belonging to the non-isothermal sub-domain (cornered white and showing the temperature scale). The extend of the two-phase sub-domain is marked by blue corners.

Figure 6.6: Simulation after 290 days of CO_2 injection (yellow arrow) and geothermal extraction (red arrow) with cold-water injection (blue arrow) modelled with the multi-physics approach. The cells of the non-isothermal sub-domain are cornered white.

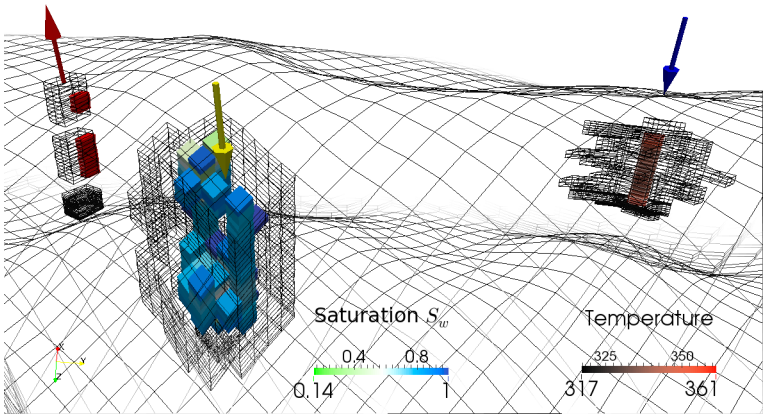

(a) Adapted grid after $4 \cdot 10^5$ seconds.

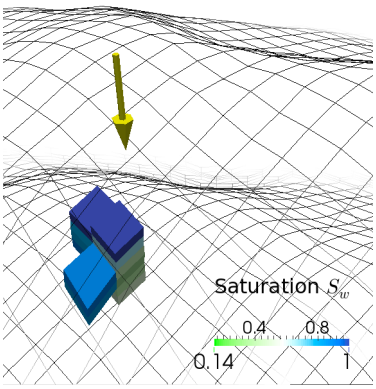

(b) Fix coarse grid after $4 \cdot 10^5$ seconds.

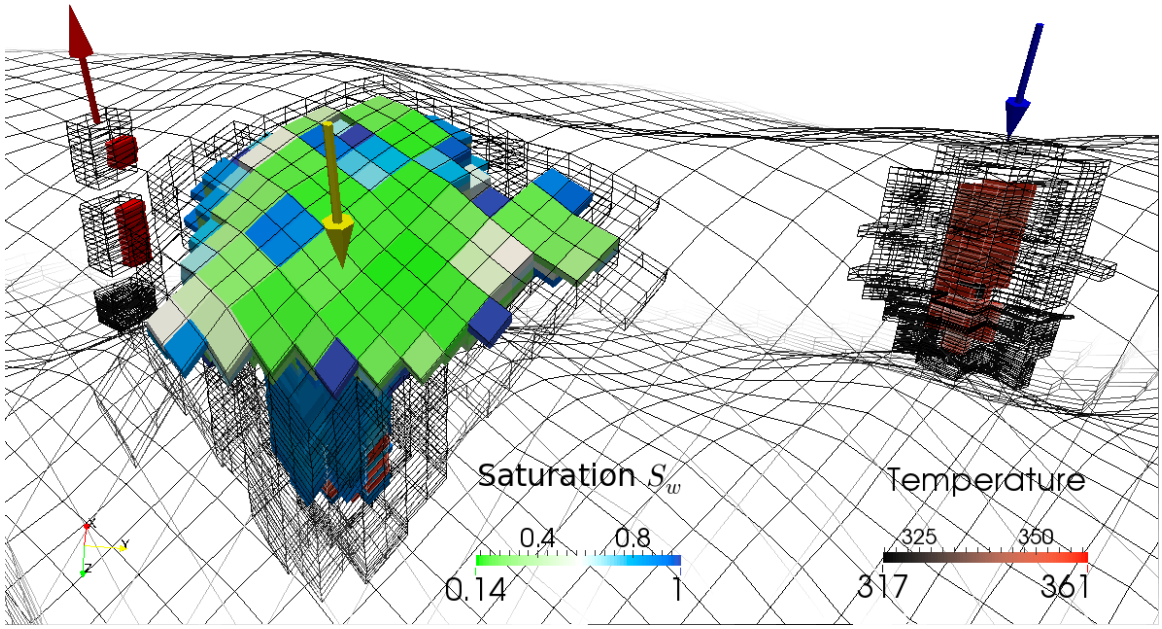

(c) Adapted grid after $2 \cdot 10^6$ seconds.

Figure 6.7: CO_2 plume and non-isothermal sub-domain (cornered white) on an adaptive grid.

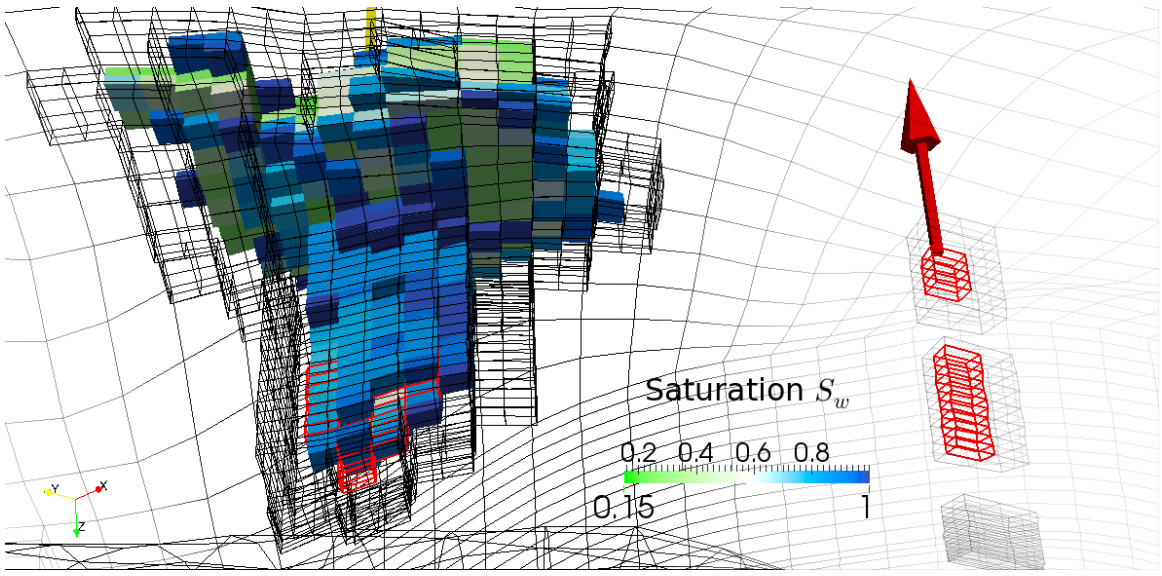

Figure 6.8: CO_2 injection and extraction well from below, non-isothermal sub-domain in red.

7 Final Remarks

7.1 Summary

This work combines two adaptive modelling strategies for compositional multi-phase flow in porous media, including non-isothermal effects. Firstly, a multi-physics concept selects different numerical models locally depending on the physical processes at hand. Secondly, an adaptive modification of the simulation grid is used to locally track features of interest with a refined grid while globally remaining as coarse as possible.

In Chapter 2, the fundamental properties and functional relationships are introduced. The basic properties of fluids and fluid mixtures, as well as thermodynamic concepts for compositional effects such as laws of equilibrium are presented. In the context of porous media, the complex interplay between solid and fluids yields further functional dependencies on the relevant scale, from a large-scale description of capillary pressures to the resistance to flow of heat and mass. The governing balance equations close the chapter briefly.

The discretisation of the system in Chapter 3 starts with an introduction to the two general temporal solution strategies, the *fully implicit* (or *coupled*) and the *sequential* (or *decoupled*) scheme. The latter approach is followed in this work, reformulating the balance equations into one pressure equation and sequentially performed transport equations, that are followed by equilibrium calculations to determine the fluids' composition. Costly iteration is avoided by using a pressure equation determined via a volume balance, whose additional terms require thorough numerical treatment. The multi-point flux approximation (MPFA) is an alternative to the traditional estimation of fluxes, that overcomes several deficiencies of the standard approach. After a detailed description of the equilibrium calculations, small examples demonstrate the applicability

of the individual models and a comparison with the results obtained by fully implicit approaches.

The first step towards adaptivity is accomplished in Chapter 4 by bonding the individual models together in the aforementioned multi-physics framework. The disadvantage that the applied numerical sequential solution procedure is bound time-step–wise is exploited in this process to reduce surplus computational efforts. A large-scale example related to CO_2 sequestration illustrates the potential and applicability of the framework, showing both a reduction in modelling bias and gains in efficiency in assembling time as well as a reduction of flash calculations.

Further improvements can be accomplished by modelling on a dynamically refined grid, which is introduced in Chapter 5 as the second adaptive strategy. Although being applied in many fields, this work is the first attempt to use adaptive grids with the selected numerical approach. Appropriate indicators that steer the grid modification are required, and if the grid is altered, the solution scheme has to continue with transferred data. As the traditional approach to compute fluxes fails on such adaptive grids, the MPFA method discussed above can be used instead.

The combination of both adaptive strategies is showcased on the large-scale CO_2 injection scenario in Section 6.1, proving to be advantageous to non-adaptive strategies where only the complex model on a globally refined grid is applied. Finally, the applicability of the concepts on field problems is visualised in Section 6.2, which is based on an existing reservoir with challenging reservoir properties.

7.2 Outlook

Non-isothermal three-phase three-component The non-isothermal extension should be made available to the three-phase three-component, and at best be nested into the grid-adaptive framework. For fluid systems considered in classical environmental problems, the strong temperature dependency of the solubility limit, and hence the equilibrium ratios, might still be solvable by the simple iterations in the flash calculations discussed in Section 3.4.3. The solution transfer during grid modification, of course, becomes more involved and differences in the proposed methods of Section 5.2.3 will probably be significant. Experimental setups such as

Webb and Phelan (1997) may be simulated with this framework to validate the model.

Varying degree of implicitness The CFL-criterion of the explicit transport model tends to be very restrictive. This becomes even more severe if the grid resolution is refined. Possible alternatives might include IMPSAT models, where both pressure and some transported quantities including the saturation are treated implicitly, while the remaining variables remain explicit in time (*Haukås et al.*, 2007; *Cao*, 2002). Any relaxation of the CFL limit, however, requires alternate strategies to adapt the sub-domains.

Time-stepping Significant volume discrepancies evolve if the fluxes are no more dominated by advection and the size of the time-steps varies strongly from one to the next step. Then, the error correction in the pressure equation, being directly dependent on the time-step size, jeopardizes a successful simulation. A systematic investigation on representative scenarios can provide insights which additional measures need to be incorporated and if schemes acknowledging a multitude of parameters such as *Coats* (2003) yield a more stable result.

Application The wide range of applications that would benefit from the presented methods has not yet been fully covered. Advectively dominated problems with weak coupling should be preferably chosen, as there lies the strength of the decoupled solution scheme. The field of multi-component transport under pure single-phase conditions but with non-isothermal effects, such as modelling the convection of brine under geothermal use with explicitly modelled transport of salts, is currently untouched, and could be supplemented with a multi-physics implementation of a geomechanical model.

The previous chapter indicated in addition that application on hard data sometimes require increased measures for numerical stability. A well model such as (*Peaceman*, 1978) eases harsh pressure gradients that evolve if injection is realized through constant sources or sinks, especially in view of significantly heterogeneous material parameters around the well. Successful simulation of thousands of time-steps required carefully gauged error-term factors, which could be avoided by restart routines or an inclusion of iteratively solved time-steps performed only in the infrequent cases that might lead to a numerical breakdown, e.g. through massively reduced size of the time-step.

Benchmarking Many other simulation frameworks have implemented their own specific attempts to remain stable under challenging situations. Typically, these occur if multiple effects intertwine and the system to solve becomes that complicated that no analytical solution can be found any more. The lack of such a reference might be one reason for sometimes surprisingly diverging simulation results (*Class et al.*, 2009; *Nordbotten et al.*, 2012) depending on the solution method and simulation framework. Comparison studies on similar, challenging setups with other codes can help in reducing model uncertainty and facilitate a step towards a verification of the model.

Up-scaling In this work, the up-scaling methods for soil properties such as porosity and permeability are circumvented by defining the parameter values on the coarsest grid level. In contrary, the best representation of the flow field is achieved if the detailed resolution is accompanied by detailed information of the porous medium, which is then up-scaled to representative quantities in coarser grid blocks (see references in Section 2.2.1 and *Gerritsen and Durlofsky* (2005)). Advanced methods including multi-phase effects and capillary pressure are under development (*Wolff et al.*, 2013b), and in the case of compositional flow, its fine-scale distribution might be included as well (*Salehi et al.*, 2013).

7.3 Reproducibility of the simulation results

It is attempted to accompany all simulations in this work by the details necessary to reproduce the findings, especially with regards to numerical parameters (e.g. Table 4.2) that ensure a successful termination of the simulation or model assumptions in the mathematical formulations. A complete description, however, lies beyond the scope of such a manuscript. Part of the publication work was the integration of the code in the software project DuMu^{x} (*Flemisch et al.*, 2011) including code documentation. In order to fill in potential information gaps, the DuMu^{x} and DUNE revision numbers in Table 7.1 allow for a full insight into the code which produced the results and figures presented.

Table 7.1: Subversion revision numbers of the source code used.

Section	Dune stable release	Dumux svn version
3.5.1	2.2.0	stable r10436
3.5.2	2.2.0	stable r11386, devel r11391
4.4	2.2.0	stable r10981
5.5	2.2.0	stable r11386, devel r10667
6.1	2.2.0	stable & devel r10981
6.2	2.2.0	stable r11386, devel r11652

Bibliography

I. Aavatsmark (1995). *Mathematische Einführung in die Thermodynamik der Gemische.* Wiley-VCH.

I. Aavatsmark (2007). *Multipoint flux approximation methods for quadrilateral grids.* 9th International Forum on Reservoir Simulation, Abu Dhabi.

I. Aavatsmark, T. Barkve, O. Bøe, and T. Mannseth (1994). *Discretization on non-orthogonal, curvilinear grids for multi-phase flow.* In *4th European Conference on the Mathematics of Oil Recovery.*

I. Aavatsmark, T. Barkve, O. Bøe, and T. Mannseth, *Discretization on non-orthogonal, quadrilateral grids for inhomogeneous, anisotropic media. Journal of Computational Physics*, 127 (1996)(1), 2–14.

I. Aavatsmark, G. T. Eigestad, B. T. Mallison, and J. M. Nordbotten, *A compact multipoint flux approximation method with improved robustness. Numerical Methods for Partial Differential Equations*, 24 (2008), 1329–1360.

I. Aavatsmark, G. T. Eigestad, B. ove Heimsund, B. Mallison, J. M. Nordbotten, and E. Øian, *A new finite-volume approach to efficient discretization on challenging grids. SPE Journal*, 09 (2010), pp. 658–669.

G. Ács, S. Doleschall, and E. Farkas, *General purpose compositional model. Society of Petroleum Engineers Journal*, (1985), 543–553.

R. Agarwal, Y.-K. Li, L. Nghiem, and D. Coombe, *Multiphase Multicomponent Isenthalpic Flash Calculations. Journal of Canadian Petroleum Technology*, 30 (1991)(3).

A. M. Akbar, M. D. Arnold, and A. H. Harvey, *Numerical simulation of individual wells in a field simulation model. Society of Petroleum Engineers Journal*, 14 (1974)(4), 315–320.

V. Artus and B. Noetinger, *Up-scaling two-phase flow in heterogeneous reservoirs: current trends. Oil & gas science and technology*, 59 (2004)(2), 185–195.

P. W. Atkins and J. De Paula (2002). *Atkins' Physical chemistry.* Oxford University Press, Oxford.

K. Aziz and A. Settari (1979). *Petroleum Reservoir Simulation.* Elsevier Science Publishers.

W. Bangerth, R. Hartmann, and G. Kanschat, *deal.ii—a general-purpose object-oriented finite element library. ACM Trans. Math. Softw.*, 33 (2007)(4), 24.

J. W. Barker and S. Thibeau, *A critical review of the use of pseudorelative permeabilities for upscaling. SPE Reservoir Engineering*, 12 (1997)(2), 138–143.

P. Bastian, M. Blatt, A. Dedner, C. Engwer, R. Klöfkorn, R. Kornhuber, M. Ohlberger, and O. Sander, *A generic grid interface for parallel and adaptive scientific computing. part ii: implementation and tests in DUNE. Computing*, 82 (2008a)(2), 121–138.

P. Bastian, M. Blatt, A. Dedner, C. Engwer, R. Klöfkorn, M. Ohlberger, and O. Sander, *A generic grid interface for parallel and adaptive scientific computing. part i: abstract framework. Computing*, 82 (2008b)(2), 103–119.

P. Bastian, M. Droske, C. Engwer, R. Klöfkorn, T. Neubauer, M. Ohlberger, and M. Rumpf (2005). *Towards a unified framework for scientific computing.* In *Domain Decomposition Methods in Science and Engineering, volume 40 of LNCSE*, pages 167–174. Springer-Verlag.

J. Bear (1972). *Dynamics of Fluids in Porous Media.* Elsevier, New York.

J. Bear, D. Zaslavsky, and S. Irmay (1968). *Physical Principles of Water Percolation and Seepage.* Unesco.

J. B. Bell, G. R. Shubin, and J. A. Trangenstein, *A method for reducing numerical dispersion in two-phase black-oil reservoir simulation. Journal of Computational Physics*, 65 (1986)(1), 71–106.

P. Bergmoa, A.-A. Grimstad, E. Lindeberg, F. Riis, and W. T. Johansen (2009). *Exploring geological storage sites for CO_2 from norwegian gas power plants: Utsira south.* In *Proceedings of the 9th International Conference on Greenhouse Gas Control Technologies (GHGT-9)*, volume 1, pages 2953 – 2959.

A. Bielinski (2006). *Numerical Simulation of CO_2 Sequestration in Geological Formations.* Ph.D. thesis, Institut für Wasserbau, Universität Stuttgart.

P. Binning and M. A. Celia, *Practical implementation of the fractional flow approach to multi-phase flow simulation. Advances in Water Resources*, 22 (1999)(5), 461–478.

P. J. Binning and M. A. Celia, *Pseudokinetics arising from the upscaling of geochemical equilibrium. Water Resour. Res.*, 44 (2008)(7), W07410–.

A. Burri, A. Dedner, R. Klöfkorn, and M. Ohlberger (2006). *An efficient implementation of an adaptive and parallel grid in dune.* In E. Krause, Y. Shokin, M. Resch, and N. Shokina, editors, *Notes on Numerical Fluid Mechanics and Multidisciplinary Design*, volume 91, pages 67–82–. Springer Berlin Heidelberg.

T. A. Buscheck, T. R. Elliot, M. A. Celia, M. Chen, Y. Sun, Y. Hao, C. Lu, T. J. Wolery, and R. D. Aines, *Integrated geothermal-CO_2 reservoir systems: Reducing carbon intensity through sustainable energy production and secure CO_2 storage. Energy Procedia*, 37 (2013)(0), 6587–6594.

H. Cao (2002). *Development of techniques for general purpose simulators.* Ph.D. thesis, Stanford University.

K. Chellamuthu and N. Ida, *'a-posteriori' error indicator and error estimators for adaptive mesh refinement. Compel-the International Journal for Computation and Mathematics in Electrical and Electronic Engineering*, 14 (1995), 139–156.

Z. Chen and S. Dai, *On the efficiency of adaptive finite element methods for elliptic problems with discontinuous coefficients. SIAM J. Sci. Comput.*, 24 (2002)(2), 443–462.

Z. Chen and R. E. Ewing, *Comparison of various formulations of three-phase flow in porous media. Journal of Computational Physics*, 132 (1997), 1–23.

Z. Chen, Q. Guan, and R. Ewing, *Analysis of a compositional model for fluid flow in porous media. SIAM Journal on Applied Mathematics*, 60 (2000)(3), 747–777.

L. Chiaramonte, M. Zoback, J. Friedmann, and V. Stamp, *Seal integrity and feasibility of co2 sequestration in the teapot dome eor pilot: geomechanical site characterization. Environmental Geology*, 54 (2008)(8), 1667–1675–.

L. Chiaramonte, M. D. Zoback, J. S. Friedmann, and V. W. Stamp (2012). *3d stochastic reservoir model and fluid flow simulation of a CO_2-EOR pilot in a fractured reservoir.* In *Carbon Management Technology Conference*. Carbon Management Technology Conference, Orlando, Florida, USA.

H. Class (2001). *Theorie und numerische Modellierung nichtisothermer Mehrphasenprozesse in NAPL–kontaminierten porösen Medien.* Ph.D. thesis, Mitteilungsheft 105, Institut für Wasserbau, Universität Stuttgart.

H. Class (2008). *Models for non-isothermal compositional gas-liquid flow and transport in porous media.* Habilitation, Universität Stuttgart.

H. Class, A. Ebigbo, R. Helmig, H. Dahle, J. Nordbotten, M. Celia, P. Audigane, M. Darcis, J. Ennis-King, Y. Fan, B. Flemisch, S. Gasda, M. Jin, S. Krug, D. Labregere, A. Beni, R. Pawar, A. Sbai, S. Thomas, L. Trenty, and L. Wei, *A Benchmark Study on Problems Related to CO_2 Storage in Geologic Formations. Computational Geosciences*, 13 (2009)(4), 409–434.

H. Class and R. Helmig, *Numerical simulation of non-isothermal multiphase multicomponent processes in porous media.: 2. applications for the injection of steam and air. Advances in Water Resources*, 25 (2002)(5), 551–564.

H. Class, R. Helmig, and P. Bastian, *Numerical Simulation of Nonisothermal Multiphase Multicomponent Processes in Porous Media - 1. An Efficient Solution Technique. Advances in Water Resources*, 25 (2002)(5), 533–550.

H. Class, R. Helmig, J. Niessner, and U. Ölmann (2006). *Multiphase processes in porous media.* In R. Helmig, A. Mielke, and B. Wohlmuth, editors, *Multifield Problems in Solid and Fluid Mechanics*, volume 28 of *Lecture Notes in Applied and Computational Mechanics*, pages 45–82. Springer Berlin / Heidelberg.

K. Coats, *A note on impes and some impes-based simulation models. SPE Journal*, 5 (2000)(3), 245–251.

K. Coats, *Impes stability: Selection of stable timesteps. SPE Journal*, 8 (2003)(2), 181–187.

R. Courant, K. Friedrichs, and H. Lewy, *Über die partiellen differenzengleiehungen der mathematischen physik. Mathematische Annalen*, 100 (1928), 32–74.

M. Darcis (2012). *Coupling Models of Different Complexity for the Simulation of COStorage in Deep Saline Aquifers*. Ph.D. thesis, Universität Stuttgart.

N. Darman, G. Pickup, and K. Sorbie, *A comparison of two-phase dynamic upscaling methods based on fluid potentials. Computational Geosciences*, 6 (2002)(1), 5–27.

E. Dicks (1993). *Higher Order Godunov Black-oil Simulations for Compressible Flow in Porous Media*. Ph.D. thesis, University of Reading.

P. Dietrich, R. Helmig, M. Sauter, H. Hölzl, J. Köngeter, and G. Teutsch (2005). *Flow and Transport in Fractured Porous Media*. Springer Verlag.

S. Doerr, R. Shakesby, and R. Walsh, *Soil water repellency: its causes, characteristics and hydro-geomorphological significance. Earth-Science Reviews*, 51 (2000)(1-4), 33–65.

L. J. Durlofsky (2005). *Upscaling and gridding of fine scale geological models for flow simulation*. In *8th International Forum on Reservoir Simulation Iles Borromees, Stresa, Italy*, pages 20–24.

M. G. Edwards, *Elimination of adaptive grid interface errors in the discrete cell centered pressure equation. Journal of Computational Physics*, 126 (1996)(2), 356 – 372.

M. G. Edwards and C. F. Rogers (1994). *A flux continuous scheme for the full tensor pressure equation*. In *Proceedings of 4th European Conference on the Mathematics of Oil Recovery*. EAGE, Norway.

M. T. Elenius and K. Johannsen, *On the time scales of nonlinear instability in miscible displacement porous media flow. Computational Geosciences*, 16 (2012), 901–911.

K. Eriksson, D. Estep, P. Hansbo, and C. Johnson, *Introduction to adaptive methods for differential equations. Acta Numerica*, 4 (1995), 105–158 M3 – 10.1017/S0962492900002531.

R. Ewing, R.E. Lazarov (1988). *Adaptive local grid refinement.* In *SPE Rocky Mountain Regional Meeting.*

B. Faigle, R. Helmig, I. Aavatsmark, and B. Flemisch, *Efficient multi-physics modelling with adaptive grid-refinement using a mpfa method. Computational Geosciences*, (2013). (accepted).

B. Flemisch, M. Darcis, K. Erbertseder, B. Faigle, A. Lauser, K. Mosthaf, S. Müthing, P. Nuske, A. Tatomir, M. Wolff, and R. Helmig, *Dumux: Dune for multi-Phase,Component,Scale,Physics, flow and transport in porous media. Advances in Water Resources*, 34 (2011)(9), 1102–1112.

P. Forsyth Jr. and P. Sammon, *Practical considerations for adaptive implicit methods in reservoir simulation. Journal of Computational Physics*, 62 (1986)(2), 265–281.

S. J. Friedmann and V. W. Stamp, *Teapot dome: Characterization of a CO_2-enhanced oil recovery and storage site in Eastern Wyoming. Environmental Geosciences*, 13 (2006)(3), 181–199.

J. Fritz (2010). *A Decoupled Model for Compositional Non-Isothermal Multiphase Flow in Porous Media and Multiphysics Approaches for Two-Phase Flow.* Ph.D. thesis, Universität Stuttgart.

J. Fritz, B. Flemisch, and R. Helmig:, *Decoupled and multiphysics models for non-isothermal compositional two-phase flow in porous media. International Journal of Numerical Analysis & Modeling*, 9, 1 (2012), 17–28.

G. Futter (2012). *Investigation of the influences of different refinement approaches in the modelling of multiphase flow in porous media.* Master's thesis (Diplomarbeit), University of Stuttgart.

S. Geiger, T. Driesner, C. A. Heinrich, and S. K. Matthai, *Multiphase thermohaline convection in the earth´s crust: I. a new finite element - finite volume solution technique combined with a new equation of state for $NaCl$-H_2O. Transport in Porous Media*, 63 (2006)(3), 399–434–.

M. G. Gerritsen and L. J. Durlofsky, *Modeling fluid flow in oil reservoirs. Annu. Rev. Fluid Mech.*, 37 (2005), 211–238.

A. Grant and L. Sorey, *The Compressibility and Hydraulic Diffusivity of a Water-Steam Flow. Water Resources Research*, 15 (1979)(3), 684–686.

C. P. Green and J. Ennis-King, *Spatial grid correction for short-term numerical simulation results of carbon dioxide dissolution in saline aquifers. Computational Geosciences*, 16 (2012), 1153–1161.

D. Han, D. Han, C. Yan, and L. Peng (1987). *A more flexible approach of dynamic local grid refinement for reservoir modeling.* SPE Symposium on Reservoir Simulation, San Antonio, Texas.

J. Haukås, I. Aavatsmark, M. Espedal, and E. Reiso, *A comparison of two different impsat models in compositional simulation. SPE Journal*, 12 (2007)(1), pp. 145–151.

Z. Heinemann, G. Gerken, and G. von Hantelmann (1983). *Using local grid refinement in a multiple-application reservoir simulator.* In *SPE Reservoir Simulation Symposium, 15-18 November 1983, San Francisco, California.*

R. Helmig (1997). *Multiphase Flow and Transport Processes in the Subsurface.* Springer Verlag.

R. Helmig, B. Faigle, B. Flemisch, and M. Wolff, *Efficient modelling of flow and transport in porous media using multi- physics and multi-scale approaches. Handbook of geomathematics*, (2013). (accepted).

R. Helmig, C. Miller, H. Jakobs, H. Class, M. Hilpert, C. Kees, and J. Niessner (2006). *Multiphase flow and transport modeling in heterogeneous porous media.* In A. Bucchianico, R. Mattheij, and M. Peletier, editors, *Mathematics in Industry*, volume 8, pages 449–488–. Springer Berlin Heidelberg.

R. Helmig, J. Niessner, B. Flemisch, M. Wolff, and J. Fritz, *Efficient modelling of flow and transport in porous media using multi- physics and multi-scale approaches. Handbook of geomathematics*, 1 (2010), 417–457.

R. C. Hornung and J. A. Trangenstein, *Adaptive mesh refinement and multilevel iteration for flow in porous media. Journal of Computational Physics*, 136 (1997), 522–545.

M. K. Hubbert, *Darcy's law and the field equations of the flow of underground fluids. Petroleum Transactions, AIME,*, 207 (1956), 222–239.

IAPWS (1997). *Revised release on the iapws industrial formulation 1997 for the thermodynamic properties of water and steam.* `http://www.iapws.org/IF97-Rev.pdf`. (The International Association for the Properties of Water and Steam).

J. Jaffré and A. Sboui, *Henry' law and gas phase disappearance. Transport in Porous Media*, 82 (2010)(3), 521–526.

M. Jamal, S. Geiger, C. Enemanna, M. A. Elfeel, and D. Arnold (2013). *Effect of DFN Upscaling on History Matching and Prediction of Naturally Fractured Reservoirs.* In *75th EAGE Conference & Exhibition incorporating SPE EUROPEC.* Society of Petroleum Engineers, London, United Kingdom.

M. E. Jarle Haukas, Ivar Aavatsmark and E. Reisoa (2005). *Exact volume balance versus exact mass balance in compositional reservoir simulation.* Centre for Integrated Petroleum Research (CIPR), University of Bergen, Norway.

Y. K. Kharaka, D. R. Cole, S. D. Hovorka, W. D. Gunter, K. G. Knauss, and B. M. Freifeld, *Gas-water-rock interactions in Frio Formation following CO_2 injection: Implications for the storage of greenhouse gases in sedimentary basins. Geology*, 34 (2006)(7), 577–580.

S. Khattri and I. Aavatsmark, *Numerical convergence on adaptive grids for control volume methods. Numerical Methods for Partial Differential Equations*, 24 (2008)(2), 465–475.

S. K. Khattri, G. E. Fladmark, and H. Dahle (2007). *Control volume finite difference on adaptive meshes.* In O. Widlund and D. Keyes, editors, *Lecture Notes in Computational Science and Engineering*, volume 55, pages 627–633–. Springer Berlin Heidelberg.

W. Klieber and B. Riviere, *Adaptive simulations of two-phase flow by discontinuous galerkin methods. Computer Methods in Applied Mechanics and Engineering*, 196 (2006), 404–419.

R. Klöfkorn, D. Kräner, and M. Ohlberger, *Local adaptive methods for convection dominated problems. International Journal for Numerical Methods in Fluids*, 40 (2002)(1-2), 79 – 91.

D. Kräner and M. Ohlberger, *A posteriori error estimates for upwind finite volume schemes for nonlinear conservation laws in multi dimensions. Mathematics of Computation*, 69 (2000), 25 – 39.

A. Lauser, C. Hager, R. Helmig, and B. Wohlmuth, *A new approach for phase transitions in miscible multi-phase flow in porous media. Advances in Water Resources*, 34 (2011)(8), 957–966.

G. Lavie and A. M. Kamp (2011). *An evaluation of criteria for dynamic gridding during reservoir simulation of water flooding and solvent injection.* In *SPE Reservoir Simulation Symposium*. Society of Petroleum Engineers, The Woodlands, Texas, USA.

B. Lu and M. F. Wheeler, *Iterative coupling reservoir simulation on high performance computers. Petroleum Science*, 6 (2009)(1), 43–50.

J. Lu, Y. K. Kharaka, J. J. Thordsen, J. Horita, A. Karamalidis, and C. Griffith, *Co2-rock-brine interactions in lower tuscaloosa formation at cranfield co2 sequestration site, mississippi, u.s.a. Chemical Geology*, 291 (2012), p. 269–277.

E. Marchand, T. Müller, and P. Knabner, *Fully coupled generalized hybrid-mixed finite element approximation of two-phase two-component flow in porous media. part i: formulation and properties of the mathematical model. Computational Geosciences*, 17 (2013)(2), 431–442.

S. Mehl and M. C. Hill, *Development and evaluation of a local grid refinement method for block-centered finite-difference groundwater models using shared nodes. Advances in Water Resources*, 25 (2002)(5), 497–511.

S. Mehl and M. C. Hill, *Three-dimensional local grid refinement for block-centered finite-difference groundwater models using iteratively coupled shared nodes: a new method of interpolation and analysis of errors. Advances in Water Resources*, 27 (2004)(9), 899–912.

M. L. Michelsen and J. M. Mollerup (2007). *Thermodynamic Models: Fundamentals & Computational Aspects.* Tie-Line Publications.

C. T. Miller, G. Christakos, P. T. Imhoff, J. F. McBride, J. A. Pedit, and J. A. Trangenstein, *Multiphase flow and transport modeling in heterogeneous porous media: challenges and approaches. Advances in Water Resources*, 21 (1998)(2), 77–120.

J. Moortgat, S. Sun, and A. Firoozabadi, *Compositional modeling of three-phase flow with gravity using higher-order finite element methods. Water Resour. Res.*, 47 (2011)(5), W05511–.

H. Morel-Seytoux (1973). *Systematic treatment of infiltration with application: Completion report. OWRR Project no. B-070 Colorado, period July 1, 1971 - June 30, 1973.* Environmental Resources Center, Colorado State University. Submitted to Office of Water Resources Research, United States.

I. Mrosovsky and R. Ridings, *Two-dimensional radial treatment of wells within a three-dimensional reservoir model. Society of Petroleum Engineers Journal*, 14 (1974)(2), 127–138.

R. Neumann, P. Bastian, and O. Ippisch, *Modeling and simulation of two-phase two-component flow with disappearing nonwetting phase. Computational Geosciences*, 17 (2013)(1), 139–149.

J. Nilsson, M. G. Gerritsen, and R. Younis (2005). *An adaptive, high-resolution simulation for steam-injection processes.* In *SPE Western Regional Meeting.* Society of Petroleum Engineers, Irvine, California.

J. Nordbotten, B. Flemisch, S. Gasda, H. Nilsen, Y. Fan, G. Pickup, B. Wiese, M. Celia, H. Dahle, G. Eigestad, and K. Pruess, *Uncertainties in practical simulation of CO_2 storage. International Journal of Greenhouse Gas Control*, 9 (2012)(0), 234–242.

J. M. Nordbotten and M. A. Celia (2012). *Geological storage of CO_2.* Wiley, Hoboken, NJ [u.a.].

J. M. Nordbotten, M. A. Celia, H. K. Dahle, and S. M. Hassanizadeh, *On the definition of macroscale pressure for multiphase flow in porous media. Water Resour. Res.*, 44 (2008)(6), W06S02–.

G. S. H. Pau, J. B. Bell, A. S. Almgren, K. M. Fagnan, and M. J. Lijewski, *An adaptive mesh refinement algorithm for compressible two-phase flow in porous media. Computational Geosciences*, 16 (2012)(3), 577–592.

G. S. H. Pau, J. B. Bell, K. Pruess, A. S. Almgren, M. J. Lijewski, and K. Zhang, *High resolution simulation and characterization of density-driven flow in co2 storage in saline aquifers. Advances in Water Resources*, 33(4) (2010), 443–455.

M. Paul (2003). *Simulation of Two-Phase Flow Processes in Heterogeneous Porous Media with Adaptive Methods*. Ph.D. thesis, Universität Stuttgart.

D. Peaceman, *Interpretation of well-block pressures in numerical reservoir simulation. Society of Petroleum Engineers Journal*, 18 (1978)(3), 183–194.

E. J. Pebesma and C. G. Wesseling, *Gstat: a program for geostatistical modelling, prediction and simulation. Computers & Geosciences*, 24 (1998)(1), 17–31.

M. Peszyńska (2003). *Multiphysics coupling of three-phase and two-phase models of flow in porous media*. In W. Wendland and M. Efendiev, editors, *Lecture Notes in Applied and Computational Mechanics*, volume 12, pages 311–316–. Springer Berlin Heidelberg.

M. Peszyńska, Q. Lu, and M. F. Wheeler (2000). *Multiphysics coupling of codes*. In *Computational Methods in Water Resources*, pages 175–182.

G. F. Pinder and M. A. Celia (2006). *Subsurface hydrology*. Wiley-Interscience, Hoboken, NJ.

B. E. Poling, J. M. Prausnitz, and J. P. O'Connell (2001). *The properties of gases and liquids*. McGraw-Hill, New York [u.a.].

H. H. Rachford Jr and J. D. Rice, *Procedure for Use of Electronic Digital Computers in Calculating Flash Vaporization Hydrocarbon Equilibrium. Journal of Petroleum Technology*, 4 (1952).

J. B. Randolph, M. O. Saar, and J. Bielicki, *Geothermal energy production at geologic CO_2 sequestration sites: Impact of thermal drawdown on reservoir pressure. Energy Procedia*, 37 (2013)(0), 6625–6635.

R. Reid, J. Prausnitz, and B. Poling (1987). *The Properties of Gases and Liquids*. McGraw-Hill Inc., 4 edition.

P. Renard and G. De Marsily, *Calculating equivalent permeability: a review. Advances in Water Resources*, 20 (1997)(5), 253–278.

J. Rodrigues and F. Dickstein, *A multigrid procedure for local grid refinement in oil reservoir simulation. SPE Advanced Technology Series*, 4 (1996)(1), 157–164.

H. Römpp, J. Falbe, and E. Amelingmeier (1999). *Römpp - Lexikon Chemie*. Thieme Verlag, Stuttgart.

A. Salehi, H. Tchelepi, and D. Voskov (2013). *Thermodynamically consistent transport coefficients for upscaling of compositional processes*. In *2013 SPE Reservoir Simulation Symposium*. Society of Petroleum Engineers, The Woodlands, TX, USA.

H. Salimi and K.-H. Wolf, *Integration of heat-energy recovery and carbon sequestration. International Journal of Greenhouse Gas Control*, 6 (2012)(0), 56–68.

R. Sander (1999). *Compilation of Henry's law constants for inorganic and organic species of potential importance in environmental chemistry.* Mainz : Max-Planck Institute of Chemistry, Air Chemistry Dept.

F. Schäfer, L. Walter, H. Class, and C. Müller, *The regional pressure impact of CO_2 storage: a showcase study from the North German Basin. Environmental Earth Sciences*, 65 (2012)(7), 2037–2049.

M. Sinsbeck (2011). *Adaptive grid refinement for two phase flow in porous media.* Master's thesis (Diplomarbeit), Institut für Wasserbau, Universität Stuttgart.

B. Sleep and J. Sykes, *Computational Simulation of Groundwater Contamination by Organic Compounds 1. Model Development and Verification. Water Resources Research*, 29 (1993)(6), 1697–1708.

R. Span and W. Wagner, *A New Equation of State for Carbon Dioxide Covering the Fluid Region from the Triple–Point Temperature to 1100 K at Pressures up to 800 MPa. J. Phys. Chem. Ref. Data*, 25(6) (1996), 1509–1596.

H. Stone (1991). *Rigorous black oil pseudo functions.* In *SPE Symposium on Reservoir Simulation*. 1991, Anaheim, California.

H. Stone and A. G. Jr., *Analysis of gas-cap or dissolved-gas drive reservoirs. SPE Journal*, 1 (1961)(2).

M. Sun and K. Takayama, *Error localization in solution-adaptive grid methods. Journal of Computational Physics*, 190 (2003)(1), 346 – 350.

G. Thomas and D. Thurnau, *Reservoir simulation using an adaptive implicit method. Society of Petroleum Engineers Journal*, 23 (1983)(5), 759–768.

S. Thomas and M. Wheeler, *Enhanced velocity mixed finite element methods for modeling coupled flow and transport on non-matching multiblock grids. Computational Geosciences*, 15 (2011), 605–625. 10.1007/s10596-011-9227-5.

J. Trangenstein and J. Bell, *Mathematical structure of compositional reservoir simulation. SIAM J. Sci. Stat. Comput.*, (1989), 817–845.

J. A. Trangenstein, *Multi-scale iterative techniques and adaptive mesh refinement for flow in porous media. Advances in Water Resources*, 25 (2002)(8-12), 1175–1213.

S. Tveit and I. Aavatsmark, *Errors in the upstream mobility scheme for countercurrent two-phase flow in heterogeneous porous media. Computational Geosciences*, 16 (2012)(3), 809–825.

S. A. Vakili-Ghahani and J. D. Jansen, *A system-theoretical approach to selective grid coarsening of reservoir models. Computational Geosciences*, 16 (2012), 159–176.

D. E. A. van Odyck, J. B. Bell, F. Monmont, and N. Nikiforakis (2008). *The mathematical structure of multiphase thermal models of flow in porous media.* In *Proceedings of the Royal Society A: Mathematical, Physical and Engineering Sciences*, volume 465 of *2102*, pages 523–549.

R. Verfürth (1996). *A review of a posteriori error estimation and adaptive mesh refinement techniques.* Wiley-Teubner, Chichester.

M. Vohralik, *Residual flux-based a posteriori error estimates for finite volume discretizations of inhomogeneous, anisotropic, and convection-dominated problems. Numer. Math*, 111 (2008), 121–158.

W. Watts, J., *A compositional formulation of the pressure and saturation equations. SPE Reservoir Engineering*, 1 (1986)(3), 243–252.

S. W. Webb and J. M. Phelan, *Effect of soil layering on napl removal behavior in soil-heated vapor extraction. Journal of Contaminant Hydrology*, 27 (1997), 285–308.

J. A. Wheeler, M. F. Wheeler, and I. Yotov, *Enhanced velocity mixed finite element methods for flow in multiblock domains. Computational Geosciences*, 6 (2002), 315–332. Springerlink:10.1023/A:1021270509932.

M. Wheeler, T. Arbogast, S. Bryant, J. Eaton, Q. Lu, M. Peszynska, and I. Yotov, *A Parallel Multiblock/Multidomain Approach for Reservoir Simulation. SPE 51884*, (1999).

M. F. Wheeler and M. Peszyńska, *Computational engineering and science methodologies for modeling and simulation of subsurface applications. Advances in Water Resources*, 25 (2002)(12), 1147–1173.

M. Wolff (2013). *Multi-Scale Modeling of Two-Phase Flow in Porous Media Including Capillary Pressure Effects*. Ph.D. thesis, Universität Stuttgart.

M. Wolff, Y. Cao, B. Flemisch, R. Helmig, and B. Wohlmuth (2013a). *Multi-point flux approximation L-method in 3D: Numerical convergence and application to two-phase flow through porous media*. In P. Bastian, J. Kraus, R. Scheichl, and M. Wheeler, editors, *Radon series on computational and applied mathematics 12*. De gruyter.

M. Wolff, B. Flemisch, and R. Helmig, *An adaptive multi-scale approach for modeling two-phase flow in porous media including capillary pressure. Water Resources Research*, (2013b). Submitted.

M. Wolff, B. Flemisch, R. Helmig, and I. Aavatsmark, *Treatment of tensorial relative permeabilities with multipoint flux approximation. International Journal of Numerical Analysis & Modeling*, 9 (2012)(3), 724–744.

R. Wooding and H. J. Morel-Seytoux, *Multiphase fluid flow through porous media. Annual review of fluid mechanics*, 8 (1976)(1), 233–274.

Lebenslauf

Persönliche Daten

Name:	Benjamin Faigle
Geburt:	27.09.1982 in Mühlacker
Staatsangehörigkeit:	deutsch

Ausbildung

1994-2002:	Friedrich-Abel Gymnasium, Vaihingen-Enz
2003-2009:	Studium der Umweltschutztechnik an der Universität Stuttgart
2007:	Studium an der Deakin University, Australien
seit 2009:	Mitglied im Internationalen Graduiertenkolleg NUPUS (Nonlinearities and Upscaling in Porous Media), zur Diplomarbeit sowie als Doktorand

Berufstätigkeit

seit 2009	Wissenschaftlicher Mitarbeiter am Institut für Wasser- und Umweltsystemmodellierung der Universität Stuttgart, Lehrstuhl für Hydromechanik und Hydrosystemmodellierung

Institut für Wasser- und Umweltsystemmodellierung
Universität Stuttgart

Pfaffenwaldring 61
70569 Stuttgart (Vaihingen)
Telefon (0711) 685 - 64717/64749/64752/64679
Telefax (0711) 685 - 67020 o. 64746 o. 64681
E-Mail: iws@iws.uni-stuttgart.de
http://www.iws.uni-stuttgart.de

Verzeichnis der Mitteilungshefte

5 Plate, Erich: *Beitrag zur Bestimmung der Windgeschwindigkeitsverteilung in der durch eine Wand gestörten bodennahen Luftschicht*,
und
Röhnisch, Arthur; Marotz, Günter: *Neue Baustoffe und Bauausführungen für den Schutz der Böschungen und der Sohle von Kanälen, Flüssen und Häfen; Gestehungskosten und jeweilige Vorteile*, sowie Unny, T.E.: *Schwingungsuntersuchungen am Kegelstrahlschieber*, 1967

6 Seiler, Erich: *Die Ermittlung des Anlagenwertes der bundeseigenen Binnenschiffahrtsstraßen und Talsperren und des Anteils der Binnenschiffahrt an diesem Wert*, 1967

7 *Sonderheft anläßlich des 65. Geburtstages von Prof. Arthur Röhnisch mit Beiträgen von* Benk, Dieter; Breitling, J.; Gurr, Siegfried; Haberhauer, Robert; Honekamp, Hermann; Kuz, Klaus Dieter; Marotz, Günter; Mayer-Vorfelder, Hans-Jörg; Miller, Rudolf; Plate, Erich J.; Radomski, Helge; Schwarz, Helmut; Vollmer, Ernst; Wildenhahn, Eberhard; 1967

8 Jumikis, Alfred: *Beitrag zur experimentellen Untersuchung des Wassernachschubs in einem gefrierenden Boden und die Beurteilung der Ergebnisse*, 1968

9 Marotz, Günter: *Technische Grundlagen einer Wasserspeicherung im natürlichen Untergrund*, 1968

10 Radomski, Helge: *Untersuchungen über den Einfluß der Querschnittsform wellenförmiger Spundwände auf die statischen und rammtechnischen Eigenschaften*, 1968

11 Schwarz, Helmut: *Die Grenztragfähigkeit des Baugrundes bei Einwirkung vertikal gezogener Ankerplatten als zweidimensionales Bruchproblem*, 1969

12 Erbel, Klaus: *Ein Beitrag zur Untersuchung der Metamorphose von Mittelgebirgsschneedecken unter besonderer Berücksichtigung eines Verfahrens zur Bestimmung der thermischen Schneequalität*, 1969

13 Westhaus, Karl-Heinz: *Der Strukturwandel in der Binnenschiffahrt und sein Einfluß auf den Ausbau der Binnenschiffskanäle*, 1969

14 Mayer-Vorfelder, Hans-Jörg: *Ein Beitrag zur Berechnung des Erdwiderstandes unter Ansatz der logarithmischen Spirale als Gleitflächenfunktion*, 1970

15 Schulz, Manfred: *Berechnung des räumlichen Erddruckes auf die Wandung kreiszylindrischer Körper*, 1970

16 Mobasseri, Manoutschehr: *Die Rippenstützmauer. Konstruktion und Grenzen ihrer Standsicherheit*, 1970

17 Benk, Dieter: *Ein Beitrag zum Betrieb und zur Bemessung von Hochwasserrückhaltebecken*, 1970

18 Gàl, Attila: *Bestimmung der mitschwingenden Wassermasse bei überströmten Fischbauchklappen mit kreiszylindrischem Staublech*, 1971, vergriffen

19 Kuz, Klaus Dieter: *Ein Beitrag zur Frage des Einsetzens von Kavitationserscheinungen in einer Düsenströmung bei Berücksichtigung der im Wasser gelösten Gase*, 1971, vergriffen

20 Schaak, Hartmut: *Verteilleitungen von Wasserkraftanlagen*, 1971

21 *Sonderheft zur Eröffnung der neuen Versuchsanstalt des Instituts für Wasserbau der Universität Stuttgart mit Beiträgen von* Brombach, Hansjörg; Dirksen, Wolfram; Gàl, Attila; Gerlach, Reinhard; Giesecke, Jürgen; Holthoff, Franz-Josef; Kuz, Klaus Dieter; Marotz, Günter; Minor, Hans-Erwin; Petrikat, Kurt; Röhnisch, Arthur; Rueff, Helge; Schwarz, Helmut; Vollmer, Ernst; Wildenhahn, Eberhard; 1972

22 Wang, Chung-su: *Ein Beitrag zur Berechnung der Schwingungen an Kegelstrahlschiebern*, 1972

23 Mayer-Vorfelder, Hans-Jörg: *Erdwiderstandsbeiwerte nach dem Ohde-Variationsverfahren*, 1972

24 Minor, Hans-Erwin: *Beitrag zur Bestimmung der Schwingungsanfachungsfunktionen überströmter Stauklappen*, 1972, vergriffen

25 Brombach, Hansjörg: *Untersuchung strömungsmechanischer Elemente (Fluidik) und die Möglichkeit der Anwendung von Wirbelkammerelementen im Wasserbau*, 1972, vergriffen

26 Wildenhahn, Eberhard: *Beitrag zur Berechnung von Horizontalfilterbrunnen*, 1972

27 Steinlein, Helmut: *Die Eliminierung der Schwebstoffe aus Flußwasser zum Zweck der unterirdischen Wasserspeicherung, gezeigt am Beispiel der Iller*, 1972

28 Holthoff, Franz Josef: *Die Überwindung großer Hubhöhen in der Binnenschiffahrt durch Schwimmerhebewerke*, 1973

29 Röder, Karl: *Einwirkungen aus Baugrundbewegungen auf trog- und kastenförmige Konstruktionen des Wasser- und Tunnelbaues*, 1973

30 Kretschmer, Heinz: *Die Bemessung von Bogenstaumauern in Abhängigkeit von der Talform*, 1973

31 Honekamp, Hermann: *Beitrag zur Berechnung der Montage von Unterwasserpipelines*, 1973

32 Giesecke, Jürgen: *Die Wirbelkammertriode als neuartiges Steuerorgan im Wasserbau*, und Brombach, Hansjörg: *Entwicklung, Bauformen, Wirkungsweise und Steuereigenschaften von Wirbelkammerverstärkern*, 1974

33 Rueff, Helge: *Untersuchung der schwingungserregenden Kräfte an zwei hintereinander angeordneten Tiefschützen unter besonderer Berücksichtigung von Kavitation*, 1974

34 Röhnisch, Arthur: *Einpreßversuche mit Zementmörtel für Spannbeton - Vergleich der Ergebnisse von Modellversuchen mit Ausführungen in Hüllwellrohren*, 1975

35 *Sonderheft anläßlich des 65. Geburtstages von Prof. Dr.-Ing. Kurt Petrikat mit Beiträgen von*: Brombach, Hansjörg; Erbel, Klaus; Flinspach, Dieter; Fischer jr., Richard; Gàl, Attila; Gerlach, Reinhard; Giesecke, Jürgen; Haberhauer, Robert; Hafner Edzard; Hausenblas, Bernhard; Horlacher, Hans-Burkhard; Hutarew, Andreas; Knoll, Manfred; Krummet, Ralph; Marotz, Günter; Merkle, Theodor; Miller, Christoph; Minor, Hans-Erwin; Neumayer, Hans; Rao, Syamala; Rath, Paul; Rueff, Helge; Ruppert, Jürgen; Schwarz, Wolfgang; Topal-Gökceli, Mehmet; Vollmer, Ernst; Wang, Chung-su; Weber, Hans-Georg; 1975

36 Berger, Jochum: *Beitrag zur Berechnung des Spannungszustandes in rotationssymmetrisch belasteten Kugelschalen veränderlicher Wandstärke unter Gas- und Flüssigkeitsdruck durch Integration schwach singulärer Differentialgleichungen*, 1975

37 Dirksen, Wolfram: *Berechnung instationärer Abflußvorgänge in gestauten Gerinnen mittels Differenzenverfahren und die Anwendung auf Hochwasserrückhaltebecken*, 1976

38 Horlacher, Hans-Burkhard: *Berechnung instationärer Temperatur- und Wärmespannungsfelder in langen mehrschichtigen Hohlzylindern*, 1976

39 Hafner, Edzard: *Untersuchung der hydrodynamischen Kräfte auf Baukörper im Tiefwasserbereich des Meeres*, 1977, ISBN 3-921694-39-6

40 Ruppert, Jürgen: *Über den Axialwirbelkammerverstärker für den Einsatz im Wasserbau*, 1977, ISBN 3-921694-40-X

41 Hutarew, Andreas: *Beitrag zur Beeinflußbarkeit des Sauerstoffgehalts in Fließgewässern an Abstürzen und Wehren*, 1977, ISBN 3-921694-41-8, vergriffen

42 Miller, Christoph: *Ein Beitrag zur Bestimmung der schwingungserregenden Kräfte an unterströmten Wehren*, 1977, ISBN 3-921694-42-6

43 Schwarz, Wolfgang: *Druckstoßberechnung unter Berücksichtigung der Radial- und Längsverschiebungen der Rohrwandung*, 1978, ISBN 3-921694-43-4

44 Kinzelbach, Wolfgang: *Numerische Untersuchungen über den optimalen Einsatz variabler Kühlsysteme einer Kraftwerkskette am Beispiel Oberrhein*, 1978, ISBN 3-921694-44-2

45 Barczewski, Baldur: *Neue Meßmethoden für Wasser-Luftgemische und deren Anwendung auf zweiphasige Auftriebsstrahlen*, 1979, ISBN 3-921694-45-0

46 Neumayer, Hans: *Untersuchung der Strömungsvorgänge in radialen Wirbelkammerverstärkern*, 1979, ISBN 3-921694-46-9

47 Elalfy, Youssef-Elhassan: *Untersuchung der Strömungsvorgänge in Wirbelkammerdioden und -drosseln*, 1979, ISBN 3-921694-47-7

48 Brombach, Hansjörg: *Automatisierung der Bewirtschaftung von Wasserspeichern*, 1981, ISBN 3-921694-48-5

49 Geldner, Peter: *Deterministische und stochastische Methoden zur Bestimmung der Selbstdichtung von Gewässern*, 1981, ISBN 3-921694-49-3, vergriffen

50 Mehlhorn, Hans: *Temperaturveränderungen im Grundwasser durch Brauchwassereinleitungen*, 1982, ISBN 3-921694-50-7, vergriffen

51 Hafner, Edzard: *Rohrleitungen und Behälter im Meer*, 1983, ISBN 3-921694-51-5

52 Rinnert, Bernd: *Hydrodynamische Dispersion in porösen Medien: Einfluß von Dichteunterschieden auf die Vertikalvermischung in horizontaler Strömung*, 1983, ISBN 3-921694-52-3, vergriffen

53 Lindner, Wulf: *Steuerung von Grundwasserentnahmen unter Einhaltung ökologischer Kriterien*, 1983, ISBN 3-921694-53-1, vergriffen

54 Herr, Michael; Herzer, Jörg; Kinzelbach, Wolfgang; Kobus, Helmut; Rinnert, Bernd: *Methoden zur rechnerischen Erfassung und hydraulischen Sanierung von Grundwasserkontaminationen*, 1983, ISBN 3-921694-54-X

55 Schmitt, Paul: *Wege zur Automatisierung der Niederschlagsermittlung*, 1984, ISBN 3-921694-55-8, vergriffen

56 Müller, Peter: *Transport und selektive Sedimentation von Schwebstoffen bei gestautem Abfluß*, 1985, ISBN 3-921694-56-6

57 El-Qawasmeh, Fuad: *Möglichkeiten und Grenzen der Tropfbewässerung unter besonderer Berücksichtigung der Verstopfungsanfälligkeit der Tropfelemente*, 1985, ISBN 3-921694-57-4, vergriffen

58 Kirchenbaur, Klaus: *Mikroprozessorgesteuerte Erfassung instationärer Druckfelder am Beispiel seegangsbelasteter Baukörper*, 1985, ISBN 3-921694-58-2

59 Kobus, Helmut (Hrsg.): *Modellierung des großräumigen Wärme- und Schadstofftransports im Grundwasser*, Tätigkeitsbericht 1984/85 (DFG-Forschergruppe an den Universitäten Hohenheim, Karlsruhe und Stuttgart), 1985, ISBN 3-921694-59-0, vergriffen

60 Spitz, Karlheinz: *Dispersion in porösen Medien: Einfluß von Inhomogenitäten und Dichteunterschieden*, 1985, ISBN 3-921694-60-4, vergriffen

61 Kobus, Helmut: *An Introduction to Air-Water Flows in Hydraulics*, 1985, ISBN 3-921694-61-2

62 Kaleris, Vassilios: *Erfassung des Austausches von Oberflächen- und Grundwasser in horizontalebenen Grundwassermodellen*, 1986, ISBN 3-921694-62-0

63 Herr, Michael: *Grundlagen der hydraulischen Sanierung verunreinigter Porengrundwasserleiter*, 1987, ISBN 3-921694-63-9

64 Marx, Walter: *Berechnung von Temperatur und Spannung in Massenbeton infolge Hydratation*, 1987, ISBN 3-921694-64-7

65 Koschitzky, Hans-Peter: *Dimensionierungskonzept für Sohlbelüfter in Schußrinnen zur Vermeidung von Kavitationsschäden*, 1987, ISBN 3-921694-65-5

66 Kobus, Helmut (Hrsg.): *Modellierung des großräumigen Wärme- und Schadstofftransports im Grundwasser*, Tätigkeitsbericht 1986/87 (DFG-Forschergruppe an den Universitäten Hohenheim, Karlsruhe und Stuttgart) 1987, ISBN 3-921694-66-3

67 Söll, Thomas: *Berechnungsverfahren zur Abschätzung anthropogener Temperaturanomalien im Grundwasser*, 1988, ISBN 3-921694-67-1

68 Dittrich, Andreas; Westrich, Bernd: *Bodenseeufererosion, Bestandsaufnahme und Bewertung*, 1988, ISBN 3-921694-68-X, vergriffen

69 Huwe, Bernd; van der Ploeg, Rienk R.: *Modelle zur Simulation des Stickstoffhaushaltes von Standorten mit unterschiedlicher landwirtschaftlicher Nutzung*, 1988, ISBN 3-921694-69-8, vergriffen

70 Stephan, Karl: *Integration elliptischer Funktionen*, 1988, ISBN 3-921694-70-1

71 Kobus, Helmut; Zilliox, Lothaire (Hrsg.): *Nitratbelastung des Grundwassers, Auswirkungen der Landwirtschaft auf die Grundwasser- und Rohwasserbeschaffenheit und Maßnahmen zum Schutz des Grundwassers*. Vorträge des deutsch-französischen Kolloquiums am 6. Oktober 1988, Universitäten Stuttgart und Louis Pasteur Strasbourg (Vorträge in deutsch oder französisch, Kurzfassungen zweisprachig), 1988, ISBN 3-921694-71-X

72 Soyeaux, Renald: *Unterströmung von Stauanlagen auf klüftigem Untergrund unter Berücksichtigung laminarer und turbulenter Fließzustände*,1991, ISBN 3-921694-72-8

73 Kohane, Roberto: *Berechnungsmethoden für Hochwasserabfluß in Fließgewässern mit überströmten Vorländern*, 1991, ISBN 3-921694-73-6

74 Hassinger, Reinhard: *Beitrag zur Hydraulik und Bemessung von Blocksteinrampen in flexibler Bauweise*, 1991, ISBN 3-921694-74-4, vergriffen

75 Schäfer, Gerhard: *Einfluß von Schichtenstrukturen und lokalen Einlagerungen auf die Längsdispersion in Porengrundwasserleitern*, 1991, ISBN 3-921694-75-2

76 Giesecke, Jürgen: *Vorträge, Wasserwirtschaft in stark besiedelten Regionen; Umweltforschung mit Schwerpunkt Wasserwirtschaft*, 1991, ISBN 3-921694-76-0

77 Huwe, Bernd: *Deterministische und stochastische Ansätze zur Modellierung des Stickstoffhaushalts landwirtschaftlich genutzter Flächen auf unterschiedlichem Skalenniveau*, 1992, ISBN 3-921694-77-9, vergriffen

78 Rommel, Michael: *Verwendung von Kluftdaten zur realitätsnahen Generierung von Kluftnetzen mit anschließender laminar-turbulenter Strömungsberechnung*, 1993, ISBN 3-92 1694-78-7

79 Marschall, Paul: *Die Ermittlung lokaler Stofffrachten im Grundwasser mit Hilfe von Einbohrloch-Meßverfahren*, 1993, ISBN 3-921694-79-5, vergriffen

80 Ptak, Thomas: *Stofftransport in heterogenen Porenaquiferen: Felduntersuchungen und stochastische Modellierung*, 1993, ISBN 3-921694-80-9, vergriffen

81 Haakh, Frieder: *Transientes Strömungsverhalten in Wirbelkammern,* 1993, ISBN 3-921694-81-7

82 Kobus, Helmut; Cirpka, Olaf; Barczewski, Baldur; Koschitzky, Hans-Peter: *Versucheinrichtung zur Grundwasser und Altlastensanierung VEGAS, Konzeption und Programmrahmen*, 1993, ISBN 3-921694-82-5

83 Zang, Weidong: *Optimaler Echtzeit-Betrieb eines Speichers mit aktueller Abflußregenerierung*, 1994, ISBN 3-921694-83-3, vergriffen

84 Franke, Hans-Jörg: *Stochastische Modellierung eines flächenhaften Stoffeintrages und Transports in Grundwasser am Beispiel der Pflanzenschutzmittelproblematik*, 1995, ISBN 3-921694-84-1

85 Lang, Ulrich: *Simulation regionaler Strömungs- und Transportvorgänge in Karstaquiferen mit Hilfe des Doppelkontinuum-Ansatzes: Methodenentwicklung und Parameteridentifikation*, 1995, ISBN 3-921694-85-X, vergriffen

86 Helmig, Rainer: *Einführung in die Numerischen Methoden der Hydromechanik*, 1996, ISBN 3-921694-86-8, vergriffen

87 Cirpka, Olaf: *CONTRACT: A Numerical Tool for Contaminant Transport and Chemical Transformations - Theory and Program Documentation* -, 1996, ISBN 3-921694-87-6

88 Haberlandt, Uwe: *Stochastische Synthese und Regionalisierung des Niederschlages für Schmutzfrachtberechnungen*, 1996, ISBN 3-921694-88-4

89 Croisé, Jean: *Extraktion von flüchtigen Chemikalien aus natürlichen Lockergesteinen mittels erzwungener Luftströmung*, 1996, ISBN 3-921694-89-2, vergriffen

90 Jorde, Klaus: *Ökologisch begründete, dynamische Mindestwasserregelungen bei Ausleitungskraftwerken*, 1997, ISBN 3-921694-90-6, vergriffen

91 Helmig, Rainer: *Gekoppelte Strömungs- und Transportprozesse im Untergrund - Ein Beitrag zur Hydrosystemmodellierung*-, 1998, ISBN 3-921694-91-4, vergriffen

92 Emmert, Martin: *Numerische Modellierung nichtisothermer Gas-Wasser Systeme in porösen Medien,* 1997, ISBN 3-921694-92-2

93 Kern, Ulrich: *Transport von Schweb- und Schadstoffen in staugeregelten Fließgewässern am Beispiel des Neckars*, 1997, ISBN 3-921694-93-0, vergriffen

94 Förster, Georg: *Druckstoßdämpfung durch große Luftblasen in Hochpunkten von Rohrleitungen 1997*, ISBN 3-921694-94-9

95 Cirpka, Olaf: *Numerische Methoden zur Simulation des reaktiven Mehrkomponententransports im Grundwasser*, 1997, ISBN 3-921694-95-7, vergriffen

96 Färber, Arne: *Wärmetransport in der ungesättigten Bodenzone: Entwicklung einer thermischen In-situ-Sanierungstechnologie*, 1997, ISBN 3-921694-96-5

97 Betz, Christoph: *Wasserdampfdestillation von Schadstoffen im porösen Medium: Entwicklung einer thermischen In-situ-Sanierungstechnologie*, 1998, ISBN 3-921694-97-3

98 Xu, Yichun: *Numerical Modeling of Suspended Sediment Transport in Rivers*, 1998, ISBN 3-921694-98-1, vergriffen

99 Wüst, Wolfgang: *Geochemische Untersuchungen zur Sanierung CKW-kontaminierter Aquifere mit Fe(0)-Reaktionswänden,* 2000, ISBN 3-933761-02-2

100 Sheta, Hussam: *Simulation von Mehrphasenvorgängen in porösen Medien unter Einbeziehung von Hysterese-Effekten*, 2000, ISBN 3-933761-03-4

101 Ayros, Edwin: *Regionalisierung extremer Abflüsse auf der Grundlage statistischer Verfahren*, 2000, ISBN 3-933761-04-2, vergriffen

102 Huber, Ralf: *Compositional Multiphase Flow and Transport in Heterogeneous Porous Media*, 2000, ISBN 3-933761-05-0

103 Braun, Christopherus: *Ein Upscaling-Verfahren für Mehrphasenströmungen in porösen Medien*, 2000, ISBN 3-933761-06-9

104 Hofmann, Bernd: *Entwicklung eines rechnergestützten Managementsystems zur Beurteilung von Grundwasserschadensfällen*, 2000, ISBN 3-933761-07-7

105 Class, Holger: *Theorie und numerische Modellierung nichtisothermer Mehrphasenprozesse in NAPL-kontaminierten porösen Medien,* 2001, ISBN 3-933761-08-5

106 Schmidt, Reinhard: *Wasserdampf- und Heißluftinjektion zur thermischen Sanierung kontaminierter Standorte*, 2001, ISBN 3-933761-09-3

107 Josef, Reinhold:, *Schadstoffextraktion mit hydraulischen Sanierungsverfahren unter Anwendung von grenzflächenaktiven Stoffen*, 2001, ISBN 3-933761-10-7

108 Schneider, Matthias: *Habitat- und Abflussmodellierung für Fließgewässer mit unscharfen Berechnungsansätzen*, 2001, ISBN 3-933761-11-5

109 Rathgeb, Andreas: *Hydrodynamische Bemessungsgrundlagen für Lockerdeckwerke an überströmbaren Erddämmen*, 2001, ISBN 3-933761-12-3

110 Lang, Stefan: *Parallele numerische Simulation instätionärer Probleme mit adaptiven Methoden auf unstrukturierten Gittern*, 2001, ISBN 3-933761-13-1

111 Appt, Jochen; Stumpp Simone: *Die Bodensee-Messkampagne 2001, IWS/CWR Lake Constance Measurement Program 2001*, 2002, ISBN 3-933761-14-X

112 Heimerl, Stephan: *Systematische Beurteilung von Wasserkraftprojekten,* 2002, ISBN 3-933761-15-8, vergriffen

113 Iqbal, Amin: *On the Management and Salinity Control of Drip Irrigation,* 2002, ISBN 3-933761-16-6

114 Silberhorn-Hemminger, Annette: *Modellierung von Kluftaquifersystemen: Geostatistische Analyse und deterministisch-stochastische Kluftgenerierung,* 2002, ISBN 3-933761-17-4

115 Winkler, Angela: *Prozesse des Wärme- und Stofftransports bei der In-situ-Sanierung mit festen Wärmequellen,* 2003, ISBN 3-933761-18-2

116 Marx, Walter: *Wasserkraft, Bewässerung, Umwelt - Planungs- und Bewertungsschwerpunkte der Wasserbewirtschaftung,* 2003, ISBN 3-933761-19-0

117 Hinkelmann, Reinhard: *Efficient Numerical Methods and Information-Processing Techniques in Environment Water,* 2003, ISBN 3-933761-20-4

118 Samaniego-Eguiguren, Luis Eduardo: *Hydrological Consequences of Land Use / Land Cover and Climatic Changes in Mesoscale Catchments*, 2003, ISBN 3-933761-21-2

119 Neunhäuserer, Lina: *Diskretisierungsansätze zur Modellierung von Strömungs- und Transportprozessen in geklüftet-porösen Medien*, 2003, ISBN 3-933761-22-0

120 Paul, Maren: *Simulation of Two-Phase Flow in Heterogeneous Poros Media with Adaptive Methods*, 2003, ISBN 3-933761-23-9

121 Ehret, Uwe: *Rainfall and Flood Nowcasting in Small Catchments using Weather Radar*, 2003, ISBN 3-933761-24-7

122 Haag, Ingo: *Der Sauerstoffhaushalt staugeregelter Flüsse am Beispiel des Neckars - Analysen, Experimente, Simulationen -,* 2003, ISBN 3-933761-25-5

123 Appt, Jochen: *Analysis of Basin-Scale Internal Waves in Upper Lake Constance,* 2003, ISBN 3-933761-26-3

124 Hrsg.: Schrenk, Volker; Batereau, Katrin; Barczewski, Baldur; Weber, Karolin und Koschitzky, Hans-Peter: *Symposium Ressource Fläche und VEGAS - Statuskolloquium 2003, 30. September und 1. Oktober 2003,* 2003, ISBN 3-933761-27-1

125 Omar Khalil Ouda: *Optimisation of Agricultural Water Use: A Decision Support System for the Gaza Strip,* 2003, ISBN 3-933761-28-0

126 Batereau, Katrin: *Sensorbasierte Bodenluftmessung zur Vor-Ort-Erkundung von Schadensherden im Untergrund*, 2004, ISBN 3-933761-29-8

127 Witt, Oliver: *Erosionsstabilität von Gewässersedimenten mit Auswirkung auf den Stofftransport bei Hochwasser am Beispiel ausgewählter Stauhaltungen des Oberrheins*, 2004, ISBN 3-933761-30-1

128 Jakobs, Hartmut: *Simulation nicht-isothermer Gas-Wasser-Prozesse in komplexen Kluft-Matrix-Systemen*, 2004, ISBN 3-933761-31-X

129 Li, Chen-Chien: *Deterministisch-stochastisches Berechnungskonzept zur Beurteilung der Auswirkungen erosiver Hochwasserereignisse in Flussstauhaltungen,* 2004, ISBN 3-933761-32-8

130 Reichenberger, Volker; Helmig, Rainer; Jakobs, Hartmut; Bastian, Peter; Niessner, Jennifer: *Complex Gas-Water Processes in Discrete Fracture-Matrix Systems: Upscaling, Mass-Conservative Discretization and Efficient Multilevel Solution,* 2004, ISBN 3-933761-33-6

131 Hrsg.: Barczewski, Baldur; Koschitzky, Hans-Peter; Weber, Karolin; Wege, Ralf: *VEGAS - Statuskolloquium 2004,* Tagungsband zur Veranstaltung am 05. Oktober 2004 an der Universität Stuttgart, Campus Stuttgart-Vaihingen, 2004, ISBN 3-933761-34-4

132 Asie, Kemal Jabir: *Finite Volume Models for Multiphase Multicomponent Flow through Porous Media*. 2005, ISBN 3-933761-35-2

133 Jacoub, George: *Development of a 2-D Numerical Module for Particulate Contaminant Transport in Flood Retention Reservoirs and Impounded Rivers,* 2004, ISBN 3-933761-36-0

134 Nowak, Wolfgang: *Geostatistical Methods for the Identification of Flow and Transport Parameters in the Subsurface,* 2005, ISBN 3-933761-37-9

135 Süß, Mia: *Analysis of the influence of structures and boundaries on flow and transport processes in fractured porous media*, 2005, ISBN 3-933761-38-7

136 Jose, Surabhin Chackiath: *Experimental Investigations on Longitudinal Dispersive Mixing in Heterogeneous Aquifers,* 2005, ISBN: 3-933761-39-5

137 Filiz, Fulya: *Linking Large-Scale Meteorological Conditions to Floods in Mesoscale Catchments,* 2005, ISBN 3-933761-40-9

138 Qin, Minghao: *Wirklichkeitsnahe und recheneffiziente Ermittlung von Temperatur und Spannungen bei großen RCC-Staumauern*, 2005, ISBN 3-933761-41-7

139 Kobayashi, Kenichiro: *Optimization Methods for Multiphase Systems in the Subsurface - Application to Methane Migration in Coal Mining Areas*, 2005, ISBN 3-933761-42-5

140 Rahman, Md. Arifur: *Experimental Investigations on Transverse Dispersive Mixing in Heterogeneous Porous Media,* 2005, ISBN 3-933761-43-3

141 Schrenk, Volker: *Ökobilanzen zur Bewertung von Altlastensanierungsmaßnahmen,* 2005, ISBN 3-933761-44-1

142 Hundecha, Hirpa Yeshewatesfa: *Regionalization of Parameters of a Conceptual Rainfall-Runoff Model*, 2005, ISBN: 3-933761-45-X

143 Wege, Ralf: *Untersuchungs- und Überwachungsmethoden für die Beurteilung natürlicher Selbstreinigungsprozesse im Grundwasser,* 2005, ISBN 3-933761-46-8

144 Breiting, Thomas: *Techniken und Methoden der Hydroinformatik - Modellierung von komplexen Hydrosystemen im Untergrund*, 2006, 3-933761-47-6

145 Hrsg.: Braun, Jürgen; Koschitzky, Hans-Peter; Müller, Martin: *Ressource Untergrund: 10 Jahre VEGAS: Forschung und Technologieentwicklung zum Schutz von Grundwasser und Boden,* Tagungsband zur Veranstaltung am 28. und 29. September 2005 an der Universität Stuttgart, Campus Stuttgart-Vaihingen, 2005, ISBN 3-933761-48-4

146 Rojanschi, Vlad: *Abflusskonzentration in mesoskaligen Einzugsgebieten unter Berücksichtigung des Sickerraumes,* 2006, ISBN 3-933761-49-2

147 Winkler, Nina Simone: *Optimierung der Steuerung von Hochwasserrückhaltebecken-systemen,* 2006, ISBN 3-933761-50-6

148 Wolf, Jens: *Räumlich differenzierte Modellierung der Grundwasserströmung alluvialer Aquifere für mesoskalige Einzugsgebiete*, 2006, ISBN: 3-933761-51-4

149 Kohler, Beate: *Externe Effekte der Laufwasserkraftnutzung*, 2006, ISBN 3-933761-52-2

150 Hrsg.: Braun, Jürgen; Koschitzky, Hans-Peter; Stuhrmann, Matthias: *VEGAS-Statuskolloquium 2006,* Tagungsband zur Veranstaltung am 28. September 2006 an der Universität Stuttgart, Campus Stuttgart-Vaihingen, 2006, ISBN 3-933761-53-0

151 Niessner, Jennifer: *Multi-Scale Modeling of Multi-Phase - Multi-Component Processes in Heterogeneous Porous Media*, 2006, ISBN 3-933761-54-9

152 Fischer, Markus: *Beanspruchung eingeerdeter Rohrleitungen infolge Austrocknung bindiger Böden,* 2006, ISBN 3-933761-55-7

153 Schneck, Alexander: *Optimierung der Grundwasserbewirtschaftung unter Berücksichtigung der Belange der Wasserversorgung, der Landwirtschaft und des Naturschutzes*, 2006, ISBN 3-933761-56-5

154 Das, Tapash: *The Impact of Spatial Variability of Precipitation on the Predictive Uncertainty of Hydrological Models,* 2006, ISBN 3-933761-57-3

155 Bielinski, Andreas: *Numerical Simulation of CO_2 sequestration in geological formations*, 2007, ISBN 3-933761-58-1

156 Mödinger, Jens: *Entwicklung eines Bewertungs- und Entscheidungsunterstützungssystems für eine nachhaltige regionale Grundwasserbewirtschaftung*, 2006, ISBN 3-933761-60-3

157 Manthey, Sabine: *Two-phase flow processes with dynamic effects in porous media - parameter estimation and simulation,* 2007, ISBN 3-933761-61-1

158 Pozos Estrada, Oscar: *Investigation on the Effects of Entrained Air in Pipelines,* 2007, ISBN 3-933761-62-X

159 Ochs, Steffen Oliver: *Steam injection into saturated porous media – process analysis including experimental and numerical investigations*, 2007, ISBN 3-933761-63-8

160 Marx, Andreas: *Einsatz gekoppelter Modelle und Wetterradar zur Abschätzung von Niederschlagsintensitäten und zur Abflussvorhersage, 2007,* ISBN 3-933761-64-6

161 Hartmann, Gabriele Maria: *Investigation of Evapotranspiration Concepts in Hydrological Modelling for Climate Change Impact Assessment*, 2007, ISBN 3-933761-65-4

162 Kebede Gurmessa, Tesfaye: *Numerical Investigation on Flow and Transport Characteristics to Improve Long-Term Simulation of Reservoir Sedimentation*, 2007, ISBN 3-933761-66-2

163 Trifković, Aleksandar: *Multi-objective and Risk-based Modelling Methodology for Planning, Design and Operation of Water Supply Systems*, 2007, ISBN 3-933761-67-0

164 Götzinger, Jens: *Distributed Conceptual Hydrological Modelling - Simulation of Climate, Land Use Change Impact and Uncertainty Analysis*, 2007, ISBN 3-933761-68-9

165 Hrsg.: Braun, Jürgen; Koschitzky, Hans-Peter; Stuhrmann, Matthias: *VEGAS – Kolloquium 2007,* Tagungsband zur Veranstaltung am 26. September 2007 an der Universität Stuttgart, Campus Stuttgart-Vaihingen, 2007, ISBN 3-933761-69-7

166 Freeman, Beau: *Modernization Criteria Assessment for Water Resources Planning; Klamath Irrigation Project, U.S.*, 2008, ISBN 3-933761-70-0

167 Dreher, Thomas: *Selektive Sedimentation von Feinstschwebstoffen in Wechselwirkung mit wandnahen turbulenten Strömungsbedingungen*, 2008, ISBN 3-933761-71-9

168 Yang, Wei: *Discrete-Continuous Downscaling Model for Generating Daily Precipitation Time Series*, 2008, ISBN 3-933761-72-7

169 Kopecki, Ianina: *Calculational Approach to FST-Hemispheres for Multiparametrical Benthos Habitat Modelling,* 2008*,* ISBN 3-933761-73-5

170 Brommundt, Jürgen: *Stochastische Generierung räumlich zusammenhängender Niederschlagszeitreihen*, 2008, ISBN 3-933761-74-3

171 Papafotiou, *Alexandros: Numerical Investigations of the Role of Hysteresis in Heterogeneous Two-Phase Flow Systems*, 2008, ISBN 3-933761-75-1

172 He, Yi: *Application of a Non-Parametric Classification Scheme to Catchment Hydrology*, 2008, ISBN 978-3-933761-76-7

173 Wagner, Sven: *Water Balance in a Poorly Gauged Basin in West Africa Using Atmospheric Modelling and Remote Sensing Information*, 2008, ISBN 978-3-933761-77-4

174 Hrsg.: Braun, Jürgen; Koschitzky, Hans-Peter; Stuhrmann, Matthias; Schrenk, Volker: *VEGAS-Kolloquium 2008 Ressource Fläche III*, Tagungsband zur Veranstaltung am 01. Oktober 2008 an der Universität Stuttgart, Campus Stuttgart-Vaihingen, 2008, ISBN 978-3-933761-78-1

175 Patil, Sachin: *Regionalization of an Event Based Nash Cascade Model for Flood Predictions in Ungauged Basins*, 2008, ISBN 978-3-933761-79-8

176 Assteerawatt, Anongnart: *Flow and Transport Modelling of Fractured Aquifers based on a Geostatistical Approach,* 2008, ISBN 978-3-933761-80-4

177 Karnahl, Joachim Alexander: *2D numerische Modellierung von multifraktionalem Schwebstoff- und Schadstofftransport in Flüssen*, 2008, ISBN 978-3-933761-81-1

178 Hiester, Uwe: *Technologieentwicklung zur In-situ-Sanierung der ungesättigten Bodenzone mit festen Wärmequellen,* 2009, ISBN 978-3-933761-82-8

179 Laux, Patrick: *Statistical Modeling of Precipitation for Agricultural Planning in the Volta Basin of West Africa,* 2009, ISBN 978-3-933761-83-5

180 Ehsan, Saqib: *Evaluation of Life Safety Risks Related to Severe Flooding,* 2009, ISBN 978-3-933761-84-2

181 Prohaska, Sandra: *Development and Application of a 1D Multi-Strip Fine Sediment Transport Model for Regulated Rivers,* 2009, ISBN 978-3-933761-85-9

182 Kopp, Andreas: *Evaluation of CO_2 Injection Processes in Geological Formations for Site Screening,* 2009, ISBN 978-3-933761-86-6

183 Ebigbo, Anozie: *Modelling of biofilm growth and its influence on CO_2 and water (two-phase) flow in porous media,* 2009, ISBN 978-3-933761-87-3

184 Freiboth, Sandra: *A phenomenological model for the numerical simulation of multiphase multicomponent processes considering structural alterations of porous media*, 2009, ISBN 978-3-933761-88-0

185 Zöllner, Frank: *Implementierung und Anwendung netzfreier Methoden im Konstruktiven Wasserbau und in der Hydromechanik*, 2009, ISBN 978-3-933761-89-7

186 Vasin, Milos: *Influence of the soil structure and property contrast on flow and transport in the unsaturated zone*, 2010, ISBN 978-3-933761-90-3

187 Li, Jing: *Application of Copulas as a New Geostatistical Tool*, 2010, ISBN 978-3-933761-91-0

188 AghaKouchak, Amir: *Simulation of Remotely Sensed Rainfall Fields Using Copulas*, 2010, ISBN 978-3-933761-92-7

189 Thapa, Pawan Kumar: *Physically-based spatially distributed rainfall runoff modelling for soil erosion estimation*, 2010, ISBN 978-3-933761-93-4

190 Wurms, Sven: *Numerische Modellierung der Sedimentationsprozesse in Retentionsanlagen zur Steuerung von Stoffströmen bei extremen Hochwasserabflussereignissen*, 2011, ISBN 978-3-933761-94-1

191 Merkel, Uwe: *Unsicherheitsanalyse hydraulischer Einwirkungen auf Hochwasserschutzdeiche und Steigerung der Leistungsfähigkeit durch adaptive Strömungsmodellierung*, 2011, ISBN 978-3-933761-95-8

192 Fritz, Jochen: *A Decoupled Model for Compositional Non-Isothermal Multiphase Flow in Porous Media and Multiphysics Approaches for Two-Phase Flow*, 2010, ISBN 978-3-933761-96-5

193 Weber, Karolin (Hrsg.): *12. Treffen junger WissenschaftlerInnen an Wasserbauinstituten*, 2010, ISBN 978-3-933761-97-2

194 Bliefernicht, Jan-Geert: *Probability Forecasts of Daily Areal Precipitation for Small River Basins,* 2011, ISBN 978-3-933761-98-9

195 Hrsg.: Koschitzky, Hans-Peter; Braun, Jürgen: *VEGAS-Kolloquium 2010 In-situ-Sanierung - Stand und Entwicklung Nano und ISCO -,* Tagungsband zur Veranstaltung am 07. Oktober 2010 an der Universität Stuttgart, Campus Stuttgart-Vaihingen*,* 2010*,* ISBN 978-3-933761-99-6

196 Gafurov, Abror: *Water Balance Modeling Using Remote Sensing Information - Focus on Central Asia,* 2010, ISBN 978-3-942036-00-9

197 Mackenberg, Sylvia: *Die Quellstärke in der Sickerwasserprognose: Möglichkeiten und Grenzen von Labor- und Freilanduntersuchungen,* 2010, ISBN 978-3-942036-01-6

198 Singh, Shailesh Kumar: *Robust Parameter Estimation in Gauged and Ungauged Basins,* 2010, ISBN 978-3-942036-02-3

199 Doğan, Mehmet Onur: *Coupling of porous media flow with pipe flow,* 2011, ISBN 978-3-942036-03-0

200 Liu, Min: *Study of Topographic Effects on Hydrological Patterns and the Implication on Hydrological Modeling and Data Interpolation,* 2011, ISBN 978-3-942036-04-7

201 Geleta, Habtamu Itefa: *Watershed Sediment Yield Modeling for Data Scarce Areas,* 2011, ISBN 978-3-942036-05-4

202 Franke, Jörg: *Einfluss der Überwachung auf die Versagenswahrscheinlichkeit von Staustufen,* 2011, ISBN 978-3-942036-06-1

203 Bakimchandra, Oinam: *Integrated Fuzzy-GIS approach for assessing regional soil erosion risks,* 2011, ISBN 978-3-942036-07-8

204 Alam, Muhammad Mahboob: *Statistical Downscaling of Extremes of Precipitation in Mesoscale Catchments from Different RCMs and Their Effects on Local Hydrology,* 2011, ISBN 978-3-942036-08-5

205 Hrsg.: Koschitzky, Hans-Peter; Braun, Jürgen: *VEGAS-Kolloquium 2011 Flache Geothermie - Perspektiven und Risiken,* Tagungsband zur Veranstaltung am 06. Oktober 2011 an der Universität Stuttgart, Campus Stuttgart-Vaihingen, 2011, ISBN 978-3-933761-09-2

206 Haslauer, Claus: *Analysis of Real-World Spatial Dependence of Subsurface Hydraulic Properties Using Copulas with a Focus on Solute Transport Behaviour,* 2011, ISBN 978-3-942036-10-8

207 Dung, Nguyen Viet: *Multi-objective automatic calibration of hydrodynamic models – development of the concept and an application in the Mekong Delta,* 2011, ISBN 978-3-942036-11-5

208 Hung, Nguyen Nghia: *Sediment dynamics in the floodplain of the Mekong Delta, Vietnam,* 2011, ISBN 978-3-942036-12-2

209 Kuhlmann, Anna: *Influence of soil structure and root water uptake on flow in the unsaturated zone,* 2012, ISBN 978-3-942036-13-9

210 Tuhtan, Jeffrey Andrew: *Including the Second Law Inequality in Aquatic Ecodynamics: A Modeling Approach for Alpine Rivers Impacted by Hydropeaking,* 2012, ISBN 978-3-942036-14-6

211 Tolossa, Habtamu: *Sediment Transport Computation Using a Data-Driven Adaptive Neuro-Fuzzy Modelling Approach,* 2012, ISBN 978-3-942036-15-3

212 Tatomir, Alexandru-Bodgan: *From Discrete to Continuum Concepts of Flow in Fractured Porous Media,* 2012, ISBN 978-3-942036-16-0

213 Erbertseder, Karin: *A Multi-Scale Model for Describing Cancer-Therapeutic Transport in the Human Lung,* 2012, ISBN 978-3-942036-17-7

214 Noack, Markus: *Modelling Approach for Interstitial Sediment Dynamics and Reproduction of Gravel Spawning Fish,* 2012, ISBN 978-3-942036-18-4

215 De Boer, Cjestmir Volkert: *Transport of Nano Sized Zero Valent Iron Colloids during Injection into the Subsurface*, 2012, ISBN 978-3-942036-19-1

216 Pfaff, Thomas: *Processing and Analysis of Weather Radar Data for Use in Hydrology*, 2013, ISBN 978-3-942036-20-7

217 Lebrenz, Hans-Henning: *Addressing the Input Uncertainty for Hydrological Modeling by a New Geostatistical Method*, 2013, ISBN 978-3-942036-21-4

218 Darcis, Melanie Yvonne: *Coupling Models of Different Complexity for the Simulation of CO_2 Storage in Deep Saline Aquifers*, 2013, ISBN 978-3-942036-22-1

219 Beck, Ferdinand: *Generation of Spatially Correlated Synthetic Rainfall Time Series in High Temporal Resolution - A Data Driven Approach*, 2013, ISBN 978-3-942036-23-8

220 Guthke, Philipp: *Non-multi-Gaussian spatial structures: Process-driven natural genesis, manifestation, modeling approaches, and influences on dependent processes*, 2013, ISBN 978-3-942036-24-5

221 Walter, Lena: *Uncertainty studies and risk assessment for CO_2 storage in geological formations*, 2013, ISBN 978-3-942036-25-2

222 Wolff, Markus: *Multi-scale modeling of two-phase flow in porous media including capillary pressure effects,* 2013, ISBN 978-3-942036-26-9

223 Mosthaf, Klaus Roland: *Modeling and analysis of coupled porous-medium and free flow with application to evaporation processes,* 2014, ISBN 978-3-942036-27-6

224 Leube, Philipp Christoph: *Methods for Physically-Based Model Reduction in Time: Analysis, Comparison of Methods and Application,* 2013, ISBN 978-3-942036-28-3

225 Rodríguez Fernández, Jhan Ignacio*: High Order Interactions among environmental variables: Diagnostics and initial steps towards modeling,* 2013, ISBN 978-3-942036-29-0

226 Eder, Maria Magdalena: *Climate Sensitivity of a Large Lake,* 2013, ISBN 978-3-942036-30-6

227 Greiner, Philipp: *Alkoholinjektion zur In-situ-Sanierung von CKW Schadensherden in Grundwasserleitern: Charakterisierung der relevanten Prozesse auf unterschiedlichen Skalen,* 2014, ISBN 978-3-942036-31-3

228 Lauser, Andreas: *Theory and Numerical Applications of Compositional Multi-Phase Flow in Porous Media,* 2014, ISBN 978-3-942036-32-0

229 Enzenhöfer, Rainer: *Risk Quantification and Management in Water Production and Supply Systems,* 2014, ISBN 978-3-942036-33-7

230 Faigle, Benjamin: *Adaptive modelling of compositional multi-phase flow with capillary pressure,* 2014, ISBN 978-3-942036-34-4

Die Mitteilungshefte ab der Nr. 134 (Jg. 2005) stehen als pdf-Datei über die Homepage des Instituts: www.iws.uni-stuttgart.de zur Verfügung.